Very Large Array broad-band monitoring of the flux-ratio anomalous lens system B2045+265 as a probe for dark matter

By

Zane Deon LENTZ

UNIVERSITEIT VAN PRETORIA
UNIVERSITY OF PRETORIA
YUNIBESITHI YA PRETORIA
Denkleiers • Leading Minds • Dikgopolo tša Dihlalefi

Department of Physics
UNIVERSITY OF PRETORIA

Submitted in partial fulfilment of the requirements for the degree of MASTER OF SCIENCE (MSC) IN PHYSICS in the Faculty of Natural and Agricultural Sciences.

December 8, 2024

Supervisor: Prof. John MCKEAN

UNIVERSITY OF PRETORIA

Abstract

Faculty of Natural and Agricultural Sciences
Department of Physics

Master of Science (MSc) in Physics

Very Large Array broad-band monitoring of the flux-ratio anomalous lens system B2045+265 as a probe for dark matter

by Zane Deon LENTZ

Supervisor: Prof. John McKean

Keywords: Instrumentation: interferometers, Very Large Array – Methods: radio astronomy, strong gravitational lensing, dark matter – Analysis: observational

In this thesis, we investigate the flux-ratio anomaly of the cusp gravitational lens system CLASS B2045+265 with the aim of gaining insight into dark matter distributions within the galactic halo. CLASS B2045+265 has a radio-loud background galaxy that is being gravitationally lensed by a radio-loud foreground galaxy to form four lensed images. The flux-ratios of the four lensed images are known from previous observations to be inconsistent with the predictions from a simple singular isothermal ellipsoidal model for the foreground mass distribution. Here, we investigate the possible causes of the flux-ratio anomaly within CLASS B2045+265, which include a population of low mass dark matter haloes, as predicted by various dark matter models, variability from the background active galactic nucleus (AGN), or a propagation effect as the light passes through the foreground lensing galaxy. For this, we have used monitoring data taken with the Karl G. Jansky Very Large Array at frequencies between 12 and 18 GHz. Firstly, we introduce a pipeline for use with the Common Astronomy Software Applications (CASA) package, which allowed us to calibrate large quantities of radio interferometric data. We have also modified a python script to automate the process of self-calibration and model fitting using the Difference Mapping (DIFMAP) package. We use the aforementioned pipelines to perform a spectral analysis of CLASS B2045+265 over a 63-day monitoring period between 2022 March and May. The spectral indices of the three brightest lensed images A, B and C between 12 and 18 GHz are found to be $\alpha_A = 0.945 \pm 0.003$, $\alpha_B = 0.954 \pm 0.006$ and $\alpha_C = 0.962 \pm 0.005$, respectively, which are consistent at the 2σ-level. We find the flux densities of these components to be varying over time, but the change is not significant enough to contribute to the anomalous flux ratios. We find a 0.97% variation in the $R_{\rm cusp}$ parameter (0.5137 ± 0.0003) between day 0 and day 63 which quantifies the deviation from perfect symmetry in the ratios of a cusp lens system where a system with perfect symmetry has $R_{\rm cusp} = 0$. Based on our an analysis of the radio spectra, we do not observe any variations as a function of frequency, which allows us to rule out any frequency dependent effects, such as free-free absorption. Therefore, we believe the flux-ratio anomaly present in CLASS B2045+265 is most likely caused by a perturbation to the mass model by means of a combination between complex mass structures and sub-haloes present within the system. However, given the large mass-fraction in sub-haloes that we find is needed to explain the extreme $R_{\rm cusp}$ parameter for this system, it is most likely that these sub-haloes are along the line-of-sight towards the distant AGN, as opposed to being purely within the lensing galaxy. Further analysis with with high angular resolution telescopes or next gen (ngVLA, SKA, etc.) will be needed to determine whether this is the cause of the flux-ratio anomaly in CLASS B2045+265.

Declaration of Authorship

I, Zane Deon LENTZ, declare that the thesis, which I hereby submit for the degree of MSc in Physics at the University of Pretoria, is my own work and has not previously been submitted by me for a degree at this or any other tertiary institution.

Signature: 

Date: 09/12/2024

Acknowledgements

With special thanks to Prof. John McKean for help in conducting this research and as acting as the Principle Investigator of the Very Large Array data used herein. Further thanks to the Strong lensing at High Angular Resolution Programme (SHARP) team, and in particular, to those working within the Lensing over Frequency and Time (LoFT) team for their continued support and insight. This work is based on the research supported in part by the National Research Foundation of South Africa (Reference number: PMDS22063029447 and Project number: 128943). The National Radio Astronomy Observatory is a facility of the National Science Foundation operated under cooperative agreement by Associated Universities, Inc. We acknowledge the use of the ilifu cloud computing facility – www.ilifu.ac.za, a partnership between the University of Cape Town, the University of the Western Cape, Stellenbosch University, Sol Plaatje University and the Cape Peninsula University of Technology. The ilifu facility is supported by contributions from the Inter-University Institute for Data Intensive Astronomy (IDIA – a partnership between the University of Cape Town, the University of Pretoria and the University of the Western Cape), the Computational Biology division at UCT and the Data Intensive Research Initiative of South Africa (DIRISA).

Contents

Abstract iii

Declaration of Authorship iv

Acknowledgements v

1 Introduction 1

2 Radio Astronomy & Gravitational Lensing 5
2.1 Radio Astronomy . . . 5
2.2 Radio Telescopes . . . 6
2.3 VLA . . . 6
2.4 Interferometers . . . 8
2.5 Radio Continuum Emission . . . 10
2.6 Synchrotron Radiation . . . 12
2.7 Polarisation . . . 16
2.8 Gravitational Lensing . . . 19
2.8.1 Lens Equation . . . 20
2.8.2 Lens Potential . . . 21
2.9 Caustics and Critical Curves . . . 22
2.10 Mass Distribution . . . 23

3 Scientific Background 26
3.1 Anomalous Lenses . . . 26
3.2 The First Case: JVAS B1422+231 . . . 27
3.3 Our Target: CLASS B2045+265 . . . 30

4 Data 32
4.1 Observations . . . 32
4.2 Data Reduction: Stokes I . . . 32
4.3 Data Reduction: Stokes Q and U . . . 34
4.4 Self-Calibration . . . 40
4.5 Final Imaging in Stokes I, Q and U . . . 44

5 Results 45
5.1 The Stokes I, Q and U Imaging of CLASS B2045+265 . . . 45
5.2 The Radio Spectra of CLASS B2045+265 . . . 46
5.3 Flux Ratios . . . 56
5.4 R_{cusp} of B2045+265 . . . 58
5.5 Complex Mass Distributions and Dark Matter . . . 64

6 Discussion **69**
6.1 Absorption from Propagation Effects 69
6.2 Variability of The Lensed Images 70
6.2.1 Intrinsic Variability 70
6.2.2 Extrinsic Variability 71
6.3 The Gravitational Lens Mass Model 73

7 Conclusions **75**
7.1 Summary and Future Work 75

List of Abbreviations

AGN	**A**ctive **G**alactic **N**ucleus
CASA	**C**ommon **A**stronomy **S**oftware **A**pplications
CDM	**C**old **D**ark **M**atter
CLASS	**C**osmic **L**ens **A**ll-**S**ky **S**urvey
DM	**D**ark **M**atter
DIFMAP	**DIF**ference **MAP**ping
EVPA	**E**lectric **V**ector **P**osition **A**ngle
ISM	**I**nter**S**tellar **M**edium
JVAS	**J**odrell Bank-**V**LA **A**strometric **S**urvey
PDF	**P**robability **D**ensity **F**unction
RFI	**R**adio **F**requency **I**nterference
SIE	**S**ingular **I**sothermal **E**llipsoid
VLA	Karl G. Jansky **V**ery **L**arge **A**rray
VLBI	**V**ery **L**ong **B**aseline **I**nterferometery
WDM	**W**arm **D**ark **M**atter

Physical Constants

Speed of Light	$c = 2.99792458 \times 10^{8}\ \mathrm{m\,s^{-1}}$
Electron Mass	$m_e = 9.1093837015 \times 10^{-31}\ \mathrm{kg}$
Electron Charge	$e = 1.60217663 \times 10^{-19}\ \mathrm{C}$
Gravitational Constant	$G = 6.67430 \times 10^{-11}\ \mathrm{N\,m^2\,kg^{-2}}$
Flat Cosmology:	
Hubble Constant	$H_0 = 70\ \mathrm{km\,s^{-1}\ Mpc^{-1}}$
Matter density	$\Omega_M = 0.28$

Chapter 1

Introduction

Galaxies are thought to reside in near spherical structures, known commonly as haloes, which consist of both baryonic matter, in the form of dust, gas, and stars, and an unknown type of matter that is called *dark matter*. The existence of the latter has been hypothesised (mainly) due to the observed (luminous) mass of galaxies being unable to account for their inferred dynamical mass, which can be determined through, for example, the rotation curves of atomic hydrogen (H I). Also, massive galaxies are thought to form hierarchically through mergers, which is also dependent on the nature of dark matter. Therefore, understanding the properties of dark matter is fundamental for our understanding as to how our Universe formed and evolved.

Dark matter has been perplexing astronomers since its inception. There is clear evidence for its existence; gravitational effects have been observed and studied on numerous scales. However, the properties of dark matter and ultimately its composition are still widely debated. The astrophysical phenomena of gravitational lensing has proven to be an invaluable tool in the pursuit of constraining the properties of dark matter since it does not depend on the type of matter that is causing the light deflection. Gravitational lensing is a property of gravity whereby light propagating through space travels along a straight geodesic line. This geodesic can become curved under the influence of gravity, as described by Einstein's Theory of General Relativity (see Section 2.8). If the surface mass density of the intervening gravitational body is sufficiently high, then the light from the distant object is bent and distorted, and multiply-imaged by the foreground mass distribution. Through the study of the properties of these multiple images, it is possible to recover information on the mass distribution of the foreground gravitational body, which in our case will be a massive galaxy. Therefore, gravitational lensing is an invaluable tool in constraining the mass distributions of galaxies and investigating the level of dark matter that they contain.

In a recent review, Vegetti et al. (2023) discuss a wide-range of dark matter model theories (i.e. cold dark matter, warm dark matter, self-interacting dark matter and fuzzy dark matter) that can be investigated using gravitational lensing. This is because the various dark matter models alter the observed properties of the lensed images in different ways. It is theorized that dark matter sub-haloes either within the lens or along the line-of-sight to the distant lensed object may result in a local perturbation in the mass distribution that can be identified in the data. These "aberrations" in the lens can in principle be identified relative to what is predicted for a simple "perfectly smooth" lens (Mao and Schneider, 1998). For example, it is believed that in the context of a cold dark matter (CDM) Universe, dark matter is not evenly distributed within a galaxy-scale halo, but will contain many thousands of sub-haloes down to Jupiter-level masses that are able to interact gravitationally and grow in size through mergers. This leads to an uneven distribution of dark

matter "clumps" of various masses with a well-predicted mass function and mass fraction within galaxy-scale haloes, which at distances beyond our Local Group are best studied using gravitational lensing.

Those gravitational lens systems with observed image properties that strongly differ with those predicted from a smooth dark matter distribution are called "anomalous". The type of anomaly that is the focus of this thesis is one commonly referred to as a "flux-ratio anomaly", where the predicted flux-densities of the magnified images produced by the gravitational lens are at odds with those that we observe. However, these anomalous flux-ratios can be due to a myriad of reasons beyond dark matter. For example, a differential absorption or scattering of the light from each lensed image, an intrinsic variability of the emitted flux of the background source over time (combined with a gravitational time-delay) or an apparent extrinsic change over time due to low-mass objects passing along the line-of-sight to the lensed images (microlensing). Therefore, for any inference on dark matter to be made, these other factors must be ruled-out.

Hsueh et al. (2019) presented a detailed analysis of seven gravitational lens systems to understand the level of dark matter that is needed to explain the observed flux-ratios. Using Bayesian inference methods in conjunction with Markov Chain Monte Carlo (MCMC) modelling, Hsueh et al. (2019) were able to constrain the abundance of dark matter sub-haloes, providing a stringent test of both cold and warm dark matter models. In Figure 1.1, we see the probability distribution functions that those authors obtained for the mass-fraction in dark matter clumps. They found a higher mass fraction in sub-haloes for this sample than had previously been found by Xu et al. (2015) (black vertical line). However, Hsueh et al. (2019) comment that the inclusion of line-of-sight haloes would decrease the predicted abundance of sub-haloes within the main lensing halo, and thus, could be comparable with the numbers predicted by numerical simulations. These galaxies, having a predicted fractional mass in sub-haloes that is comparable with that from CDM numerical simulations is critical to the research done in this project, as this high fractional mass in sub-haloes may be able to account for the flux-ratio anomalies.

The system we focus on throughout this thesis is CLASS B2045+265, which has the most anomalous flux-ratios of any known gravitational lens. The discovery of CLASS B2045+265 was presented by Fassnacht et al. (1999), where the system was introduced as having four lensed images, whereby a flat-spectrum radio source was gravitationally lensed by another flat-spectrum radio source (see Figure 1.2). It was found that simple lens models could reproduce the image positions of CLASS B2045+265, but not the image fluxes. A further study of CLASS B2045+265 was done by McKean et al. (2007); high angular resolution radio along with optical and infrared imaging were used to argue against propagation and scintillating affects, that is, interstellar scattering (see Figure 1.3). This leaves open the question as to whether the observed anomaly is due purely from dark matter sub-haloes or luminous CDM substructure from a potential dwarf galaxy within the Einstein radius. Understanding the source of the flux-ratio anomaly in CLASS B2045+265 forms the basis of this project, whereby we use the Karl G. Jansky Very Large Array (VLA) to conduct a high angular resolution broad-band spectral and temporal analysis. Using these data, we are able to investigate whether propagation effects or source variability play a roll in the observed anomaly, and whether these factors have a strong enough affect to explain the observed anomaly. If not, then further explanations, such as a complex mass model with dark matter sub-haloes would be more likely. Further study into the mass distribution would also allow us to gain a deeper understanding of the structure of the foreground galaxy of CLASS B2045+265.

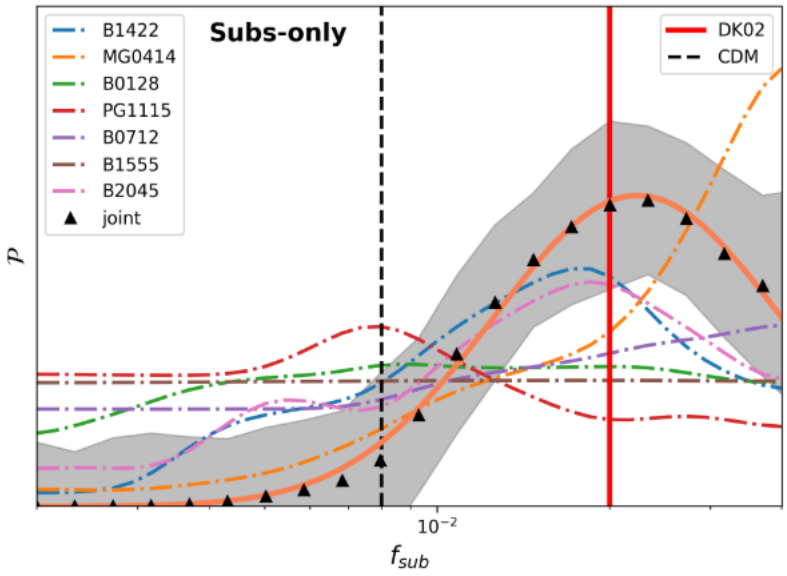

FIGURE 1.1: The probability density distribution of the fractional mass in sub-haloes (f_{sub}) using seven gravitational lens systems with four lensed images, as well as the joint constraints (triangles and thick curve). The black vertical line shows the upper limit expected from CDM models (Xu et al., 2015). Image taken from Hsueh et al. (2019).

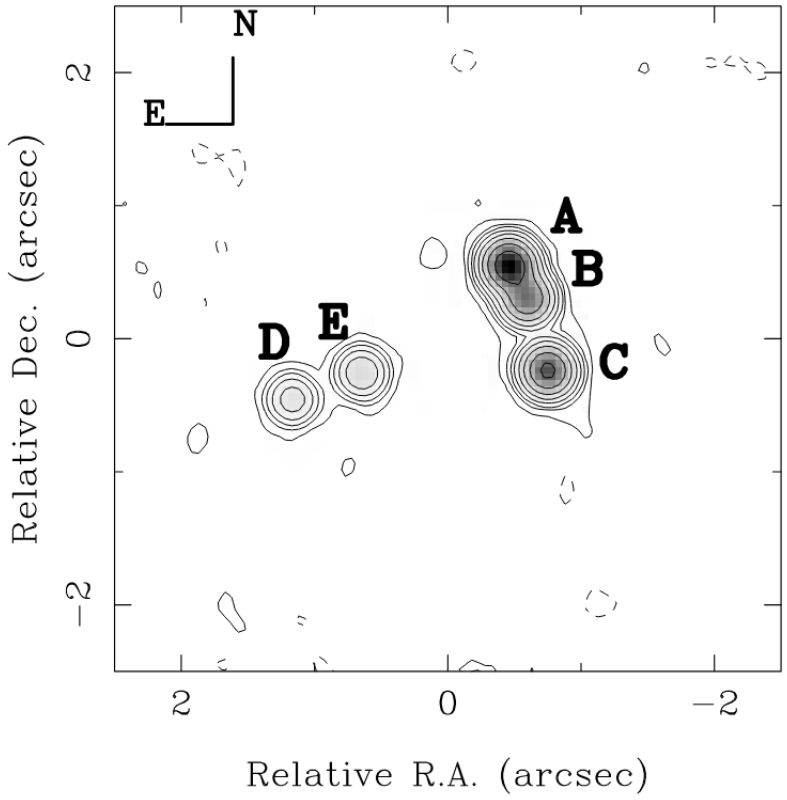

FIGURE 1.2: Very Large Array (VLA) imaging of CLASS B2045+265, showing four lensed images (A, B, C and D), and a fifth component that is associated with the lensing galaxy (E). Image taken from Fassnacht et al. (1999).

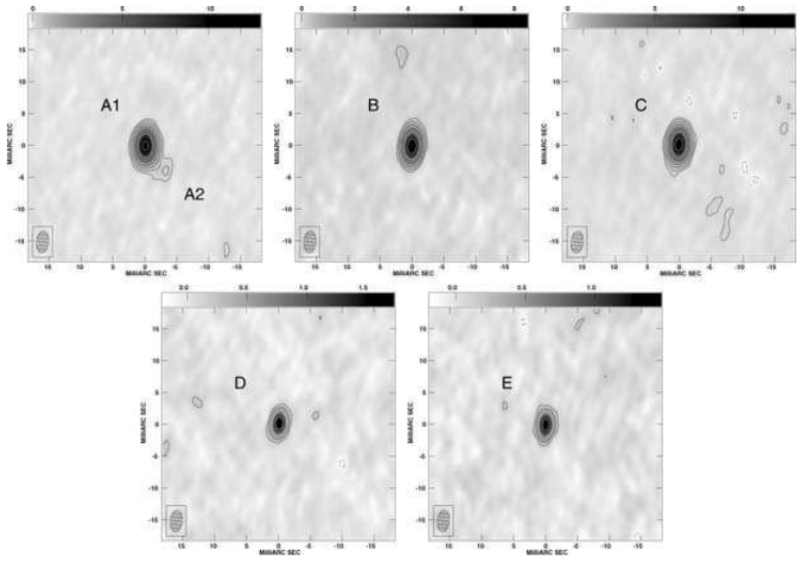

FIGURE 1.3: Very Long Baseline Array (VLBA) high angular resolution imaging of the individual components of CLASS B2045+265 at 5 GHz. The lensed images (A, B, C and D) and the lensing galaxy (E) are detected. Image taken from McKean et al. (2007).

This Masters in Science (MSc) project will aim to account for the observed flux-ratio anomaly by answering the following questions:

- What can we learn about flux-ratio anomalies from data of similar quality to that obtained with the SKA-MID in Band 5?
- Can a propagation effect or source variability explain the flux-ratio anomaly in CLASS B2045+265?
- Is the mass fraction in sub-haloes needed to explain the flux-ratio anomaly in CLASS B2045+265 consistent with theoretical expectations?

This MSc thesis is arranged as follows. In Chapter 2, we discuss the history of radio astronomy and give a detailed introduction to the VLA and the scientific theory behind radio continuum emission sources. Here, we also present the relevant theory on gravitational lensing as pertaining to our target. Later, in Chapter 3, we discuss the nature of the flux-ratio anomaly in CLASS B2045+265. These introductory chapters will give the context as we progress through our data analysis. In Chapter 4, we outline the procedures developed and applied to obtain, reduce and analyse the data collected for this project. In Chapter 5, the results from this data analysis are presented in the context of our scientific goals. Finally, in Chapters 6 and 7, we conduct a more in-depth discussion on our results and summarize our conclusions, respectively, in terms of testing dark matter models with broad band spectral imaging of radio-bright gravitationally lensed radio sources.

Chapter 2

Radio Astronomy & Gravitational Lensing

In this chapter, we introduce the field of radio astronomy including its historical background. This also includes a review of the scientific background of the instrumentation and science concepts needed to understand the research described in this thesis. The main concepts that we will introduce are radio interferometry (Section 2.4), synchrotron radiation from celestial radio sources (Section 2.6) and gravitational lensing (Section 2.8), which forms the basis for the research conducted on our target CLASS B2045+265.

2.1 Radio Astronomy

The field of radio astronomy essentially dates back to 1932, which is fairly late in comparison to optical astronomy. This was due to two main reasons; first, it was expected that the thermal emission from radio sources (stars) would be too faint to be seen, and second, because the technology needed to make observations at radio wavelengths had still to be developed. This changed when Karl G. Jansky, a radio engineer at Bell Laboratories in the United States, noticed a noisy radio signal at 20.5 MHz. This noise was noted to vary across the sky every 23 hours and 56 minutes (a sidereal day), which led Jansky to conclude that the signal was extraterrestrial in origin. In 1933 Jansky published his paper titled *"Radio Waves from Outside the Solar System"*, which outlined what we now know, that he had in fact detected emission from the Galactic Centre of our own Milky Way. Jansky's discovery caught the attention of Grote Reber, who in his own backyard, built a 10 m radio telescope that would go on to create the first radio map of the sky and would ultimately show that the emission was non-thermal in origin.

Radio astronomy has since grown considerably and is now a widely researched field of astronomy. Using both single dish telescopes and multi-dish interferometry, which is discussed later in this chapter, radio astronomy allows us to observe what would otherwise be hidden aspects of our Universe in unprecedented sensitivity and angular resolution. Celestial objects that are typically observed at radio frequencies (between 10 MHz and 1 THz) for ground based telescopes are thermal and non-thermal continuum sources, and also spectral line sources, such as masers or atomic hydrogen and molecular transitions. This observing window for radio sources is set from the reflection of low frequency radio waves by our ionosphere and from absorption and emission effects at high frequencies from molecules in our atmosphere.

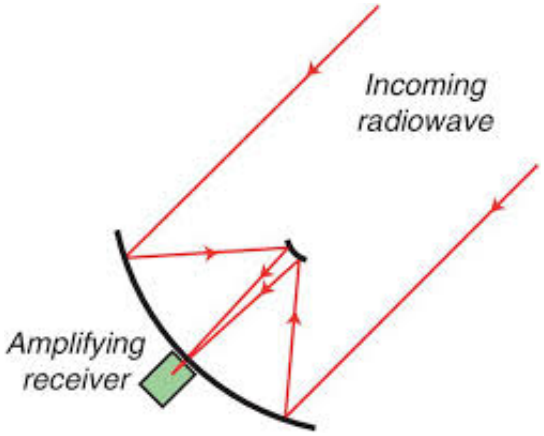

FIGURE 2.1: Diagram of parabolic dish antenna radio telescope receiving an incoming radio signal. Image taken from Christian and Roy (2017).

2.2 Radio Telescopes

Radio telescopes come in a myriad of shapes and sizes, all with the intention of turning weak radio waves into voltages induced in a conductor that we can measure; it is these voltages that encode the information about the celestial radio sources. These telescopes typically consist of an antenna that gathers the incoming radio waves. Throughout this thesis, the VLA is used for our observations, which consists of 27 dish-shaped telescopes that are 25 m in diameter. The angular resolution of a filled aperture is given by,

$$\theta = k \times \frac{\lambda}{D}, \tag{2.1}$$

where θ is the angular resolution of the single dish telescope (in radians), λ is the observing wavelength and D is the diameter of the dish. Note that the constant of proportionality, k, is related to the illumination pattern of the aperture. A single dish radio telescope is limited in its angular resolution because even though the diameter can be very large, for example, around 15 to 500 m, the wavelengths of the light are also very long (few metres to mm). Therefore, the angular resolution of a radio telescope at GHz frequencies is typically a few to a few tens of arcmin. For example the angular resolution of the HartRAO telescope (26 m) at 15 GHz is approximately 9.4 arcminutes.

As seen in Figure 2.1, the parabolic dish reflects radio waves in phase to a focal point where they arrive at the same time, after which the signal is sent to a receiver that amplifies, filters and converts the input voltage to a measurable signal. This process is discussed in more detail in the next section where we focus on the design of the VLA.

2.3 VLA

The VLA has been in operation since 1980, but was upgraded in the early 2000s to improve its overall sensitivity. The array consists of 27 parabolic dish-shaped telescopes (with one extra that is typically undergoing maintenance). The 27 telescopes all work in conjunction with each other to form an interferometer, discussed in more detail in Section 2.4, which provides a larger effective collecting area with respect to a single-dish. The maximum distance between the antennas is 36 km, which results

FIGURE 2.2: The VLA located on the Plains of San Agustin in New Mexico. Credit: NRAO/AUI/NSF.

in improving the angular resolution of the data, such that,

$$\theta = \frac{\lambda}{B}, \tag{2.2}$$

where θ is the angular resolution of the interferometer (in radians), λ is the observing wavelength and B is the distance between two dishes, which is called the baseline length. Given that the dishes of an interferometer can be placed far apart, this technique allows astronomers to produce high angular resolution images of celestial objects. In this thesis, the data is collected with the VLA in its largest configuration, which provides an angular resolution of around 0.15 arcsec.

The VLA is situated on the Plains of San Agustin in New Mexico (see Figure 2.2). Away from major cities, ringed by mountains and coupled with a desert climate, the location of the VLA is ideal for radio astronomy with minimal radio frequency interference and low humidity that would affect the incoming signals at both low and high frequencies.

As seen in Figure 2.3, the telescopes of the VLA are arranged in the characteristic Y-shape, where each of the individual telescopes are placed on a regular grid with respect to each other. This means that the "aperture" of the interferometer is not completely filled, but instead has gaps in it. This has implications for the resulting imaging that is produced with the VLA. In Figure 2.3, we also show the relative positions of the VLA antennas for our experiment, which is called A-configuration. The output data from the VLA is a cross-correlation of signals from each pair of antennas. Each antenna has eight receivers that collects these signals at different continuous frequency ranges between 1 and 50 GHz, as seen in Table 2.1. For the observations carried out in this thesis, we use the Ku-band receiver, which operates at a frequencies between 12 and 18 GHz.

Electromagnetic waves collected by telescopes like the VLA can occasionally share the same electric vector position angle (EVPA), in which case the signal is described as polarised. The VLA is able to detect this polarisation by having orthogonal dipole receivers that each detect incoming signals as a voltage at different

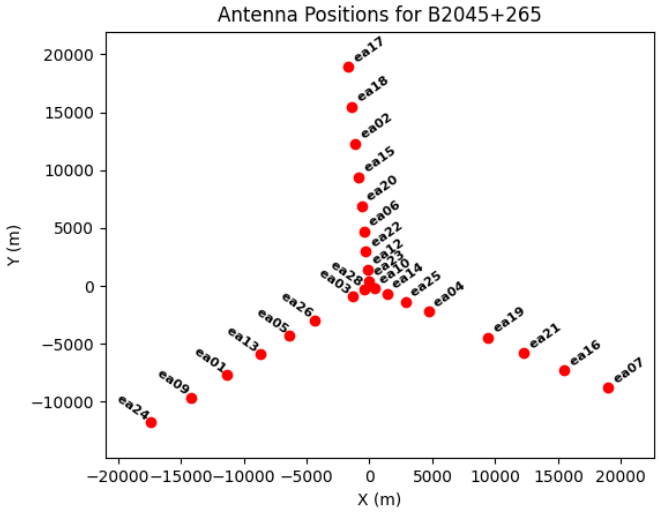

FIGURE 2.3: Layout of 27 VLA dish-telescopes, when in A-configuration. Created using the data collected for this thesis.

TABLE 2.1: The receivers that provide a continuous frequency coverage between 1 and 50 GHz for the VLA. Note that there are also lower frequency receivers that are sensitive below 1 GHz, but these do not provide a continuous frequency coverage.

L-band	1–2 GHz
S-band	2–4 GHz
C-band	4–8 GHz
X-band	8–12 GHz
Ku-band	12–18 GHz
K-band	18–26.5 GHz
Ka-band	26.5–40 GHz
Q-band	40–50 GHz

orientations. In the case of the VLA, the receivers measure the R- and L-handed circular polarisation. The polarisation properties of radio sources is discussed in more detail below.

2.4 Interferometers

As mentioned in Section 2.3, the use of interferometers in astronomy allows us to observe the Cosmos at higher angular resolution than is typically possible with single-dish telescopes (see Equation 2.1). Interferometry works on the basis of constructive and destructive interference patterns that are created when the incoming electromagnetic waves are combined from each dish. This can be best understood by considering a simple two-element interferometer that is observing a distant source. As seen in Figure 2.4, the electromagnetic wave arriving at Dish 1 has a longer distance to travel than that arriving at Dish 2, such that,

$$\vec{b} \cdot \hat{s} = b \cos\theta, \tag{2.3}$$

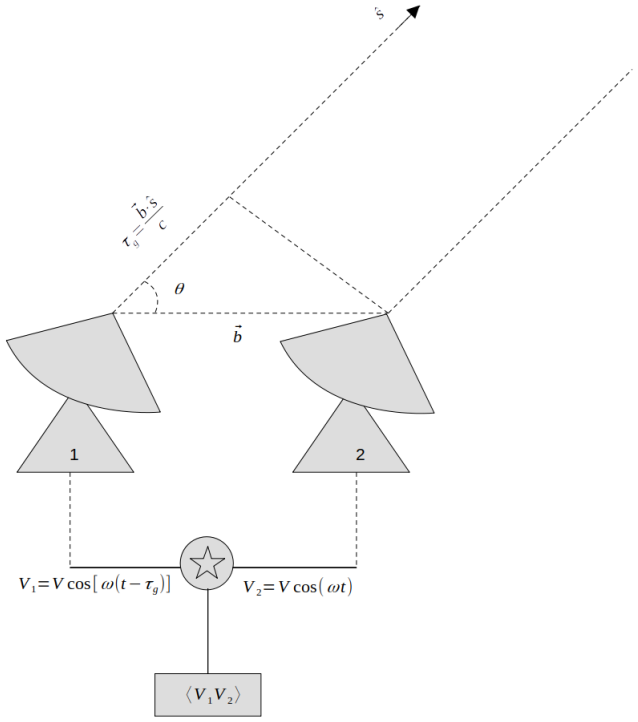

FIGURE 2.4: Example schematic of a two element interferometer separated by a baseline $\vec{b}$, combining an incoming signal with a time delay τ_g.

where $\vec{b}$ is the projected baseline length and $\hat{s}$ is the unit vector towards the source. As electromagnetic waves travel at the speed of light c, this distance corresponds to a geometric time delay,

$$\tau_g = \frac{\vec{b}\cdot\hat{s}}{c}. \tag{2.4}$$

Therefore, the output voltages received from the electromagnetic waves are,

$$V_1 = V\cos[\omega(t-\tau_g)] \qquad V_2 = V\cos(\omega t) \tag{2.5}$$

for Dish 1 and Dish 2, respectively. Here, ω corresponds to the angular frequency, $\omega = 2\pi c/\lambda$. These voltages are then multiplied and time averaged using a piece of equipment that is called a correlator. The resulting output from this process is,

$$R = \langle V_1 V_2 \rangle = \frac{V^2}{2}\cos(\omega\tau_g). \tag{2.6}$$

The sinusoidal fringe pattern created by this process has a period that is directly proportional to the baseline length b, via the geometric delay τ_g, and the observing frequency ν, via ω. From this we again find, as stated in Equation 2.2, that longer baselines and higher observing frequencies produce more rapidly varying fringes across the sky and thus provide information on smaller angular-scales.

Thus far, we have only considered the case for a distant point source. For an extended surface brightness distribution, we can consider the source as the sum of independent point sources with sky brightness $I_\nu(\hat{s})$. The interferometer would thus

have the response of a real component,

$$R_c = \int I_v(\hat{s}) \cos(2\pi \vec{b} \cdot \hat{s}/\lambda) d\Omega, \tag{2.7}$$

and an imaginary component with a 90° phase delay,

$$R_s = \int I_v(\hat{s}) \sin(2\pi \vec{b} \cdot \hat{s}/\lambda) d\Omega. \tag{2.8}$$

By expressing these in complex notation, we obtain the definition of the complex visibility,

$$V = Ae^{-i\phi}, \tag{2.9}$$

where A is the amplitude expressing how bright the source is and ϕ is the phase, which provides information to its position. Both the amplitude and phase encode information about the surface brightness distribution of the radio source. By combining Equations 2.7, 2.8 and 2.9, we are able to obtain the response of a two element interferometer to an extended source as,

$$V = \int I_v(\hat{s}) \exp(-i2\pi \vec{b} \cdot \hat{s}/\lambda) d\Omega. \tag{2.10}$$

Equation 2.10 can be mapped to a coordinate system which would then allow us to obtain the response of our interferometer from anywhere in the sky. This response is the inverse Fourier transform of the sky brightness distribution, and thus, we are able to easily go from the visibility Fourier plane to the sky plane.

As previously mentioned, we are looking at a case that consists of two dishes and thus one baseline and one visibility. In the case of the VLA, we have 27 dishes corresponding to 351 baselines. Each of these baselines corresponds to a visibility orientated in the direction of the baseline on the UV plane. The UV plane represents the Fourier space sampled by an interferometer, where each baseline corresponds to a specific point in this plane. Together, these visibility's inform us on the power corresponding to some angular-size on the sky. The Fourier transform of these visibilities then in turn gives us a sampled image of the sky (the sky plane), based on the power and angular size observed. Incomplete UV coverage results in distortions in the sky plane image. These distortions are counteracted by sampling techniques to improve the UV coverage as well as implementation of cleaning algorithms (discussed in later chapters) to better represent the sky plane. of However, where are these signals coming from? In the next section we will discuss radio continuum emission with a focus on synchrotron emission.

2.5 Radio Continuum Emission

Thermal and non-thermal electromagnetic radiation is emitted with a power that is described by Larmor's formula,

$$P = \frac{2}{3} \frac{q^2 a^2}{c^3}, \tag{2.11}$$

where P is the power produced when a particle of charge q is (tangentially) accelerated by a. In the case of thermal emission, an ensemble of accelerated particles

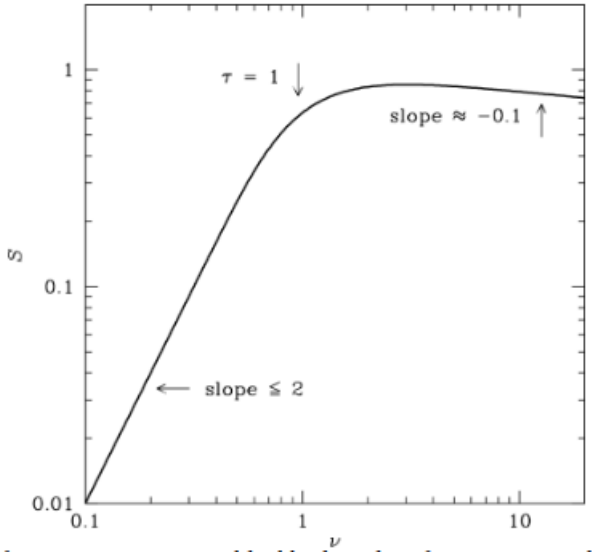

FIGURE 2.5: Radio spectrum of an HII region, taken from Condon and Ransom (2016). At low frequencies the spectrum has a spectral index of $\alpha \leq 2$ (due to the Rayleigh-Jeans part of spectrum) until at some frequency (ν) the optical depth becomes < 1 and the slope changes to ≈ -0.1.

with a temperature $T > 0$ K produces radiation that is dependent on their thermal energy and velocity. Whereas in non-thermal emission, the particle acceleration is independent of temperature and is typically dependent on the presence and strength of magnetic fields (e.g. synchrotron radiation) or gravitational interactions (e.g.Bremsstrahlung radiation).

Examples of thermal emission include black body radiation from stars, grey body radiation from heated dust and free-free emission, which is often observed in regions of ionised plasma (e.g., HII regions). For black body radiation to peak at radio wavelengths, then the source must be extremely cold. For example, cold dust ($T_D \sim 30$ K) typically radiates in the far-infrared regime, and it is the Rayleigh-Jeans part of the spectrum that is observed at radio wavelengths. However, this emission would be very faint, hence at the radio regime we shouldn't expect blackbody emission from anything that isn't nearby. In HII regions, free electrons interact electrostatically with ions in the plasma. The free electrons do not get captured by the ion and thus the electron is free before and after the interaction, hence the term "free-free". When these electrons interact with the ion, they are accelerated via the Coulomb force (F),

$$|a| = \frac{F}{m_e} = \frac{Ze^2}{m_e r^2}, \tag{2.12}$$

where m_e is the electron mass, Z is the number of electrons removed from the ion, e is the charge of the electron, and r is the distance between the electron and the ion. The strength of the emission is related to a number of properties of the interaction, most notably the velocity distribution of the electrons, which is described by a non-relativistic Maxwellian distribution; this is dependent on the temperature of the electrons, and hence, determines that this is a thermal process. In Figure 2.5, we see the spectrum of free-free emission for a typical HII region.

For non-thermal radiation, as mentioned previously, charged particles are accelerated by a magnetic field or gravitational interactions (we will focus on particles

accelerated by magnetic fields), but the type of radiation is defined by the velocity of the particle, that is,

- gyro radiation, when the particle velocity is much less than the speed of light ($v \ll c$);
- cyclotron radiation, when the particle velocity is less than the speed of light ($v < c$); and
- synchrotron radiation, when the particle velocity is close to the speed of light ($v \sim c$).

The magnetic force is given by,

$$\vec{F} = \frac{q(\vec{v} \times \vec{B})}{c}, \tag{2.13}$$

where a particle of charge q is travelling with velocity $\vec{v}$ ($v \ll c$) through a magnetic field $\vec{B}$. This force $\vec{F}$ is perpendicular to $\vec{v}$ such that,

$$\vec{F} \cdot \vec{v} = 0, \tag{2.14}$$

thus no work is done on the particle. In this set up, the velocity parallel ($v_{\parallel}$) to the magnetic field is constant and so is dependent on the total magnitude of the velocity $|v|$. Therefore, the magnitude of the perpendicular velocity component ($v_{\perp}$) is constant, but with changing direction. The combination of these velocities results in the charged particle travelling along uniform magnetic field lines in a helical path with radius r perpendicular to the field lines and with angular frequency $\omega = \frac{v}{r}$ (see Figure 2.6). The angular velocity required to balance the centripetal force,

$$|F_c| = m\omega^2 r, \tag{2.15}$$

and the magnetic force (F_m) from Equation 2.13 is independent of velocity, so long as $v \ll c$. Thus, the gyro frequency (ω_G) we obtain from equating Equations 2.15 and 2.13 is,

$$\omega_G = \frac{qB}{mc}. \tag{2.16}$$

For an electron, this gyro frequency equates to a frequency

$$\left(\frac{\nu_G}{\text{MHz}}\right) = 2.8 \left(\frac{B}{\text{gauss}}\right), \tag{2.17}$$

which requires extremely high magnetic fields, such as found for neutron stars, in order to have a frequency high enough to propagate through the interstellar medium (ISM) (Condon and Ransom, 2016). Thus, the more prominent case of non-thermal radiation is that of synchrotron radiation, which will be discussed in detail in the next section.

2.6 Synchrotron Radiation

As mentioned in the previous section, synchrotron radiation comes from charged particles travelling at relativistic speeds ($v \sim c$) through a magnetic field. Due to relativistic effects, the processes in which the particle moves is dictated by special relativity as it undergoes a Lorentz transformation from the inertial coordinate frame

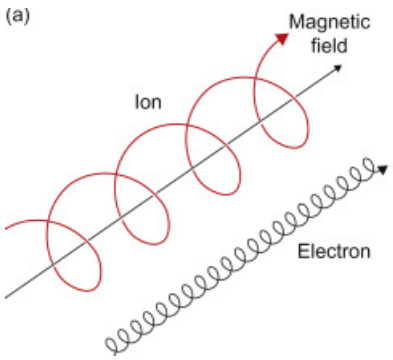

FIGURE 2.6: Image of the helical path taken by a charged particle moving through a uniform magnetic field with example radii of an ion compared to that of an electron (taken from McCracken and Stott, 2013).

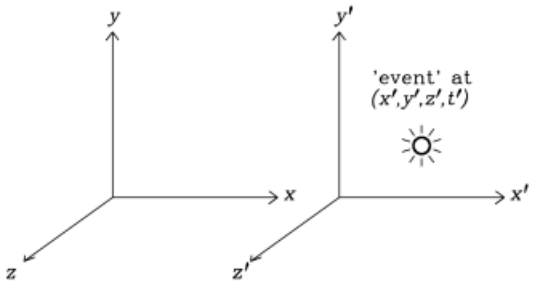

FIGURE 2.7: The coordinate system of two reference frames in which an event happens. The un-primed inertial coordinate frame and the primed frame moving with a velocity in the x-direction (taken from Condon and Ransom, 2016).

to a frame moving at an initial velocity (see Figure 2.7). These frames are related to each other such that an event can be transformed from one frame to anther via the following,

$$x = \gamma(x' + vt'), \quad y = y', \quad z = z', \quad t = \gamma(t' + \beta x'/c), \tag{2.18}$$

$$x' = \gamma(x - vt), \quad y' = y, \quad z' = z, \quad t' = \gamma(t - \beta x/c), \tag{2.19}$$

where

$$\beta \equiv v/c, \tag{2.20}$$

and

$$\gamma \equiv (1 - \beta^2)^{1/2}. \tag{2.21}$$

Due to the relativistic nature of the particle and the conservation of momentum, the relativistic mass m is different to that of its rest mass m_0, such that,

$$m = \gamma m_0. \tag{2.22}$$

Thus we get the angular frequency,

$$\omega_B = \frac{qB}{(\gamma m_0)c}, \tag{2.23}$$

which for a relativistic particle travelling along its helical path is smaller than that

of a non-relativistic particle. This means that we would need an even stronger magnetic field than that needed to observe a non-relativistic particle. However, there are more relativistic properties at play.

From Larmor's equation (Equation 2.11), we find the power in the primed coordinate system to be,

$$P' = \frac{2q^2 a_\perp^2}{3c^3}, \tag{2.24}$$

where $a'_\perp$ is the perpendicular acceleration of the particle in the primed coordinate frame (see Figure 2.7). To convert this into the inertial frame we apply the chain rule derivative, such that for

$$a_\perp = (a_y^2 + a_z^2)^{1/2} \tag{2.25}$$

we get,

$$a_y \equiv \frac{dv_y}{dt} = \frac{dv_y}{dt'}\frac{dt'}{dt} = \frac{1}{\gamma}\frac{dv'_y}{dt'}\frac{dt'}{dt} = \frac{a'_y}{\gamma^2}. \tag{2.26}$$

Similarly,

$$a_z \equiv \frac{dv_z}{dt} = \frac{a'_z}{\gamma^2}, \tag{2.27}$$

so,

$$a_\perp = \frac{a'_\perp}{\gamma^2}. \tag{2.28}$$

By substituting Equation 2.28 into Equation 2.24, we get the prime power of Larmor's formula in terms of the inertial acceleration,

$$P' = \frac{2q^2 a_\perp^2 \gamma^4}{3c^3}. \tag{2.29}$$

This formula is the same in both the prime and the inertial reference frame, such that $P' = P$, with power being relativistically invariant. To compare this with the non-relativistic case we use the fact that

$$a_\perp \equiv \frac{dv_\perp}{dt} = \omega_B v_\perp = \omega_B v \sin\alpha, \tag{2.30}$$

where α is the pitch angle between the electron velocity and the magnetic field, which along with Equation 2.23, we get,

$$P = \frac{2q^2}{3c^3}\gamma^2 \frac{q^2 B^2}{m_0^2 c^2} v^2 \sin^2\alpha. \tag{2.31}$$

This power equation for an electron is however often written in terms of the Thomson cross section of an electron σ_T,

$$\sigma_T = \frac{8\pi}{3}\left(\frac{e^2}{m_0 c^2}\right)^2, \tag{2.32}$$

and the magnetic energy density U_B,

$$U_B = \frac{B^2}{8\pi}, \tag{2.33}$$

FIGURE 2.8: In the frame of the electron, the dipole radiation power pattern is shown by the dotted line. However, in the frame of the observer, the transformed pattern is shown by the solid line with a width $\theta = 2/\gamma$ for $\gamma \gg 1$. Taken from Condon and Ransom (2016).

then the instantaneous power emitted for a single electron becomes

$$P = 2\sigma_T \beta^2 \gamma^2 c U_B \sin^2 \alpha. \tag{2.34}$$

The time-averaged synchrotron power over an electron's lifetime is found by averaging over all pitch angles, which gives,

$$P = \frac{4}{3}\sigma_T \beta^2 \gamma^2 c U_B. \tag{2.35}$$

For relativistic electrons ($\gamma \gg 1$) the power emitted is a factor of γ^2 greater than that of a non-relativistic electron.

Due to the relativistic nature of the electron, not only is the power greater, but the power pattern of the radiation is also affected as, in the observers frame, the electron "catches up" with its own emission in a phenomenon known as relativistic beaming, as seen in Figure 2.8.

In relativistic beaming, the radiation pattern seen by the observer is a narrow beam of width $\theta = 2/\gamma$ for $\gamma \gg 1$. This radiation is only seen in pulses due to the helical path of the electron as it moves through the magnetic field. As can be seen from Figure 2.6, this means the emission will only be measured by an observer once a cycle, that is, during the brief period when the electron's power pattern is directed towards the observer. By considering Figure 2.9, we are able to determine how long this pulse lasts by finding the difference in time between the end of the pulse and the start of the pulse, that is,

$$\Delta t_p = \frac{\Delta x}{v} + \frac{(x - \Delta x)}{c} - \frac{x}{c} = \frac{\Delta x}{v} - \frac{\Delta x}{c} = \frac{\Delta x}{v}\left(1 - \frac{v}{c}\right), \tag{2.36}$$

where,

$$\left(1 - \frac{v}{c}\right) = \left(1 - \frac{v}{c}\right)\frac{1 + v/c}{1 + v/c} = \frac{1 - v^2/c^2}{1 + v/c} \approx \frac{1}{2\gamma^2}, \tag{2.37}$$

such that,

$$\Delta t_p = \frac{\Delta x}{v}\frac{1}{2\gamma^2} = \frac{\Delta \theta}{\omega_B}\frac{1}{2\gamma^2} = \frac{1}{\gamma^3 \omega_B} = \frac{1}{\gamma^2 \omega_G}. \tag{2.38}$$

This results in very narrow pulses of power over time, which can be converted via a Fourier transform into the synchrotron power spectrum. This spectrum is continuous, but most of the power is emitted at a characteristic frequency, which is dependent on the energy of the electron and the magnetic field strength, such that,

$$\nu_c \approx \gamma^2 \nu_G \tag{2.39}$$

where,

$$E = \gamma m_e c^2. \tag{2.40}$$

By differentiating Equation 2.40 in terms of Equation 2.39 we get,

$$\frac{dE}{d\nu} \approx \frac{1}{2(\nu\nu_G)^{1/2}} m_e c^2. \tag{2.41}$$

With the emission co-efficient (ϵ_ν) for synchrotron radiation being,

$$\epsilon_\nu = -\frac{dE}{dt} N(E) \frac{dE}{d\nu}, \tag{2.42}$$

using Equations 2.35, 2.39 and 2.40. We find for a collection of electrons, whose energy distribution is described by the power-law,

$$N(E) = kE^\delta, \tag{2.43}$$

where $N(E)$ is the number of electrons per unit volume, k is a normalisation constant and δ is the power-law index,

$$\epsilon_\nu \propto I_\nu \propto S_\nu \propto \nu^\alpha, \tag{2.44}$$

where α is now the spectral index,

$$\alpha = \frac{\delta - 1}{2}, \tag{2.45}$$

I_ν is the specific intensity and S_ν is the flux-density. Specifically, we show how the flux density of a synchrotron emitting radio source varies as a function of frequency in Figure 2.10. When the optical depth is $\tau \approx 1$ at some frequency ν_1, the brightness temperature of the radiation that is emitted has the same temperature of the electrons within the plasma. At frequencies below ν_1, synchrotron self-absorption occurs and there is a turnover in the low-frequency spectrum of the source. At frequencies above ν_1, the radio source becomes optically thin to the synchrotron emission and the resulting spectrum is given by the power-law given in Equation 2.44. For a radio source with a spectral index of α, the synchrotron self-absorption can be described by the model,

$$S_\nu = S_{\nu_1} (\nu/\nu_1)^{2.5} (1 - \exp[-\tau(\nu/\nu_1)^{\alpha - 2.5}]). \tag{2.46}$$

In this thesis, we study a lensed radio source with a flat-radio spectrum, defined as having $\alpha > -0.5$ at GHz frequencies. Such sources are thought to contain several synchrotron self-absorbed components where the optical depth is unity at different frequencies. This results in a combination of radio spectra that when added together produce an overall radio spectrum that is flatter than $\alpha = -0.7$.

2.7 Polarisation

As discussed in the previous section, radio waves consist of an electric and magnetic field component that are orthogonal to each other. The orientation of the electric field is what describes the polarisation, via the electric vector position angle (EVPA). For a monochromatic electro-magnetic wave we are able to describe the electric field such that for a wave travelling in a $\hat{z}$ direction,

$$\vec{E} = [\hat{x} E_x \exp(i\phi_x) + \hat{y} E_y \exp(i\phi_y)] \exp[i(\vec{k} \cdot \hat{z} - \omega t)], \tag{2.47}$$

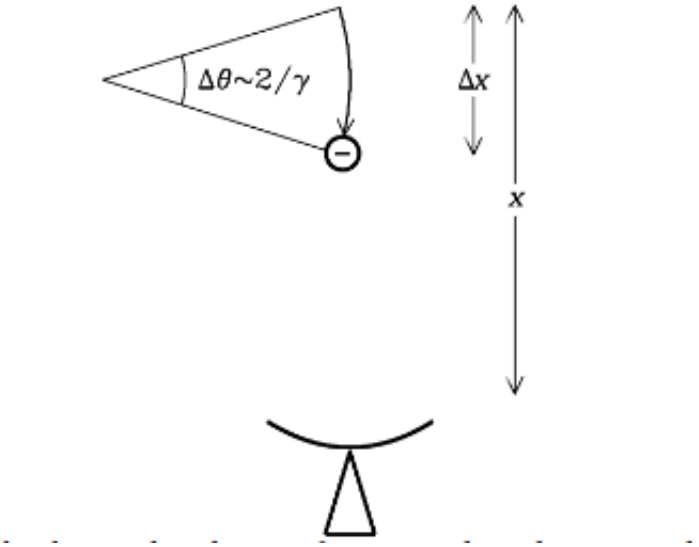

FIGURE 2.9: Illustration taken from Condon and Ransom (2016) depicting an electron moving a distance Δx towards the observer.

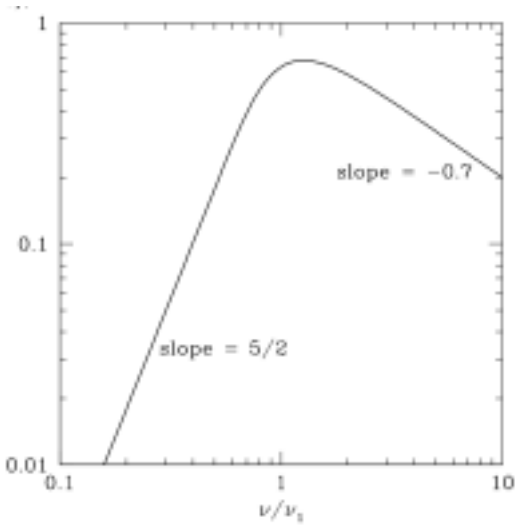

FIGURE 2.10: Spectrum of an optically thick ($\tau \approx 1$) synchrotron source, where there is a sharp fall off due to synchrotron self-absorption ($\alpha = 5/2$) at frequencies when the object becomes optically thick. At higher frequencies, the object is optically thin, with a typical synchrotron spectral index of $\alpha = -0.7$. Taken from Condon and Ransom (2016).

where the wave vector $\vec{k}$ has a magnitude of,

$$|\vec{k}| \equiv \frac{2\pi}{\lambda}, \tag{2.48}$$

in the direction of travel and ω is the angular frequency. The x and y wave components have a phase difference (δ) such that,

$$\delta \equiv \phi_x - \phi_y, \tag{2.49}$$

and the total magnitude of the electric field is,

$$E = \sqrt{E_x^2 + E_y^2}. \tag{2.50}$$

Most combinations of phase and amplitude results in an elliptically polarised wave. Whereas, if the phase difference is 0 the resulting EVPA is linear, and thus, the wave is linearly polarised. If the magnitude of $E_x = E_y$, and there is a phase difference of $\delta = \pi/2$, then the electric field will be circular, and therefore, the wave is circularly polarised. In terms of synchrotron radiation, which we have been focusing on in this thesis, the emission from a single electron should be elliptically polarised (either right handed or left handed polarisation, depending on whether the line-of-sight of our observation falls inside or outside the pitch angle of the emission). However, this right- or left-handed disparity for elliptical polarisation would cancel out in a smoothly varying distribution of multiple particles, and thus, in synchrotron radiation the elliptical polarisation of each particle will cancel out to form a partial linearly polarized source, which is either parallel or perpendicular to the sky plane (Rybicki and Lightman (1985)).

However, in astronomical sources the radiation received is not monochromatic, but contains multiple varying electric fields. These electric fields can therefore be characterized by the four Stokes parameters. The radiation from a frequency range is averaged over time such that the Stokes parameters are,

$$I = \langle E_x^2 + E_y^2 \rangle / R_0, \tag{2.51}$$

$$Q = \langle E_x^2 - E_y^2 \rangle / R_0, \tag{2.52}$$

$$U = \langle 2E_x E_y \cos\delta \rangle / R_0, \tag{2.53}$$

$$V = \langle 2E_x E_y \sin\delta \rangle / R_0, \tag{2.54}$$

where R_0 is the radiation resistance of free space. If the averaged magnitudes of E_x and E_y are equal and the phase of the electric fields are uncorrelated, it follows that $Q = U = V = 0$ and the source is said to be unpolarised. For any polarisation state, I is the total intensity of the source. The VLA, which is used in this thesis, has the capability of measuring the polarisation of the source by having two orthogonally orientated receivers that detect the L and R directions independently (more generally referred to as the left- and right-hand receivers, respectively).

Now that we know where the signal from a radio source is coming from and how it is detected, in the next section we will introduce gravitational lensing, which we use for our tests of dark matter.

2.8 Gravitational Lensing

Gravitational lensing was first considered in 1783, with correspondence sent between John Mitchell and Henry Cavendish. In these papers, John Mitchell postulated a method in which to derive the mass of a star using the reduction in light speed due to the gravitational field of said star. This lead Cavendish to produce the first calculation of the deflection angle of light by the Sun (called the *Newtonian* deflection angle),

$$\Delta\theta \approx \frac{2GM}{c^2R}, \tag{2.55}$$

where $\Delta\theta$ is the level of light deflection, G is the gravitational constant, M is the enclosed mass within a distance R of the star, and c is the speed of light in a vacuum. However, this is half of the value we know today. The difference came from the lack of knowledge at the time about the curvature of space-time around massive objects. This changed in 1916 when Albert Einstein theorised that the deflection of light can rather be described by geodesic lines that travel straight in the curvature of space-time, better known as his General Theory of Relativity (see Meneghetti 2017 for a full derivation). Therefore, the deflection angle (for a point mass lens) will be dependent on the light path through the gravitational potential, such that,

$$\hat{\vec{\alpha}}(b) = \frac{2}{c^2}\int_{-\infty}^{+\infty} \nabla_{\perp}\phi dz, \tag{2.56}$$

where $\hat{\vec{\alpha}}$ is the total deflection angle with impact parameter b. The Newtonian gravitational potential ϕ is assumed to be much smaller than c^2. This assumption allows us to expect a small deflection angle and thus we can integrate over the light path as if it were unperturbed. By assuming the lens as a point mass,

$$\phi = -\frac{GM}{r}, \tag{2.57}$$

we find,

$$\hat{\vec{\alpha}} = \frac{4GM}{c^2b}. \tag{2.58}$$

Here, we now see that Einstein's General Theory of Relativity produces a deflection angle twice that of Newtonian gravity, as proposed in 1783 by Cavendish. This was verified when the Sun was directly observed in 1919 during a solar eclipse by Arthur Eddington (and collaborators) who noted that the positions of stars had shifted by an angle similar to that predicted by Einstein's deflection angle. This was a spectacular success for Einstein's new theory of gravitation.

Thus, with General Relativity we are not only equipped to find the deflection angle, but to also predict the various paths around a mass that produces multiple images, which due to the conservation of surface brightness, will be magnified by the aforementioned mass. It is here where the term "lensing" comes to light, as such objects of significant mass act as a natural telescope, allowing us to see light from distant objects that otherwise could not be observed. The magnification of an object that is lensed is simply the ratio of the intrinsic and observed solid angles, which due to the conservation of surface brightness, is also the ratio of their intrinsic and observed flux-densities,

$$\mu \equiv \frac{S_{\nu,\text{observed}}}{S_{\nu,\text{intrinsic}}}, \tag{2.59}$$

with μ being the magnification and S_ν being the flux density of the source.

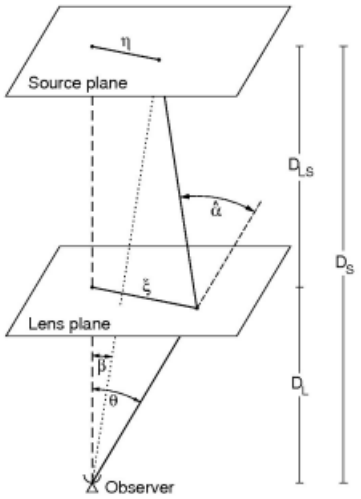

FIGURE 2.11: Sketch of a typical gravitational lens system. Taken from Bartelmann and Schneider (2001).

2.8.1 Lens Equation

In Figure 2.11 we see a schematic layout of a gravitational lens system, with a source at an angular-diameter distance D_S and a lensing mass at angular-diameter distance D_L. The dashed line is the optical-axis, which is perpendicular to the observer and η is the projected angular distance between the source and the optical-axis ($\vec{\eta} = \vec{\beta} D_S$). Similarly to Equation 2.58, we have a deflection angle $\hat{\vec{\alpha}}$ and an impact parameter (previously labelled b in the point mass lens case) $\vec{\xi} = \vec{\theta} D_L$. As mentioned in Section 2.8, we assume these angles to be small (much smaller than a radian), and thus, we define the lens equation as,

$$\theta \vec{D}_S = \vec{\beta} D_S + \hat{\vec{\alpha}} D_{LS}. \tag{2.60}$$

This can be rewritten by defining a reduced deflection angle, such that,

$$\vec{\alpha}(\vec{\theta}) \equiv \frac{D_{LS}}{D_S} \hat{\vec{\alpha}}(\vec{\theta}), \tag{2.61}$$

giving us the standard form of the lens equation,

$$\vec{\beta} = \vec{\theta} - \vec{\alpha}(\vec{\theta}). \tag{2.62}$$

This, in conjunction with Equation 2.58, forms the basis of lensing as from these two equations we are able to investigate the properties of lenses based on their image configuration and mass distributions. For example, lets consider a point-mass as the lens. From Equations 2.58 and 2.62, we obtain,

$$\vec{\beta} = \vec{\theta} - \frac{4GM}{c^2 D_L \theta} \frac{D_{LS}}{D_S}. \tag{2.63}$$

From this, and setting $\beta = 0$, we are able to define the Einstein radius as,

$$\vec{\theta_E} = \sqrt{\frac{4GM}{c^2 \theta} \frac{D_{LS}}{D_S D_L}}. \tag{2.64}$$

By substituting Equation 2.64 into Equation 2.63, we obtain two solutions for θ, and thus two images of the source in the sky are formed at position,

$$\theta_{\pm} = \frac{1}{2}\left[\beta \pm \sqrt{\beta^2 + 4\theta_E^2}\right]. \tag{2.65}$$

Therefore, if $\beta = 0$, that is, the source is directly behind the point mass, θ would be $\pm\theta_E$. Thus, the images would form a ring with radius θ_E, which is generally called an *Einstein ring*. As $\beta \to \infty$, then $\theta_- \to 0$ and $\theta_+ \to \beta$; in this case the source and lens have great enough septation that the source is unlensed. These points are referred to as caustics in the source-plane, or critical curves in the image-plane. They are regions that define the image multiplicity and the magnification of said images.

2.8.2 Lens Potential

In order to understand the gravitational lens observables used within this MSc project, we continue by describing the significance of the lensing potential and its role in the positions, time-delays and magnifications of lensed images.

By combining Equations 2.56 and 2.61, we can define the reduced deflection angle in terms of the Newtonian potential as,

$$\alpha(\theta) = \nabla_{\perp}\left[\frac{D_{LS}}{D_S}\frac{2}{c^2}\int \phi dz\right], \tag{2.66}$$

and,

$$\alpha(\theta) = \nabla_{\theta}\left[\frac{D_{LS}}{D_S D_L}\frac{2}{c^2}\int \phi dz\right], \tag{2.67}$$

where we can define a scalar function $\psi(\theta)$ as,

$$\psi(\theta) = \frac{D_{LS}}{D_S D_L}\frac{2}{c^2}\int \phi dz. \tag{2.68}$$

This scalar function (ψ) is known as the lensing potential and contains all of the information necessary to find the two-dimensional deflection of the light on the sky. From Equation 2.67, we note that the gradient of the lensing potential is the reduced deflection angle. Therefore, the deflections, or positions, of the lensed images are dependent on the first derivative of the lensing potential. Furthermore, the Laplacian (∇_θ^2) of the lensing potential simplifies to,

$$\nabla_\theta^2 \psi = 2\kappa(\theta), \tag{2.69}$$

where κ is the convergence, which is related to the surface-mass density of the lens, and furthermore, is related to the lensing magnification, such that,

$$\mu = \frac{1}{(1-\kappa)^2 - \gamma^2}, \tag{2.70}$$

where μ is the magnification of the lens and γ is the shear. Equations 2.69 and 2.70 are derived in full by Bovy, in preparation. Here, we see that the image magnifications are related to the second derivative of the lensing potential. Thus, from both the positions and the magnifications of the lensed images, we are able to derive information on the lensing potential.

Above, we introduced the convergence, which is defined in terms of the surface-mass density of the lens, such that,

$$\kappa = \frac{\Sigma}{\Sigma_{\rm crit}}, \tag{2.71}$$

where

$$\Sigma_{\rm crit} = \frac{c^2}{4\pi G}\frac{D_S}{D_L D_{LS}}. \tag{2.72}$$

Σ is the surface-mass density of the lens and $\Sigma_{\rm crit}$ is the critical surface-mass density. When $\Sigma \geq \Sigma_{\rm crit}$ the lens will produce multiple images, depending on where the source and lens lie in relation to each other.

For a variable source, another important observable from the lens equation and the lens potential is a geometric and gravitational (Shapiro) time-delay between the lensed images. The time-delay is used later in this thesis when we analyse the variability of our anomalous lens system. The geometric time-delay, taking into account the redshift of the lens, is described as,

$$\Delta t_{\rm geom} = \frac{1+z_L}{2c}\frac{D_L D_{LS}}{D_S} \mid \theta - \beta \mid^2, \tag{2.73}$$

and the Shapiro time-delay is described as,

$$\Delta t_{\rm Shapiro} = -(1+z_L)\frac{D_S D_L}{D_{LS}}\psi(\theta). \tag{2.74}$$

Thus, the combined time-delay for a lens system is,

$$\Delta t_{\rm lensing} = \frac{1+z_L}{c}\frac{D_L D_S}{D_{LS}}\left[\frac{1}{2} \mid \theta - \beta \mid^2 - \psi(\theta)\right]. \tag{2.75}$$

Images form at the extremes of such a time delay surface, the number and positions of these images are determined by the caustics and critical curves of the lens system, which are discussed in the next section.

2.9 Caustics and Critical Curves

In the previous section, we introduced the lens equation and the caustics that are formed by a point-mass lens. Here, we expand on this by looking into more realistic cases for galaxy-scale gravitational lenses. In particular, we focus on a smoothly varying elliptical mass distribution as the lens mass. The simpler case would be to look at a spherical mass model, but these have been shown to be too symmetric, and therefore, are unable to reproduce many of the lensed image configurations that have been observed (Narayan and Wallington, 1992). In the case of a singular isothermal ellipsoid (SIE), we consider the deflection angle (Narayan and Wallington, 1992; Blandford and Kochanek, 1987),

$$\hat{\alpha}_{1,2}(\xi_1, \xi_2) = 4\pi\frac{\sigma^2}{c^2}\frac{(1 \mp \epsilon)\xi_{1,2)}}{[\xi_c^2 + (1-\epsilon)\xi_1^2 + (1+\epsilon)\xi_2^2]^{1/2}} \tag{2.76}$$

where ϵ measures the ellipticity of the lens and the subscripts 1 and 2 correspond to the components along the axes of the elliptical. We consider the distribution to

be isothermal when $\xi_{1,2} < \xi_c$, where ξ_c is the core radius of the mass distribution (Narayan and Wallington, 1992). By using the SIE model, the caustics are no longer a point at the centre of the lens and a ring at θ_E, but instead, as seen in the left panels of Figure 2.12, there is a caustic at the centre, a diamond shape and an elliptical shape in the outer regions. Also seen in Figure 2.12, the multiplicity of the images is dictated by the source position relative to these caustics.

2.10 Mass Distribution

The mass distribution of galaxies have been well studied over years of investigation by astronomers. Through the study of galaxy rotation curves, it has been concluded that galaxies are not only formed with baryonic matter that emits light, but they also contain an encompassing halo structure of satellite galaxies and a dark matter halo. It is this halo that gravitationally holds galaxies together as they spiral at speeds higher than those physically capable if they were only simply composed of their galactic bugle and disk components (Gunn, 1977).

There are currently many predictions for the nature of this halo. Although it is widely accept that simple models of the halo can be described as isothermal and roughly spherical (Navarro, Frenk, and White, 1996) (thus explaining the single isothermal ellipsoid model); what is not yet widely accepted is the type of dark matter mass model that should be applied. Vegetti et al., 2023 discuss these haloes in detail, from cold dark matter (CDM), warm dark matter (WDM) and self-interacting dark matter, to more exotic forms, such as fuzzy dark matter. For the research carried out here, we will focus on CDM haloes, which are predicted to form hierarchically such that low-mass haloes merge to form higher mass structures (Vegetti et al., 2023). This subsequently leads to a high number of low mass haloes, as seen in Figure 2.13; we note the suppression in the number of sub-haloes seen at low masses for the different WDM models, when compared to the predictions for CDM. This is important since these low mass sub-haloes are thought to play a role in our observed flux-ratio anomalies. Therefore, the level of flux-ratio anomaly provides information on the abundance of low mass haloes within lensing galaxies (and along the line-of-sight).

As previously discussed in Chapter 1, the aim of this project is to constrain the properties of dark matter. This can be done through determining the mass-fraction of a lensing galaxy that is composed of sub-haloes f_{sub}. This is defined as the ratio of the total mass in sub-haloes within a projected cylinder of radius double that of the Einstein radius of the lens, and the total mass of the halo within the same cylinder (Hsueh et al., 2019). By conducting a Bayesian inference, we will produce a posterior probability distribution under an idealized CDM model, where the half-mode mass (which is related to the mass of the dark matter particle) is $M_{hm} = 0$ (see Figure 1.1). From this, we derive a mean value of f_{sub}, which will give us an insight into the dark matter distribution present in the halo of our target lens system.

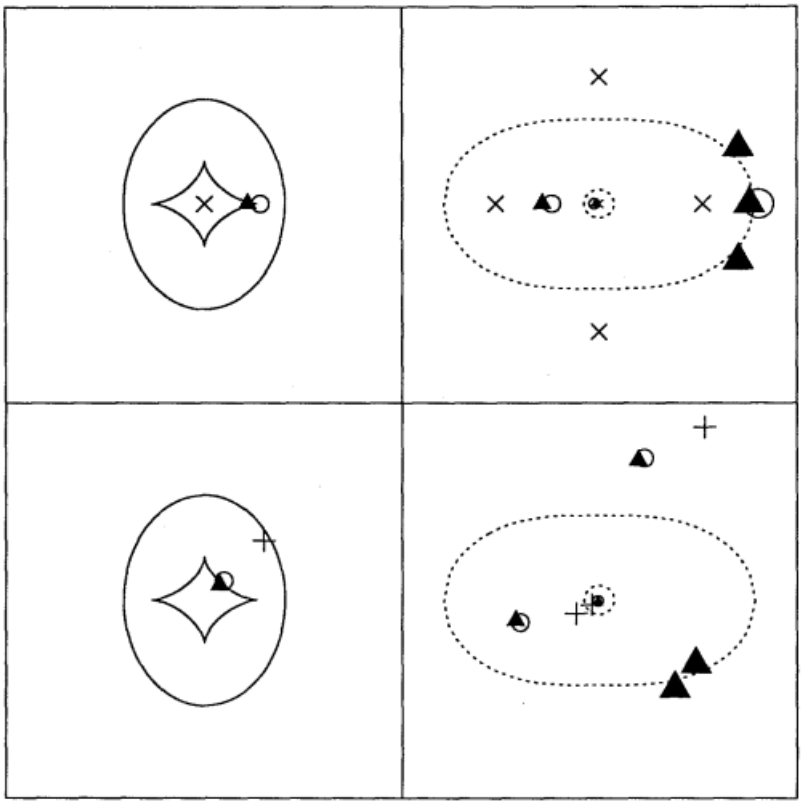

FIGURE 2.12: In the left panels are the caustics, which separate the source-plane into different regions, and in the right panels are the corresponding critical curves in the image-plane. The diamond shaped caustic has two points of interest, the curved lines (called the folds) and the intercept points (called the cusps). In the top panel we see the effect of a source moving across the caustics from the centre to the cusp, as shown by the cross and the triangle (5 image multiplicity) and from the cusp to the outer elliptical, as shown by the circle (3 image multiplicity). Similarly, in the bottom panel we see a source moving across the caustics from the fold, as shown by the cross and the triangle (5 image multiplicity), and from the fold to the outer elliptical, as shown by the circle (3 image multiplicity). Here, we also note one of the images is always near the centre and this image is strongly demagnified if the core radius (ξ_c) is small. Taken from Narayan and Wallington (1992).

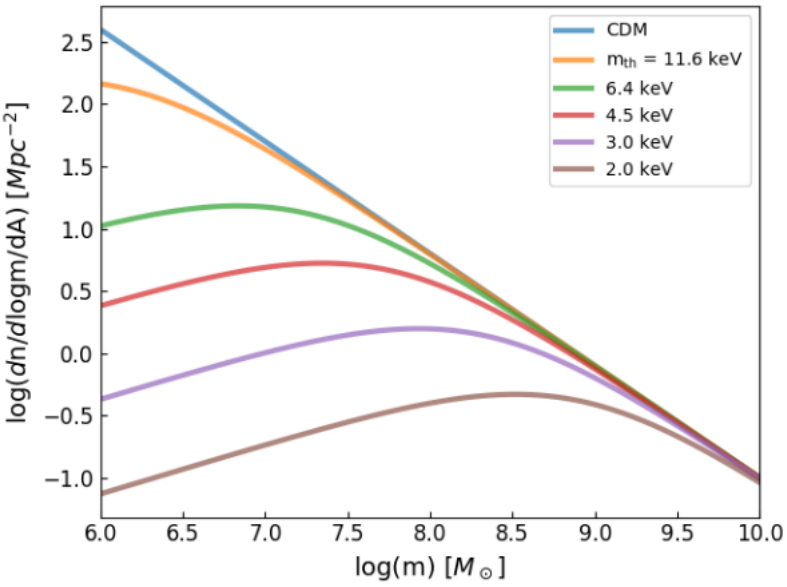

FIGURE 2.13: Sub-halo mass function for CDM and various WDM models. The number of sub-haloes from WDM models is suppressed at low masses with respect to the predictions from CDM. Image taken from Hsueh et al., 2019.

Chapter 3

Scientific Background

In this chapter, we present the scientific background of the research project by discussing topics such as anomalous gravitatonal lens systems, cold dark matter subhaloes, as well as reviewing previous work in the field and introducing our target CLASS B2045+265.

3.1 Anomalous Lenses

In this section, we will be using the tools introduced in Chapter 2 to discuss those gravitational lens systems whose observed properties are inconsistent with a smooth ellipsoidal mass distribution. Here, we focus on so-called "cusp lenses", as seen in the top panel of Figure 2.12, where the source lies close to the cusp of the caustic, and thus produces 5 images (although one of these images is strongly de-magnified). As first suggested by Mao and Schneider (1998), point-sources that are multiply imaged can be well-modelled using a simple elliptical mass distribution. However, for almost all gravitational lenses that produce four images, the observed flux-ratios do not agree with the model-predicted flux-ratios, even though the models are able to accurately predict the image positions.

As can be seen from Equation 2.59, the magnification is directly related to the flux-density of the lensed images, and with this in mind, Narayan and Wallington (1992) derived the following relation for the magnifications of a cusp lens system with a smooth mass distribution,

$$\mu^{(1)} + \mu^{(2)} + \mu^{(3)} = 0, \tag{3.1}$$

where,

$$|\mu^{(2)}| = |\mu^{(3)}| = \frac{1}{2}|\mu^{(1)}|. \tag{3.2}$$

Here, the super-scripts 1, 2 and 3 correspond to the three images with the largest flux-densities. As seen in Figure 3.1, these images correspond to the three squares on the right-hand-side of the right panel, with the central image having the super-script 1, the two outer images having super-scripts 2 and 3 and for completeness the image on the left side of the right panel would have super-script 4 . Here it is important to note that the images within the caustic would have negative magnifications (negative parity) denoting that these images are reversed in one dimension with respect to the images outside the caustic.

Therefore, with all three images having the same intrinsic flux density, we are able to obtain the observed flux ratios. For simplicity, lets call the observed flux density of the central image B, and the observed flux densities of the outer images A and C (in descending order from top to bottom), and the intrinsic flux density of

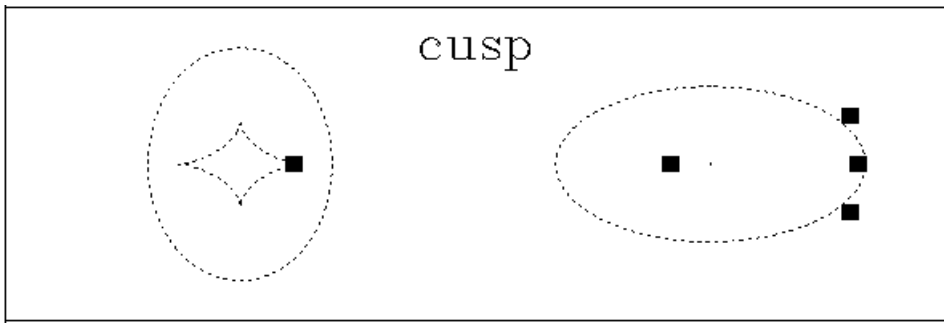

FIGURE 3.1: A simulated singular isothermal ellipsoid (SIE) lens model for a cusp lens system, where we see the source-plane and the caustics with the source represented by a square (left) and the sky plane with the lensed images represented by squares (right). Note that an SIE does not produce a 5th lensed image. This image is reproduced from Keeton, Gaudi, and Petters (2002).

the source I. Therefore, from Equations 2.59 and 3.2, we obtain the following,

$$\frac{|\mu^{(2)}|}{|\mu^{(1)}|} = \frac{A/I}{B/I} = \frac{A}{B} = 0.5, \tag{3.3}$$

$$\frac{|\mu^{(3)}|}{|\mu^{(1)}|} = \frac{C/I}{B/I} = \frac{C}{B} = 0.5, \tag{3.4}$$

and,

$$\frac{|\mu^{(2)}|}{|\mu^{(3)}|} = \frac{A/I}{C/I} = \frac{A}{C} = 1. \tag{3.5}$$

We would therefore expect flux-ratios of A/B and $C/B \sim 0.5$, and $A/C \sim 1$. However, this does not hold true for most cusp lens systems that have been observed. The first lens system where this flux-ratio anomaly was presented is JVAS B1422+231, which we discuss in the next section.

3.2 The First Case: JVAS B1422+231

JVAS B1422+231 is a quadruply-imaged quasar with a characteristic cusp configuration, similar to that seen in Figure 3.1. This lens system was discovered as part of the Jodrell Bank-VLA Astrometric Survey (JVAS) by Patnaik et al. (1992). Since then, there have been multiple unsuccessful attempts to model this system (Hogg and Blandford, 1994; Kormann, Schneider, and Bartelmann, 1994; Keeton, Kochanek, and Seljak, 1997). The general consensus is that although the positions can be recovered, the high-magnifications and the flux-ratios have yet to be reproduced by a model. It has therefore lead to many debates on what could be causing these anomalous fluxes. Some of the current theories include are as follows.

1. Intrinsic variability of the source coupled with a time-delay between the lensed images introduced by the light-path of travel and the gravitational potential may be able to account for the flux-ratio anomaly (Kormann, Schneider, and Bartelmann, 1994). The idea here is that images A and C are observed at a time when the source was brighter as compared to the light coming from image B (Images A, B, C and D of B1422+231 as shown in Figure 3.2). This has essentially been ruled out through monitoring of the system at 5 GHz by Koopmans

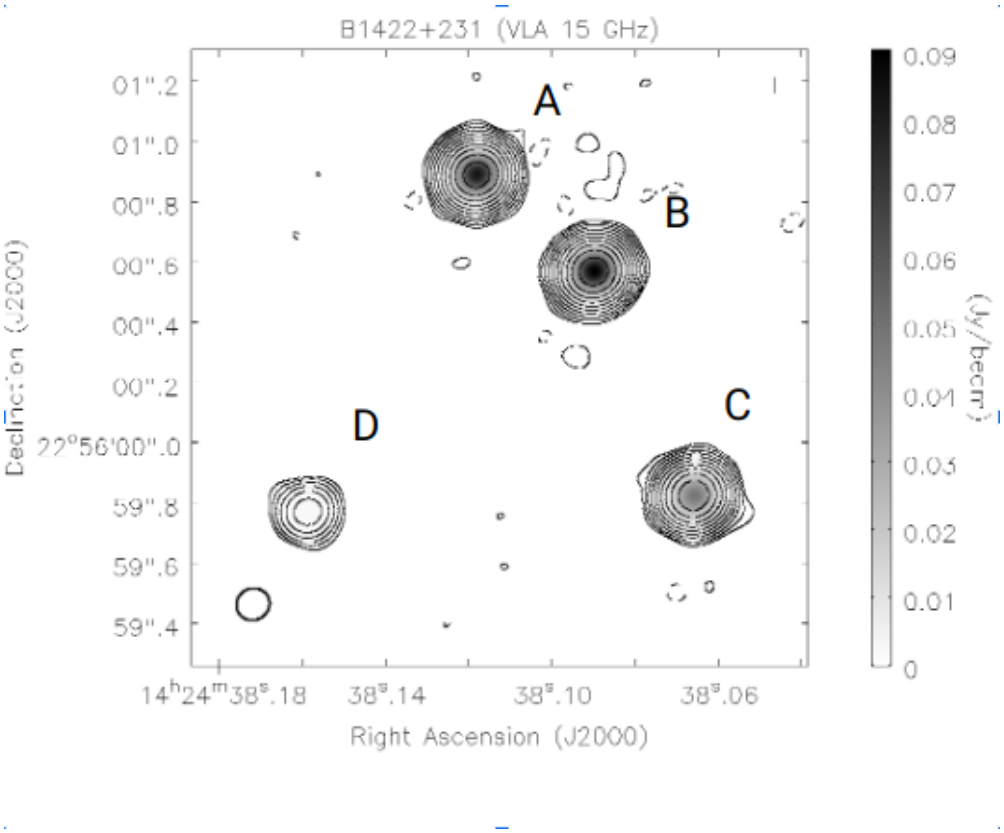

FIGURE 3.2: JVAS B1422+231 observed at 15 GHz with the VLA. The lensed images of the system are labeled A, B, C and D, as per Section 3.1. This image is provided by John McKean.

et al. (2003), and at 8.46 and 15 GHz by Patnaik and Narasimha (2001); see also a recent re-analysis by Biggs (2023).

2. Light attenuation from absorption or scattering affects. As the light from each of the images travels through space, they may separately encounter perturbations along their line of sight. This may differentially affect one image more than the others and produce anomalous flux-ratios. This also seems unlikely, given the similar radio spectra that the lensed images have (Patnaik et al., 1992).

3. Dark matter sub-haloes, as predicted by cold dark matter models may be present in the system (Mao and Schneider, 1998; Nierenberg et al., 2014). These sub-haloes would locally effect the magnification of the individual components. An example of this is shown in Figure 3.3, which is a conceptual visualization of how CDM sub-haloes could effect the flux-ratios of JVAS B1422+231.

The flux-ratio anomaly seen in JVAS B1422+231 is not unique and has been seen in multiple lens systems. For example, CLASS B0128+437, MG J0414+0534, CLASS B0712+472, CLASS B1555+375 and CLASS B2045+265; together with JVAS B1422+231, these five lens systems comprise the Lensing over Frequency and Time (LoFT) sample. Through the research done in this project, we have focused on CLASS B2045+265, where we have taken into account the aforementioned possibilities of intrinsic variability, light attenuation and cold dark matter sub-haloes. We now give a summary of the properties of this system.

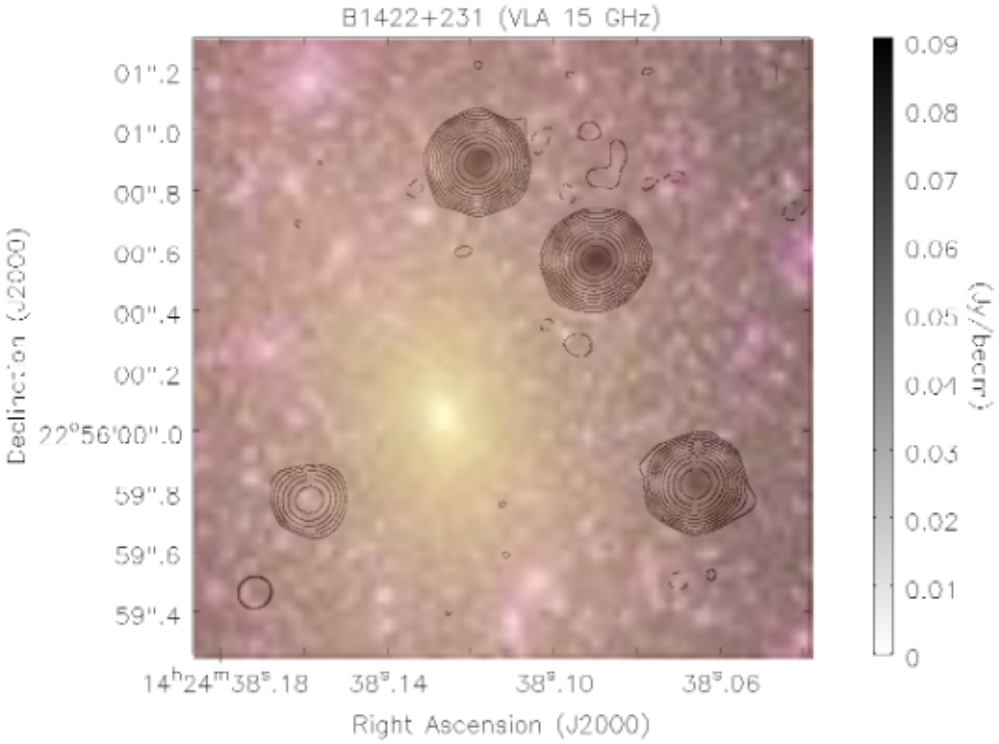

FIGURE 3.3: A visual representation of what a possible CDM model may look like, with the contours of JVAS B1422+231 overlayed. Here we see a strong concentration of dark matter in the centre of the image where we would expect the lensing galaxy to be, but also smaller clumps with a random distribution spread around the field-of-view. These clumps have a distribution such that some are close to the lensed images. These CDM sub-haloes will locally effect the magnification of the individual components. This image is provided by John McKean.

3.3 Our Target: CLASS B2045+265

Between 1994 and 1998, the Cosmic Lens All-Sky Survey (CLASS; Browne et al. 2003; Myers et al. 2003) was carried out with the VLA in A-configuration at 8.46 GHz over three observing seasons. The goal of CLASS was to image a sample of 16 503 flat-spectrum radio sources to search for gravitational lenses. From a complete sample of 11 685 sources, 22 gravitational lenses were discovered. As part of the second phase of CLASS, in September 1995, CLASS B2045+265 was clearly identified as a gravitational lens system with four lensed images, and a fifth radio-loud component that has since turned out to be associated with an AGN within the lensing galaxy (Fassnacht et al., 1999). The radio spectra of the four lensed images between 1.4 and 15 GHz were found to be very similar. From optical spectroscopy, the lensing galaxy redshift was found to be $z_l = 0.8673 \pm 0.0005$. However, only a single broad emission line was detected from the background source, and so, its redshift remains uncertain. Follow-up high angular resolution imaging in the near infrared, using the adaptive optics system of the W. M. Keck Telescope by McKean et al. (2007), found a possible luminous sub-halo associated with the system. This is now thought to be a foreground star in the Milky Way due to it no longer being seen in the system due to its proper motion (John McKean, private communication). VLBI imaging with the VLBA (see Figure 1.3) found that the lensed images, and the emission from the lensing galaxy to be dominated by a compact component, but with a hint of extension seen in lensed images A and C (McKean et al., 2007).

Gravitational lensing mass models for CLASS B2045+265, in which a smooth mass distribution in the form of a singular isothermal ellipsoid (SIE), have been successful in reproducing the positions of the lensed images and their VLBI detected components, but these models are unable to explain the observed flux ratios. McKean et al. (2007) and Koopmans et al. (2003) quantify the level of the flux-ratio anomaly using the $R_{\rm cusp}$ parameter (Bradac, M. et al., 2002; Keeton, Gaudi, and Petters, 2003),

$$R_{\rm cusp} = \frac{\mu_A + \mu_B + \mu_C}{|\mu_A| + |\mu_B| + |\mu_C|}, \tag{3.6}$$

where μ_A, μ_B and μ_C are the magnifications of images A, B and C, respectively. Here, it is again important to note the parities of the images, where μ_B would have a negative parity. For a true-cusp lens system, we expect $R_{\rm cusp}$ to tend to 0. However, CLASS B2045+265 has a value of $R_{\rm cusp} = 0.501 \pm 0.035$, which is actually the most extreme flux-ratio anomaly within the LoFT sample (Koopmans et al., 2003). CLASS B2045+265 thus has a similar issue as JVAS B1422+231, where we have yet to accurately model the lens system with a smooth mass distribution. This is why, as part of this project, we have observed CLASS B2045+265 over a large time-range and large frequency bandwidth. This has allowed us to investigate the nature of the flux-ratio anomaly in CLASS B2045+265 deeper, and allowed us to rule-out possible causes, as postulated in Section 3.2.

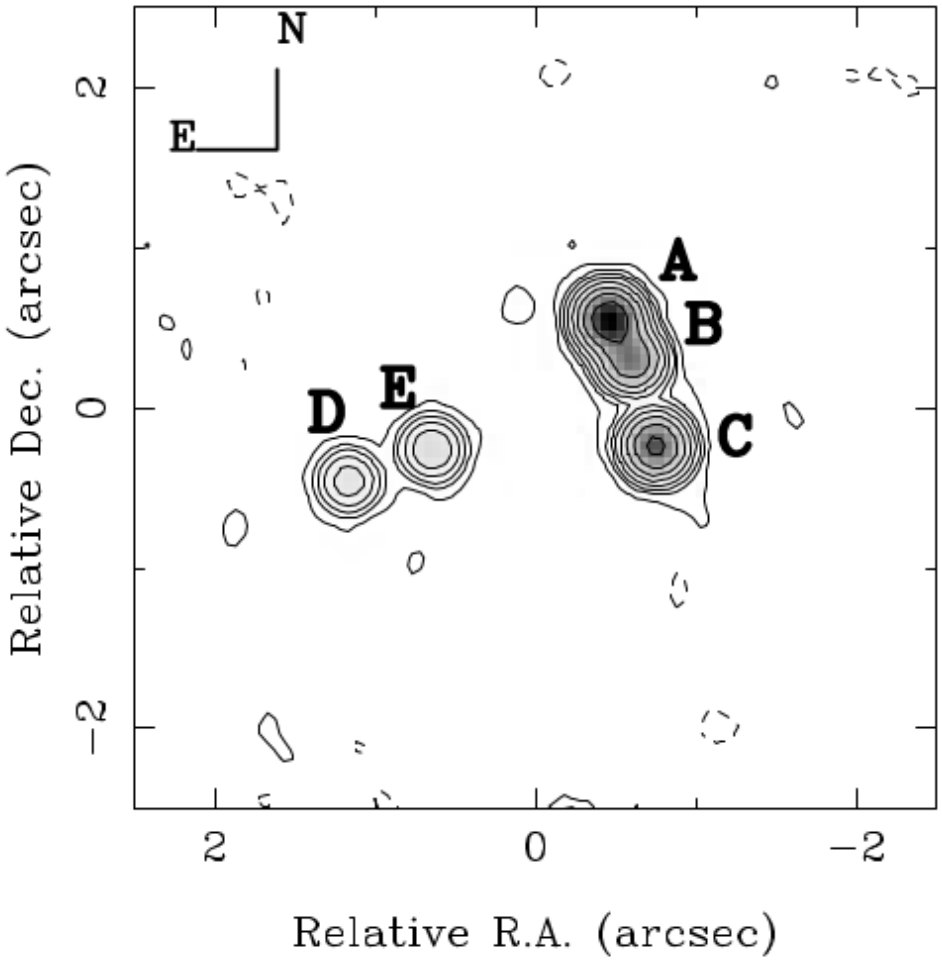

FIGURE 3.4: 8.46 GHz image of CLASS B2045+265 taken with the VLA in December 1996. The lensed images are labeled A, B, C and D, and the lensing galaxy, which is also radio-bright, is labeled as E. Taken from Fassnacht et al. (1999).

Chapter 4

Data

In this Chapter, we present the observational data that are used throughout this thesis, and the processes applied to produce science ready images and visibilities that could be used to measure the flux-ratios of our target CLASS B2045+265.

4.1 Observations

The data used in this thesis were collected between 2022 March 15 and 2022 May 17 using the VLA in A-configuration. We monitored six gravitationally lensed radio sources in total between 12 and 18 GHz for 20 epochs as part of the observing project 22A-388 (PI: McKean). In this thesis, the data for three of the lensed radio sources are analysed, although our final results are based on one of them. The two other lenses that were analysed are the subject of a BSc thesis (Vrints; RuG) and a PhD thesis (Ndiritu; RuG and MPA) of two other students working as part of the Lensing over Frequency and Time (LoFT) team. The lensed radio sources that we worked on here are JVAS B1422+231, CLASS B1555+375 and CLASS B2045+265; all of which are known to exhibit a flux ratio anomaly. For this thesis, we will be focusing on the results for CLASS B2045+265.

For each epoch, JVAS B1422+221 was observed for 6.7 min, whereas CLASS B1555+375 and CLASS B2045+265 were observed 8 min each as part of an observing block that lasted for one hour to aid scheduling. The Ku-band receiver was used in 3-bit mode, which provided a continuous bandwidth between 12 and 18 GHz. This bandwidth was divided into three base-bands that each contained 16 spectral windows, with 64 channels each that were 2 MHz in width. The visibility integration time was 2 s. The data were recorded in left (L) and right (R) circular polarisations, which were correlated to produce the RR, LL, RL and LR correlations (full-polarisation). 3C 286 was observed as the (primary) absolute and polarisation flux density calibrator and as the polarisation position angle calibrator, and J1407+2827, J1625+4134 and J2023+3153 were observed as the (secondary) phase, delay and bandpass calibrators of JVAS B1422+231, CLASS B1555+375 and CLASS B2045+265, respectively. Note that only one observation of each phase reference source was carried out to maximise the amount of time on each target, and because phase self-calibration could be employed later. Finally, a longer observation of J1407+2827 was carried out since it was also used to determine the polarisation leakage.

4.2 Data Reduction: Stokes I

We used the Common Astronomy Software Applications (CASA; CASA Team et al. 2022) package to produce calibrated data. In Figure 4.1, we present the standard

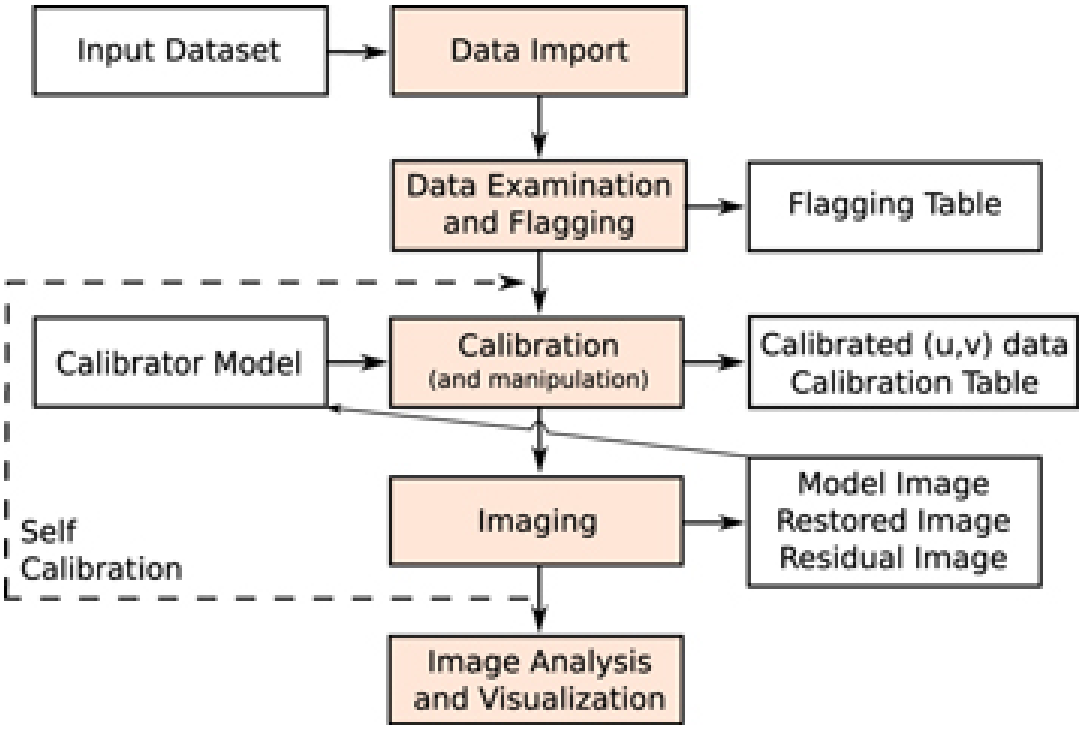

FIGURE 4.1: Workflow of a general CASA data reduction pipeline taken from CASA Team et al. (2022).

CASA work flow diagram, which formed the basis of the pipeline implemented for calibrating our data for JVAS B1422+231, CLASS B1555+375 and CLASS B2045+265.

As mentioned above, our data set was taken using the VLA in A-configuration (see Figure 2.3). Since interferometers are sensitive to the relative phase differences between the visibilities, a reference antenna is normally used from which all calibration solutions are determined relative to. We chose antenna ea10, which is near the centre of the array and hence had many short baselines (with the highest signal-to-noise ratio and simplest source model), as our reference antenna for 19 of the 20 epochs; in the 16th epoch, antenna ea10 was offline, and we therefore chose ea23 as an alternative reference antenna. Following the work flow, after importing our data sets into CASA and doing an apriori calibration with the task *gencal* (corrections done for opacity, antenna elevation, the sampler quantisation and the antenna positions, based on data collected by the VLA), an examination was done on the data where we manually flagged any bad antennas, time-ranges or channels that were obviously outliers using the *flagdata* task. In addition, the "quack" flagging process within *flagdata* was employed to remove the set of visibilities at the beginning of each scan due to the movements of the VLA dishes. Finally, (automatic) flagging in time and frequency, based on the visibility statistics, was used to remove any residual and frequent radio frequency interference that was difficult and/or time-consuming to identify and remove manually.

3C 286, which is a known calibrator with a well defined model, was used to calibrate the flux-density scale of our observations. The nature of 3C 286 whereby there is no detectable variations in total flux density or polarized emission makes it uniquely valuable as a calibrator as noted in Perley and Butler, 2017. By comparing the observed visibility amplitudes to the known model visibility amplitudes for 3C 286 (which in the case of our pipeline we used the Perley and Butler 2017

model at Ku-band) we can derive the calibration solutions with respect to some absolute flux-scale. These calibration solutions can then be compared with those for the phase-reference calibrators in order to obtain the correct flux-density scale and spectrum for our target object. In terms of CASA, the function *setjy* is used to generate the model visibilities for 3C 286 (see Figures 4.2 and 4.3 for an example of the raw and model visibilities of 3C 286 for one of the visits). This is followed by a short (single integration; 2 s) phase-calibration step where, using a small frequency interval of 8 MHz to minimize delay errors, we create a correction table for the time-dependent and frequency-independent complex gains on short time-scales. This is done using *gaincal*, with gain type G in phase-only calibration mode. Next, another *gaincal* calibration is done with gain type K, which solves for residual delays to our reference antenna, that is, solves for the phase as a function of frequency. Once this is done, we correct for the spectral response of each spectral window using the task *bandpass*. This solves for the amplitude as a function of frequency.

At this point, we have derived corrections for the phase and amplitude as a function of frequency, which now allows us to solve for these as a function of time, using the full bandwidth of each spectral window. Again, using the function *gaincal* with gain type G, we create phase-only calibration tables for every visibility integration for 3C 286, as well as for each of the phase-reference calibrators (J1407+2827, J1625+4134 and J2023+3153). This is followed by creating the amplitude gain tables using *gaincal* with gain type G and using the amplitude and phase calibration mode. Here, we used a solution interval that is equal to the scan time since the solutions are expected to vary slowly in time and to maximise the signal-to-noise ratio.

Our next step was to determine the model for the phase-reference calibrators, which up until now had been assumed to be point sources with an amplitude of 1 Jy. Using the task *fluxscale*, we compare the solutions of 3C 286 and the phase-reference calibrators to determine their flux-density as a function of frequency, that is, their spectrum (see Figure 4.4). Again, using the task *setjy*, we generate a set of model visibilities, but now for the phase-reference calibrators. We then repeat the steps we used above for our phase-reference calibrators to derive better amplitude and phase solutions. These new gain tables are then applied to create the corrected data, with 3C 286 having its own tables applied, and the phase-reference calibrators J1407+2827, J1625+4134 and J2023+3153 having their respective calibration tables applied to themselves and the targets JVAS B1422+231, CLASS B1555+375 and CLASS B2045+265, respectively. Finally, a radio frequency interference flagging step is applied to the corrected data. From this we obtain the final calibrated data for 3C 286, as presented in Figure 4.5, and our target sources, as presented in Figure 4.6. Although the results shown are based on the first visit from our data, this process was repeated for all 20 visits.

4.3 Data Reduction: Stokes Q and U

Our pipeline also includes an additional section for polarisation calibration. Thus far, we have only been working with the RR (right-hand) and LL (left-hand) correlations, which are combined to form the Stokes I (total intensity). Here, we calibrate the RL and LR (cross-hand) correlations, which measure light that has been polarised and can be combined to form the Stokes Q and U. The gain tables that we solve for are only for 3C 286 (to correct for the polarisation angle) and J1407+2827 (to correct for the polarisation leakage). First, we use *gaincal* with type Kcross to correct for the antenna cross-hand delays of the RL and LR data channels. This is followed by

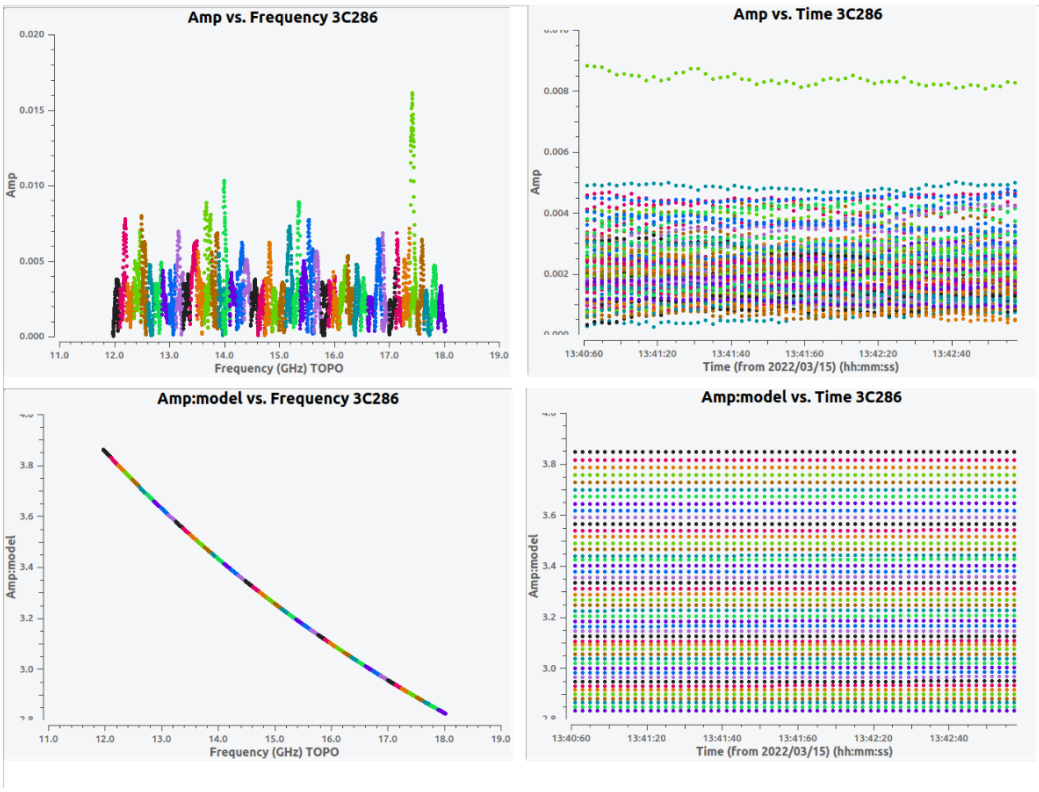

FIGURE 4.2: The visibility amplitude as a function of frequency (left), and the visibility amplitude as a function of time (right) for 3C 286, based on the first visit (2022 March 15), made using the CASA task *plotms*. The top panels are the raw visibilities and the bottom panels are the model visibilities, from the Perley and Butler (2017) model for 3C 286 at Ku-band. All plots show only the RR and LL correlations, have been colourised by spectral window, and have been averaged in time or frequency, and over all baselines, for clarity.

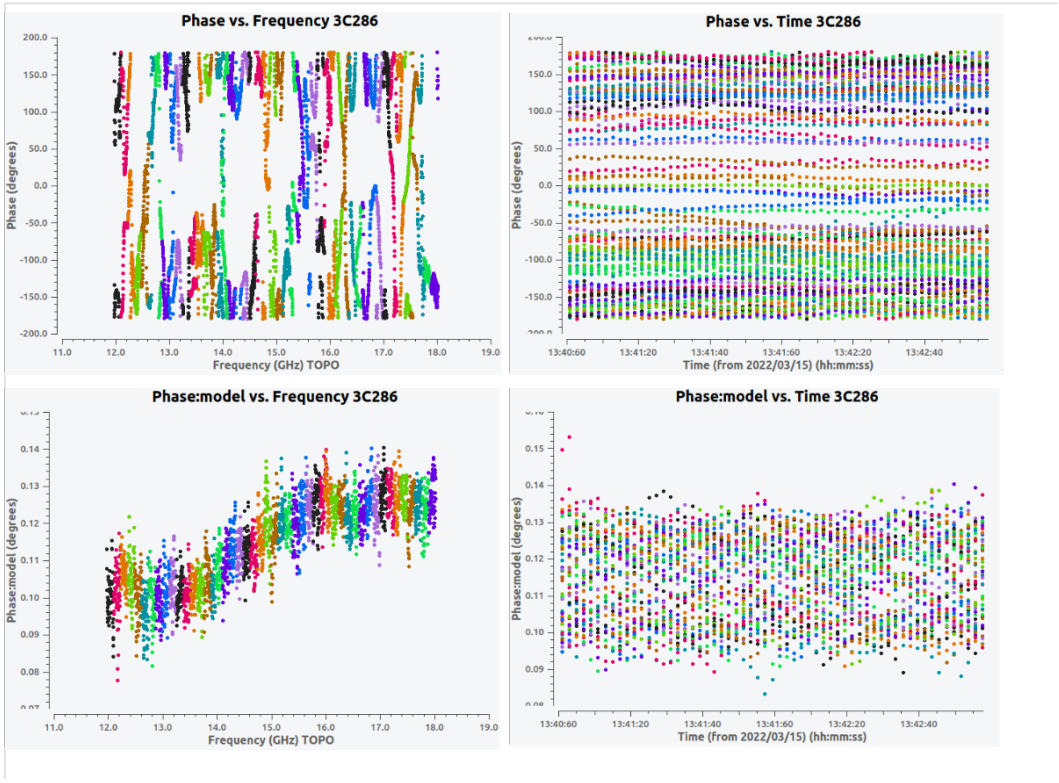

FIGURE 4.3: The visibility phase as a function of frequency (left), and the visibility phase as a function of time (right) for 3C 286, based on the first visit (2022 March 15), made using the CASA task *plotms*. The top panels are the raw visibilities and the bottom panels are the model visibilities, from the Perley and Butler (2017) model for 3C 286 at Ku-band. All plots show only the RR and LL correlations, have been colourised by spectral window, and have been averaged in time or frequency, and over all baselines, for clarity.

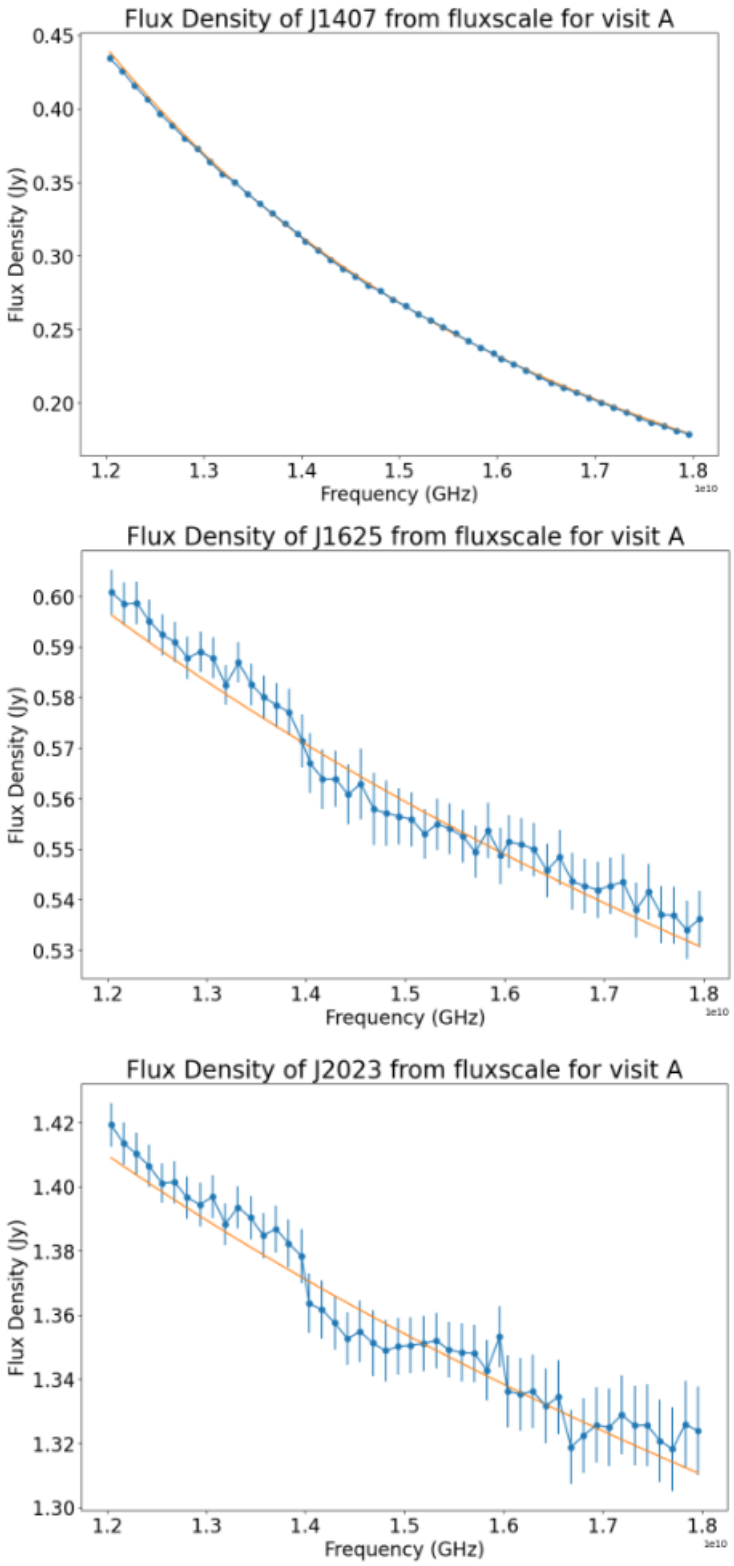

FIGURE 4.4: Second order polynomial model (orange) of the flux-density as a function of frequency determined using the CASA task *fluxscale* for the phase-reference calibrators J1407+2827, J1625+4134 and J2023+3153, based on the bootstrap calibration for the first visit (blue) (2022 March 15). We see that there is significant scatter in the data, as a result of using the solutions for 3C 286 to calibrate the flux-scale. By using the new models for the phase-reference sources, we reduce this scatter and the variations from spectral window to spectral window. It is noted that J1407+2827 has smaller error bars and a better fit because it was observed for a longer time (for the polarisation calibration).

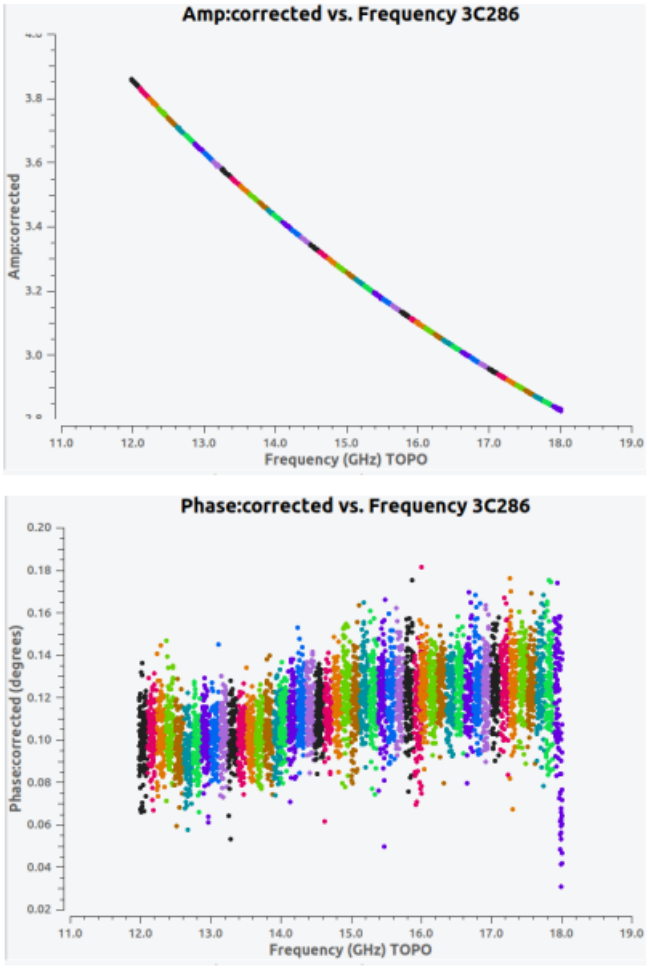

FIGURE 4.5: The corrected visibility amplitude (top) and phase (bottom) as a function of frequency for 3C 286, based on the first visit (2022 March 15), made using the CASA task *plotms*. By comparing these with the data presented in Figures 4.2 and 4.3, we see that the calibrated visibilities are a close reflection of the model visibilities. All plots show only the RR and LL correlations, have been colourised by spectral window, and have been averaged in time and over all baselines, for clarity.

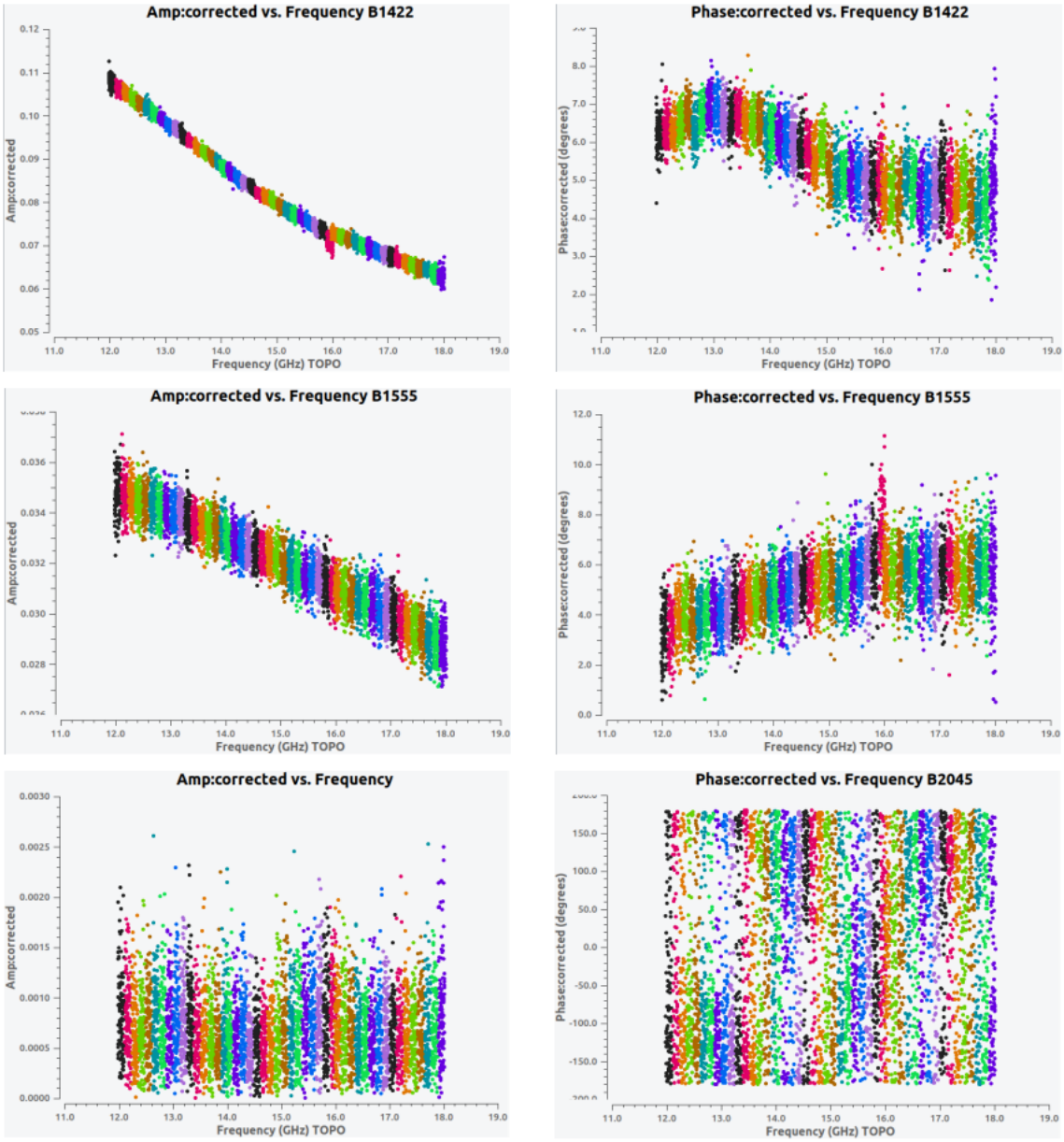

FIGURE 4.6: The corrected visibility amplitude (left) and phase (right) for our target sources JVAS B1422+231 (top), CLASS B1555+375 (middle) and CLASS B2045+265 (bottom), after all the gain tables have been applied. We see there are offsets in some spectral windows, which is likely due to residual radio frequency interference that remained throughout the calibration process.

using *polcal* to solve for the systematic calibration gains in the polarisation effects. *polcal* is used with type Df to solve for the polarisation leakage (where polarisation for one polarisation channel has been incorrectly detected in another due to imperfections, calibration errors, or misalignments in the system) , and then with type Xf to solve for the cross-hand phases. These tables are then applied to each of the calibrators and the target sources. We verify the calibration by inspecting the resulting polarisation angle and flux for 3C 286 using *plotms*. We note that the phase-reference sources are polarised at the few per cent level between 12 to 18 GHz, except for J1407+2827, which is confirmed to have no polarised flux.

4.4 Self-Calibration

The final step of the our calibration pipeline extracts the calibrated visibilities for the three basebands using the CASA task *split*. We then converted them into uvfits format using the task *exportuvfits* for the next step in the process, called self-calibration, which we describe in this section. From this point, we will be exclusively focused on the target source of this thesis, CLASS B2045+265.

For the self-calibration step, we opted to use the interactive imaging, calibration and model fitting package, Difmap (Shepherd, 1997). Difmap gets its name from the process of difference mapping, where a model is produced by iteratively cleaning the pre-calibrated data and inspecting the residuals. This model is then used for the calibration of the data; hence the name, self-calibration. In Figure 4.7, we show the dirty images of each of the three 2 GHz basebands using the pre-calibrated data from Section 4.2. For each of these images, we have used only the RR and LL correlations (Stokes I) and have used a uniform weighting of the visibilities. From these images, we do not see signs of extended structure and only four components of the system can be seen as fairly uniform "blobs" (these are the three brightest lensed images and the lensing galaxy). We used the central baseband to derive a starting model for the data set. For this, we first used a set of delta functions to describe the observed surface brightness distribution. We used the Difmap *clean* function to build the model for our data. Cleaning is an iterative process in which we extract a fraction (in our case 1%) of the peak surface brightness within pre-defined regions, which are called clean-boxes, until our model is a good representation of the data and we see mostly noise after removal of the flux. This became our initial model that we calibrated the data against. This process is repeated several times until we saw no major improvement in the image residuals.

With the improved calibration, we then created a new model that was based on fitting a single elliptical Gaussian model component to each lensed image and to the emission from the lensing galaxy. We then iteratively self-calibrated against this Gaussian model, improving it with additional model fitting. Strictly, the best calibration will come from the best model, and we have made an assumption that the source is well-represented by an elliptical Gaussian. Given the VLBI imaging of McKean et al. (2007), this seems a reasonable approximation. However, we also found that such a model produced a better rms (root mean square) map noise when compared to the results using a model composed of delta functions; we note that the model for each lensed image is certainly not consistent with a set of four delta functions (20 components in total), as was produced from cleaning. The final self-calibrated image produced from Difmap for the 14 to 16 GHz baseband data is given in Figure 4.8. The resulting five-component Gaussian model is what we will refer to as our base model.

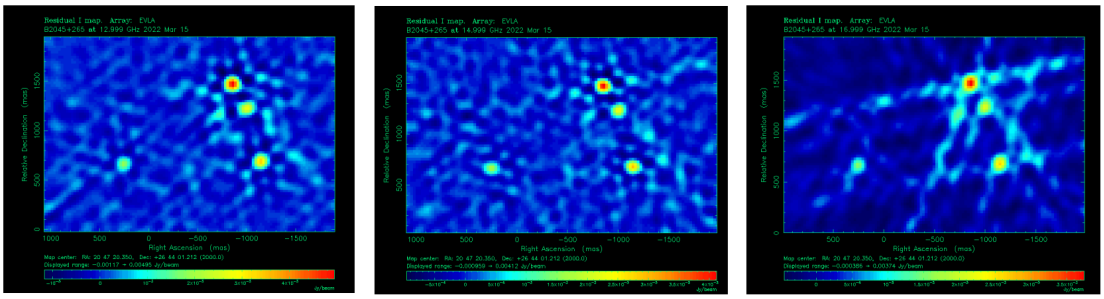

FIGURE 4.7: Imaging (dirty) of the CLASS B2045+265 pre-calibrated data from the three basebands at frequencies between 12 to 14 GHz (left), 14 to 16 GHz (middle) and 16 to 18 GHz (right), after running our CASA calibration pipeline. Each of these images are for Stokes I, and use uniformly weighted visibilities.

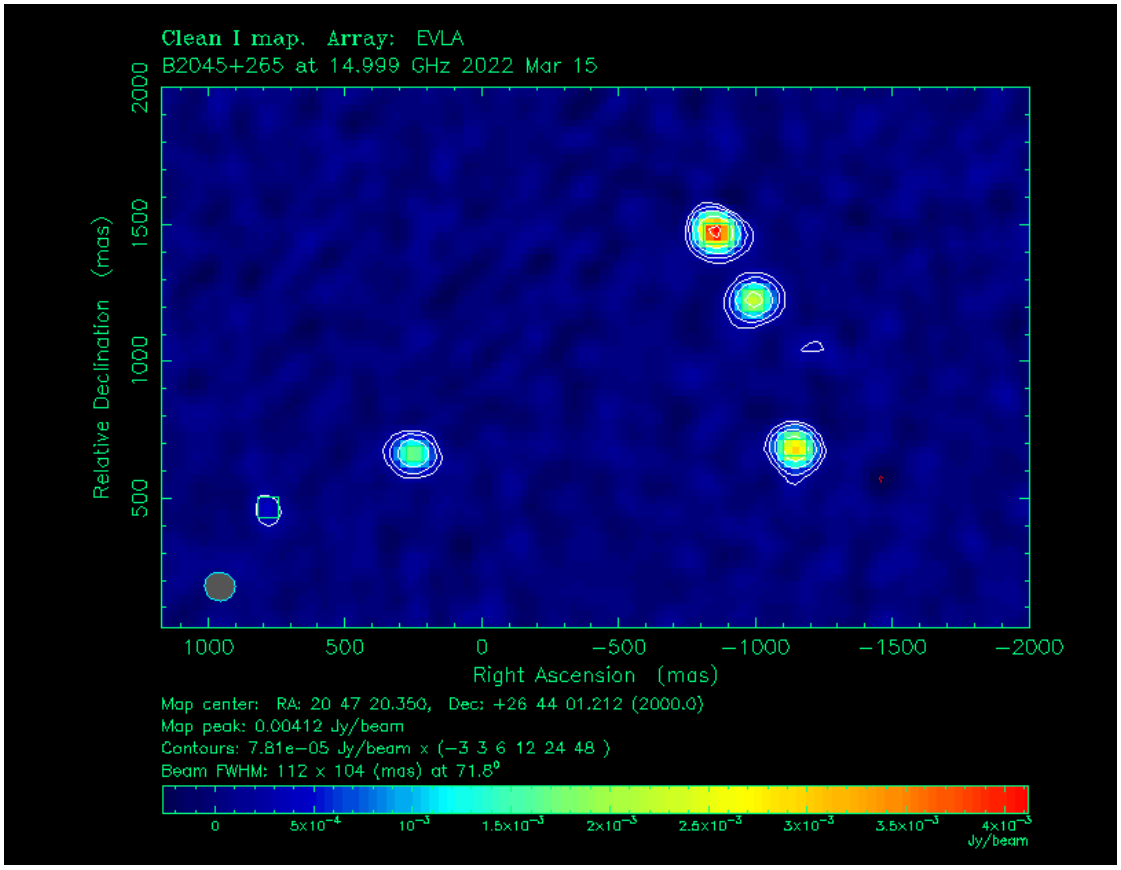

FIGURE 4.8: Final de-convolved image of CLASS B2045+265 using the self-calibrated data from the baseband at 14 to 16 GHz. Note that all four lensed images are detected, as well as the lensing galaxy.

We next use the base model as a starting point to self-calibrate the individual spectral windows, called intermediate frequencies in Difmap, for each visit. During self-calibration, the absolute positional accuracy is lost as the model fits for the relative positions of the components, which can drift away from the true positions during multiple runs of self-calibration. Therefore, to ensure that the different spectral windows were astrometrically aligned, we fixed the positions for the five elliptical Gaussian components in our model. Later, when we fit to individual channels, the low signal-to-noise ratio resulted in poor model fits. Therefore, we also fixed the model parameters, and allowed only for the flux-density of the model components to vary.

We started by doing a phase-only self-calibration in Stokes I by loading in our base-model to Difmap, and running the task *selfcal*, along with our desired solution interval. In this case, we used time intervals of 5 minutes and 1 minute, with additional model-fitting after each self-calibration to update the model. The correct interval to be used was not intuitive; if too long, we may not correct for all of the phase variations, and if too short, the signal-to-noise ratio of the data may be too low to derive good solutions. Thus, we ran this step multiple times with many different variations to the solution interval to test the results. We tried to avoid either over or under calibrating the data, and found that the best solutions were produced with a 5 minute and then a 1 minute interval. Through these tests, we did find that it was difficult to identify when the data were over-calibrated for the Stokes I. However, when we looked at the resulting polarised images in Stokes Q and U, we could clearly see when we were over-calibrating the data. This is demonstrated in Figure 4.9, where we see the difference in the quality of the calibration when 30 seconds is used for the phase-only self-calibration solution interval, which seems to over-calibrate the data, when compared to when only a 5 and 1 minute self-calibration solution interval was used. A test was also conducted using a long solution interval of 30 minutes, but this had little affect on our results when compared to the 5 and 1 minute strategy, since it was much longer than the integration time used for the target. After each of these phase-only self-calibration loops, we used the function *modelfit* to re-fit our Gaussian model components to the visibility data; this is done for 10 fitting iterations and outputs the flux density, position (radius and angle from the phase centre), axis-ratio, major-axis and position angle of the Gaussian models, and their errors. As we keep most of the model parameters fixed, only the flux density and the error are the main outcomes from this step.

Next, with our best model for the target, we apply amplitude self-calibration using the Difmap function *gscale*, which requires no input parameters since it provides normalised antenna-based corrections with a solution interval that is the length of the observation. We run this function twice, until all the amplitude corrections for each telescope are ~ 1 (i.e. no additional correction needed). As above, *modelfit* was run to update the source model after our first *gscale*.

The final step was to obtain a clean image and retrieve the flux-density of each component. This was done by reading in the base model we created from our 14 to 16 GHz baseband data (Figure 4.8) and then re-fitting the model to our self-calibrated data, again using *modelfit*. The outputted values from this final model-fit are the flux-density of each component and a final de-convolved (clean) image. This was done for each spectral window in Stokes I, Q and U, and per channel for Stokes I.

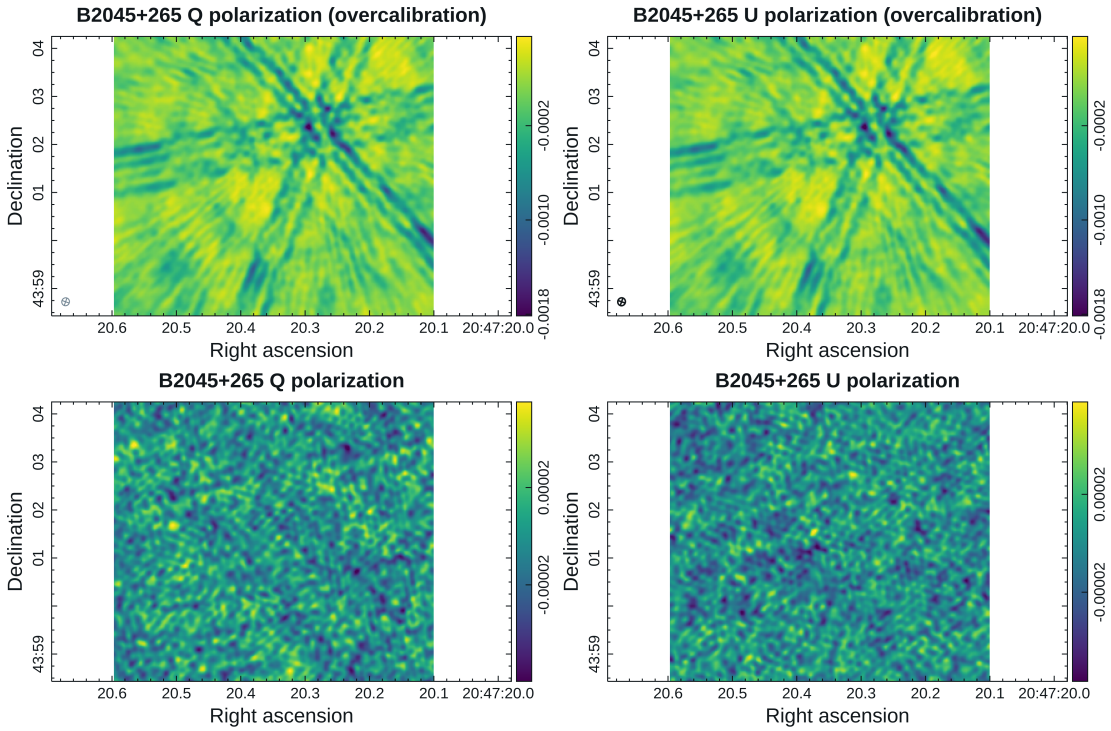

FIGURE 4.9: An example of the different results obtained for various self-calibration solution intervals done with the Stokes I data and applied to the Stokes Q (left) and U (right) data. In the top panels are the results of a 30 second phase-only sellf-calibration solution interval, after 5 and 1 minute solution intervals have been used. In the bottom panels are the results from only using 5 and 1 minute solution intervals. From these images we note that the beam patterns seen in the top panels are due to over-calibration from the 30 second solution-interval step. Therefore, we exclude it in our final calibration and use only a 5 and 1 minute solution interval.

4.5 Final Imaging in Stokes I, Q and U

Having a complete data set over the frequency range of 12 to 18 GHz that was taken over 20 visits provides an extremely deep observation of 160 min over a 6 GHz bandwidth for our target. As part of our imaging and self-calibration pipeline within Difmap, we also produced deconvolved (clean) image at each of the three basebands (12 to 14, 14 to 16, and 16 to 18 GHz), which are saved as a *fits* image for the Stokes I, Q and U, as well as the corresponding residual images (with the Gaussian model subtracted, in the case of Stokes I). Thus, for each of our 20 visits we have an image for each polarisation, as well as three images of the residuals, which are combined to produce a set of stacked images. This process averaged the observed flux-density and the rms of 60 images for each polarisation, and thus, provides the best possible image of B2045+265 with the lowest rms.

Chapter 5

Results

From the previous Chapter, we have now successfully completed the calibration and self-calibration of our data, and the model-fitting to obtain the flux-density for each component per channel (and spectral window). This corresponds to a flux-density measurement at 2 MHz intervals between 12 and 18 GHz for each visit. We therefore have many measurements of the components as a function of frequency and time, and in this chapter, we present the images of CLASS B2045+265 in Stokes I, Q and U, and we discuss the radio spectra and the flux-ratios of the lensed images that we derive from these measurements.

5.1 The Stokes I, Q and U Imaging of CLASS B2045+265

In Figure 5.1, we present the stacked Stokes I image of CLASS B2045+265 between 12 and 18 GHz (central frequency of 15 GHz). This image is made using a natural weighting of the visibilities, which produces a synthesised beam size of 0.169×0.141 arcsec at a position angle of -26.1 degrees (note that this is the average beam size of the 20 visits). The rms map noise is 2.6 μJy beam^{-1}, which is in excellent agreement with the expectations, given the 6 GHz bandwidth and the 160 mins on-source integration time (as derived from the VLA Exposure Time calculator). From Figure 5.1, we see that all four lensed images have been detected at high significance, as is the emission from the lensing galaxy. Immediately from this image, we see that, as previously observed in 1998 with the VLA (see Figure 1.2), the lensed images present the same flux-ratio anomaly (this will be further quantified below). Therefore, the flux-ratio anomaly has persisted for almost 25 years.

In a recent analysis of the gravitational lens system JVAS B1422+231 by Biggs (2023), where monitoring data was similarly stacked together, faint extended emission was found between the lensed images. Such emission can potentially provide additional constraints to the gravitational lens mass model. Motivated by this, we have also stacked the model-subtracted images of the Stokes I emission, which we show in Figure 5.2. We see that there is no additional emission present in this rather deep image of the system. Therefore, we confirm that the lensed source is core-dominated on these scales, and that there is no extended emission present in our data. We do note that there is some evidence of residual side-lobe emission. This is either due to low level calibration errors that remain in the visibility data or due to an imperfect removal of the source emission over the wide bandwidth that we imaged.

We have also made images of the stacked Stokes Q and U surface brightness for the target, as presented in Figures 5.3 and 5.4, respectively. As noted during the calibration process, we see no evidence of any emission in the Stokes Q and U from CLASS B2045+265 above the 5σ-level ($S_{Q,U} < 13$ μJy; point-source). Given that the

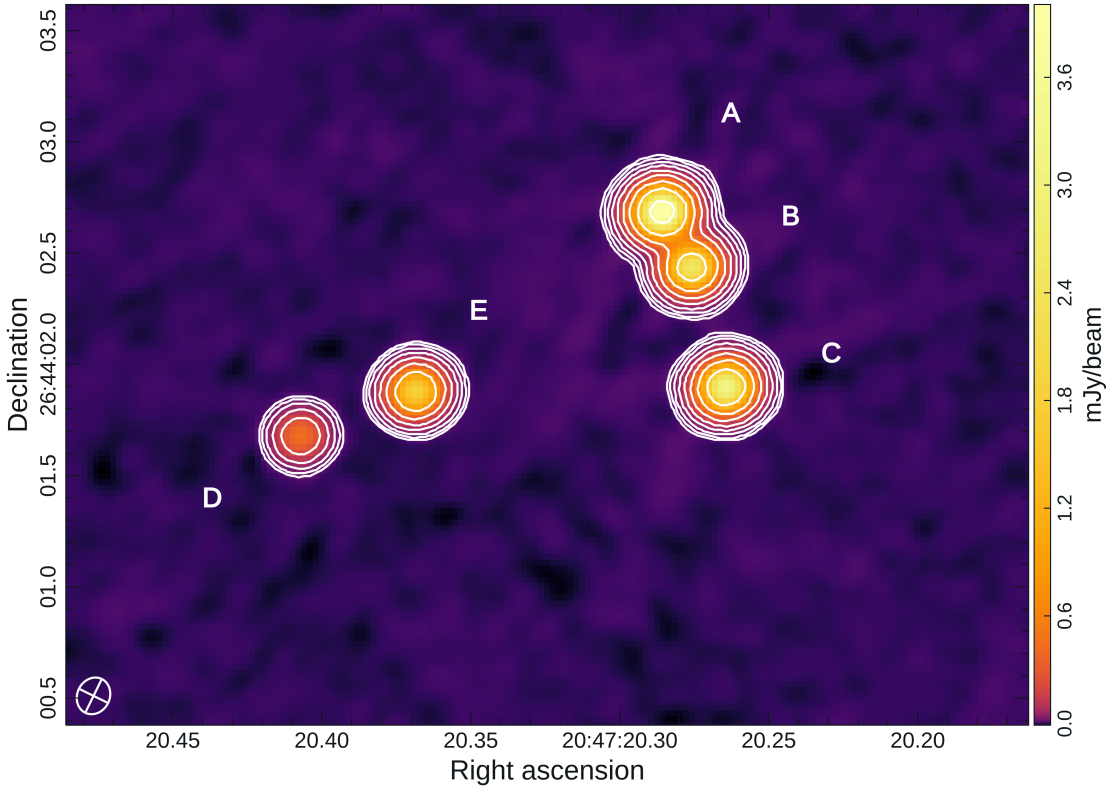

FIGURE 5.1: The stacked Stokes I image of CLASS B2045+265 at a frequency between 12 to 18 GHz, from the VLA observations taken over 20 visits between 2024 March 15 and 2024 May 17 (160 mins total on-source integration). The lensed components are labelled A, B, C and D, with the lensing galaxy labelled as E. Contours are at (5, 10, 20, 40, 80,...)$\times\sigma_{\rm map}$, where $\sigma_{\rm map} = 2.6$ μJy beam^{-1} is the residual image rms. The restoring beam size is 0.169 $\times$ 0.141 arcsec at a position angle of -26.1 deg, and is shown in the bottom left hand corner of the image.

polarisation fraction is

$$P_{\rm frac} = \frac{\sqrt{Q^2 + U^2}}{I}, \tag{5.1}$$

we find $P_{\rm frac} < 0.2\%$. Therefore, we conclude that CLASS B2045+265 is not polarised at frequencies between 12 and 18 GHz, when observed at $\sim$ 0.15 arcsec angular resolution.

5.2 The Radio Spectra of CLASS B2045+265

From Section 2.6, the flux density (S_ν) of each radio component is related to the frequency (ν) via a power law, $S_\nu \propto \nu^\alpha$, where α is the spectral index. Thus, in order to quantify the results from our data, the important information we can parametrise from our many flux-density measurements is the reference flux-density (S_0) and the spectral index for each component on each visit. This is done by fitting, via python polynomial fitting, our data to the power law,

$$S_\nu = S_0 \left(\frac{\nu}{\nu_0}\right)^\alpha, \tag{5.2}$$

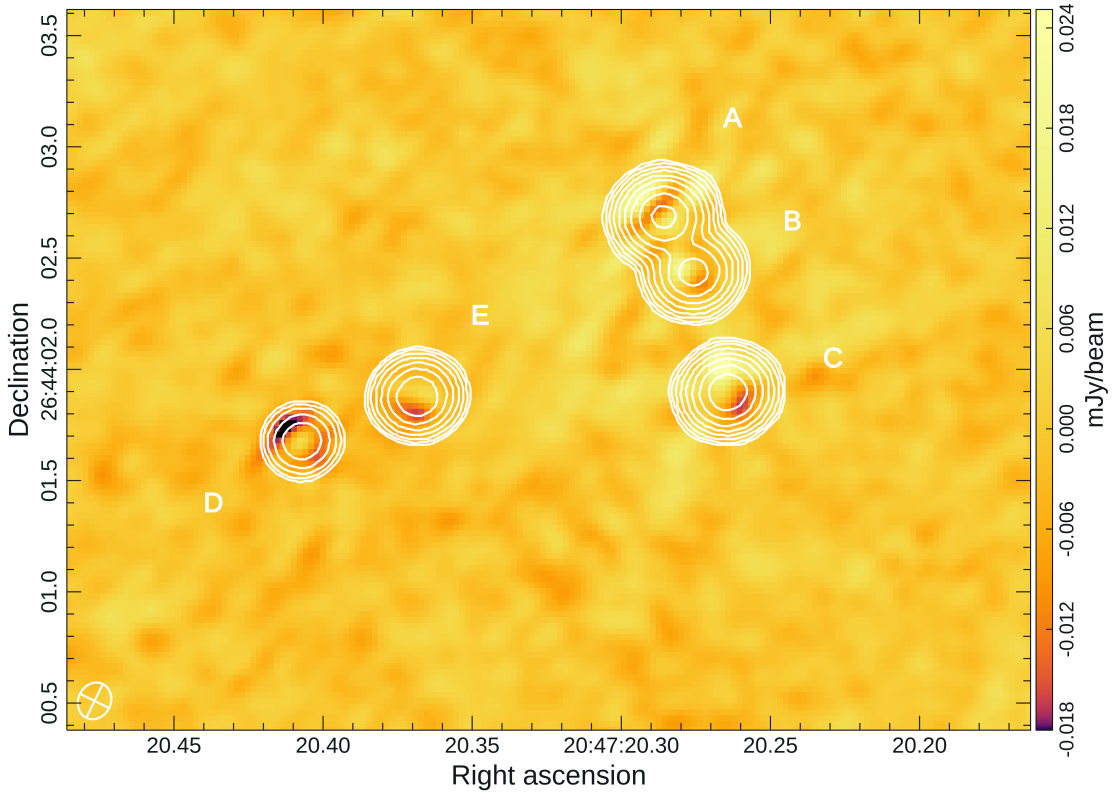

FIGURE 5.2: The stacked Stokes I residual image (model subtracted) of CLASS B2045+265 at a frequency between 12 to 18 GHz, from the VLA observations taken over 20 visits between 2024 March 15 and 2024 May 17 (160 mins total on-source integration). For comparison, the labelling and contours of the Stokes I emission are also shown (see Figure 5.1). There is no evidence of any faint extended emission associated with the lensed images, although low-level residual side-lobe emission from the lensed images remains.

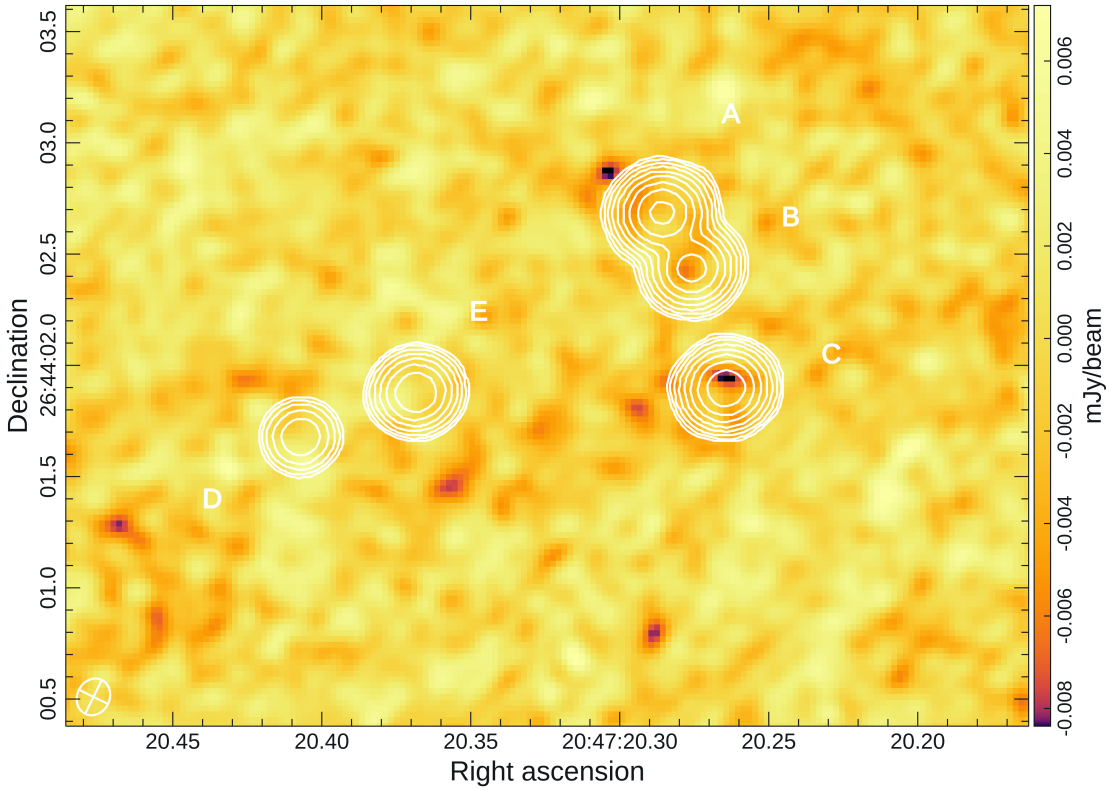

FIGURE 5.3: The stacked Stokes Q image of CLASS B2045+265 at a frequency between 12 to 18 GHz, from the VLA observations taken over 20 visits between 2024 March 15 and 2024 May 17 (160 mins total on-source integration). For comparison, the labelling and contours of the Stokes I emission are also shown (see Figure 5.1). There is no evidence of any Stokes Q emission associated with the lensed images.

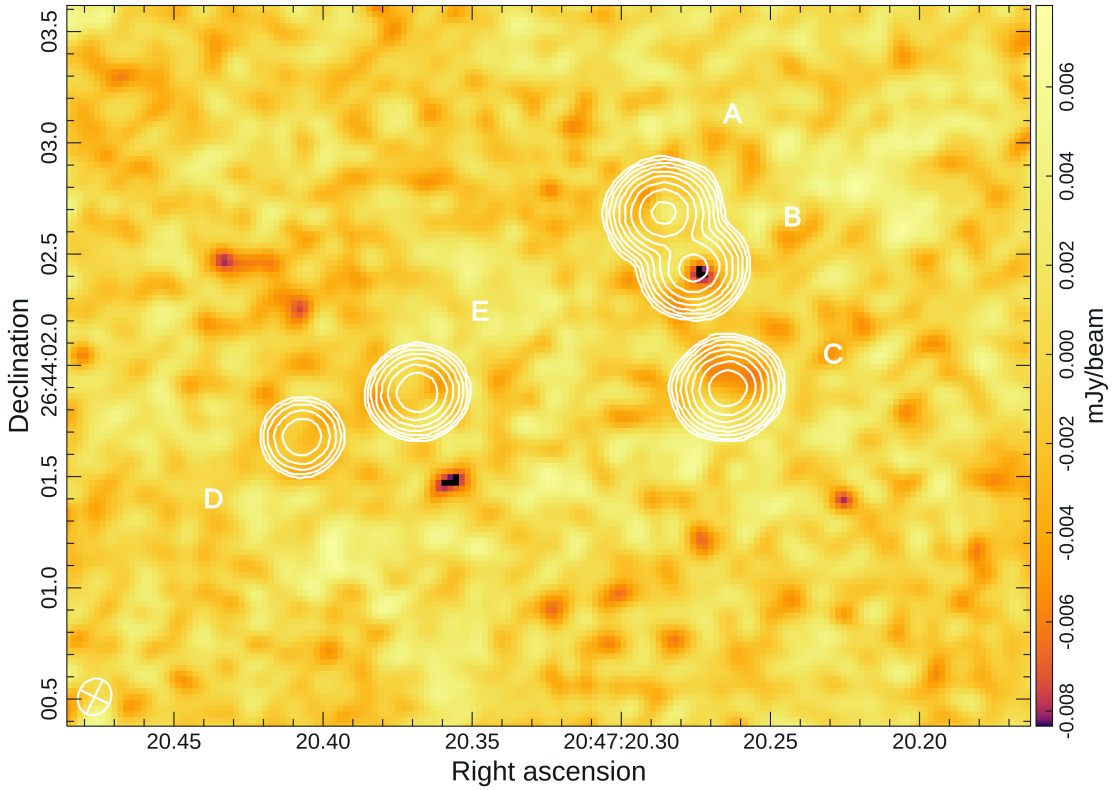

FIGURE 5.4: The stacked Stokes U image of CLASS B2045+265 at a frequency between 12 to 18 GHz, from the VLA observations taken over 20 visits between 2024 March 15 and 2024 May 17 (160 mins total on-source integration). For comparison, the labelling and contours of the Stokes I emission are also shown (see Figure 5.1). There is no evidence of any Stokes U emission associated with the lensed images.

TABLE 5.1: The spectral index between 12 and 18 GHz for lensed images A, B, C and D, and lensing galaxy E taken from the power-law polynomial fits to each individual visit.

Date	A	B	C	D	E
15/03	-0.97 ± 0.01	-1.12 ± 0.02	-1.00 ± 0.02	-0.8 ± 0.2	-0.58 ± 0.04
25/03	-0.95 ± 0.01	-0.94 ± 0.02	-1.00 ± 0.02	-0.8 ± 0.1	-0.22 ± 0.03
30/03	-1.01 ± 0.02	-1.11 ± 0.04	-1.07 ± 0.03	-1.1 ± 0.2	-0.49 ± 0.06
02/04	-0.96 ± 0.01	-1.01 ± 0.02	-0.98 ± 0.02	-0.9 ± 0.1	-0.32 ± 0.03
04/04	-0.91 ± 0.01	-0.94 ± 0.03	-0.96 ± 0.02	-0.9 ± 0.1	-0.40 ± 0.04
07/04	-1.00 ± 0.01	-1.02 ± 0.03	-1.07 ± 0.02	-0.8 ± 0.2	-0.34 ± 0.04
13/04	-0.93 ± 0.01	-0.93 ± 0.02	-0.98 ± 0.02	-1.1 ± 0.1	-0.31 ± 0.03
15/04	-0.85 ± 0.01	-0.85 ± 0.02	-0.87 ± 0.02	-0.7 ± 0.1	-0.37 ± 0.03
18/04	-0.97 ± 0.01	-1.03 ± 0.02	-1.02 ± 0.02	-0.7 ± 0.1	-0.17 ± 0.03
23/04	-1.06 ± 0.01	-1.03 ± 0.03	-1.05 ± 0.03	-1.1 ± 0.1	-0.32 ± 0.03
26/04	-1.02 ± 0.01	-0.98 ± 0.02	-0.96 ± 0.02	-0.8 ± 0.1	-0.24 ± 0.03
28/04	-1.00 ± 0.01	-0.96 ± 0.03	-0.98 ± 0.02	-0.6 ± 0.2	-0.37 ± 0.03
30/04	-0.84 ± 0.01	-0.83 ± 0.02	-0.80 ± 0.02	-1.0 ± 0.1	-0.27 ± 0.03
02/05	-0.91 ± 0.01	-0.90 ± 0.02	-0.88 ± 0.02	-0.7 ± 0.2	-0.15 ± 0.03
05/05	-1.01 ± 0.01	-0.96 ± 0.02	-0.98 ± 0.02	-1.1 ± 0.1	-0.24 ± 0.03
07/05	-0.88 ± 0.01	-0.89 ± 0.02	-0.95 ± 0.02	-0.7 ± 0.1	-0.12 ± 0.04
10/05	-0.96 ± 0.01	-0.89 ± 0.03	-1.00 ± 0.02	-0.7 ± 0.1	-0.60 ± 0.03
12/05	-0.90 ± 0.01	-0.90 ± 0.02	-0.90 ± 0.02	-0.6 ± 0.2	-0.22 ± 0.03
15/05	-0.91 ± 0.01	-0.94 ± 0.02	-0.93 ± 0.02	-0.8 ± 0.1	-0.29 ± 0.03
17/05	-0.90 ± 0.01	-0.87 ± 0.02	-0.90 ± 0.02	-0.7 ± 0.1	-0.31 ± 0.03

where ν_0 is the frequency at which the reference flux density is measured. For our data, we chose the central frequency of 15 GHz as our reference frequency. The python function *polyfit* fits a polynomial to a data set that minimises the squared error, via a least squares fitting, by the order of the polynomial.

In Figure 5.5, we show the flux-density of the lensed images A, B, C and D, and the lensing galaxy E as a function of frequency for each visit. We note that the uncertainties of the flux-densities on 2022 March 30 are particularly large (almost 50 % larger; see also Figure 5.6 for a measure of the quality of the data per channel), and we take this into account in our analysis. Furthermore, in Figure 5.5, we also show the fitted radio spectra to each component, as defined by Equation 5.2. From these fits, we extract the spectral indices and reference flux-densities for each visit, which are presented in Tables 5.1 and 5.2, respectively. Also, we have determined the average spectral index and reference flux-density of each component of the system by combining the data from all visits, which we present in Tables 5.3 and 5.4, respectively.

From Figure 5.5 and Table 5.1, we see that the spectral indices of lensed images A, B and C remain fairly similar over all 20 visits, as we would expect since lensing is achromatic and we are observing the same source multiple times. The spectral indices of lensed image D and the lensing galaxy E are noted to vary more substantially. These variations are believed to come from the lower signal-to-noise ratio of these components. Furthermore, we do see several outliers between each of the lensed images A, B and C per visit, where the difference in spectral index can be up to $\Delta\alpha \sim 0.1$; this is much larger than the relative individual uncertainties on any given visit. In addition, when we compare the average spectral index of each lensed

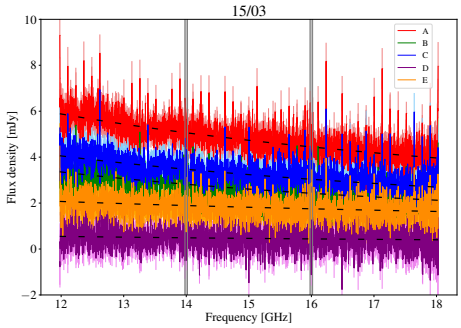

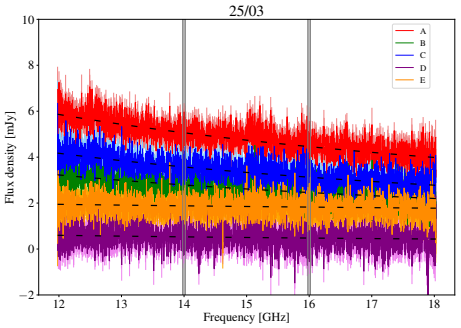

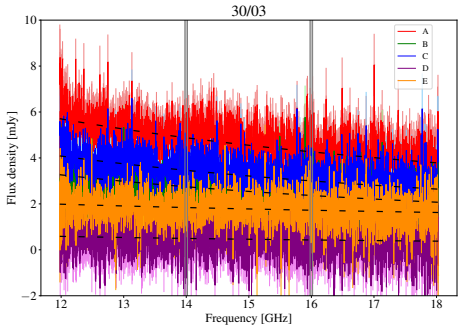

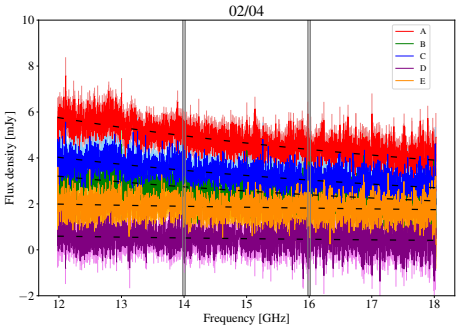

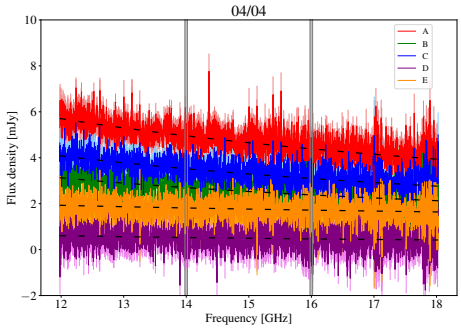

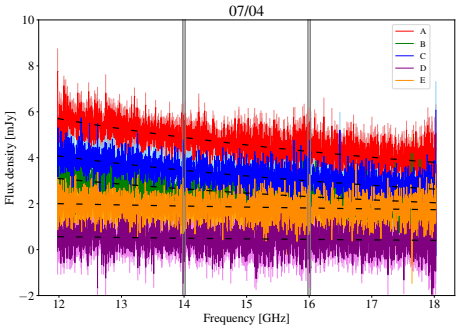

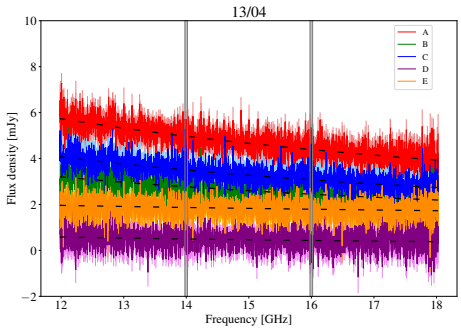

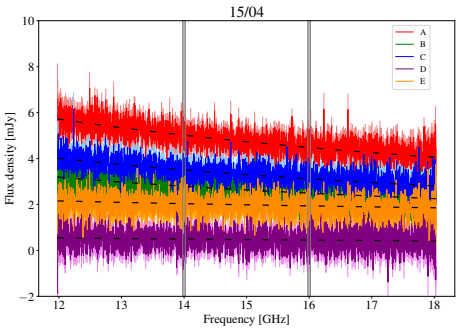

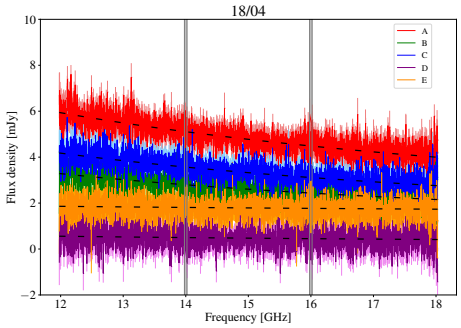

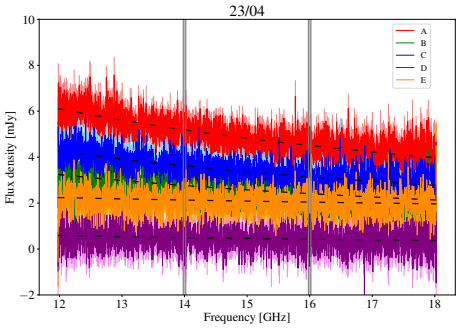

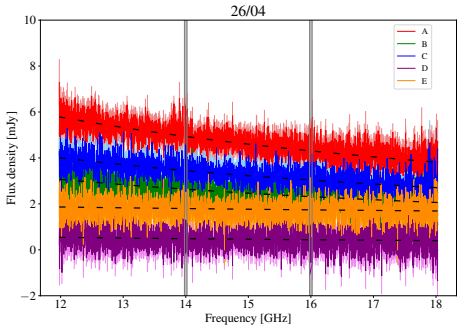

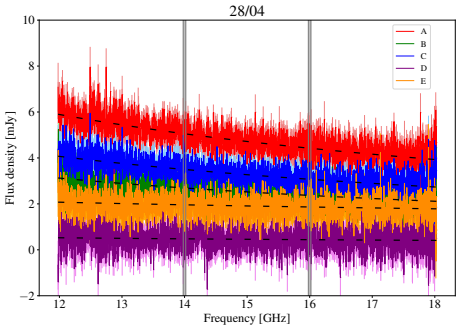

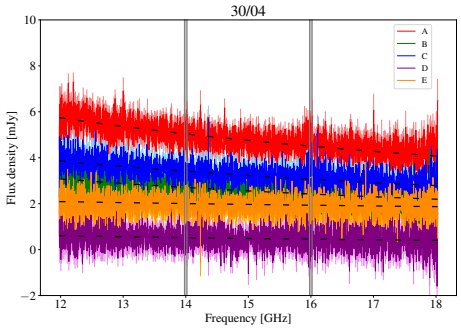

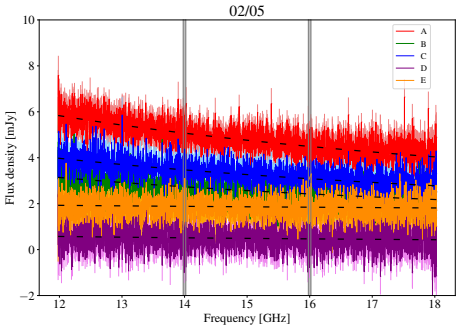

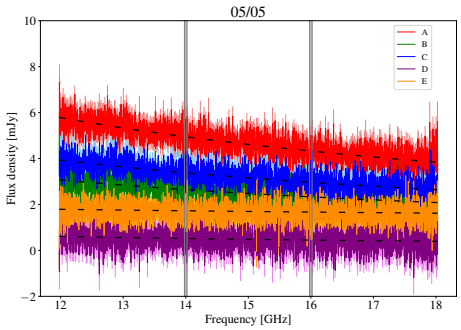

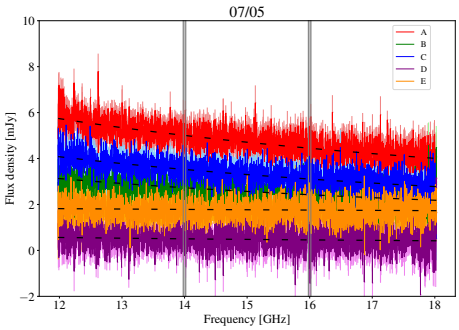

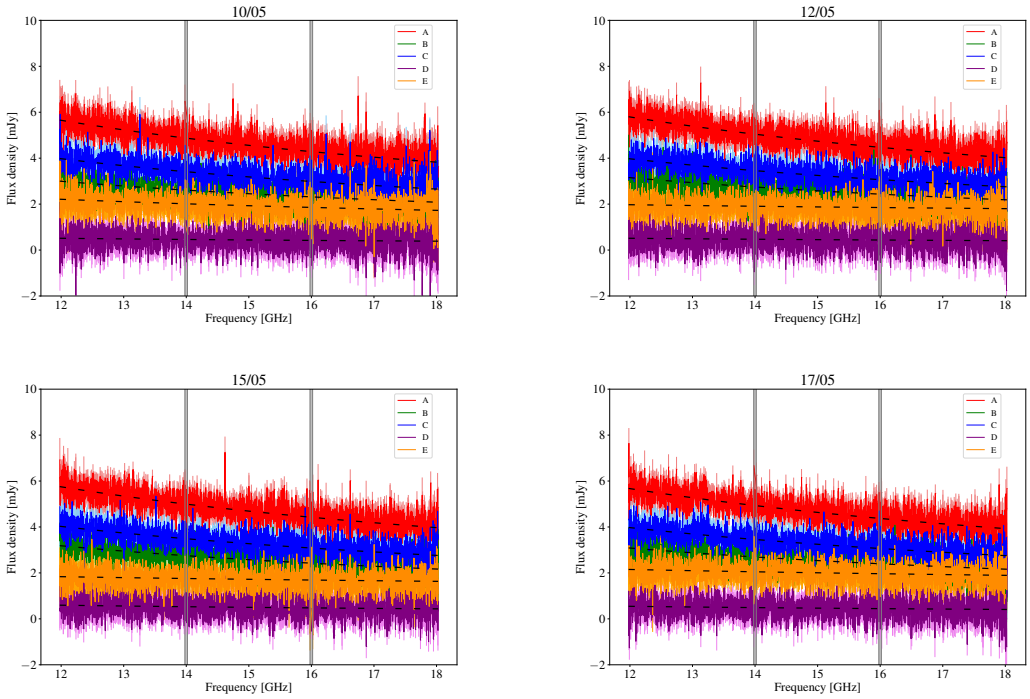

FIGURE 5.5: The radio spectra from all 20 visits between 2022 March 15 and 2022 May 17. In each panel we show the spectra of the four lensed images A, B, C and D, in red, green, blue, and purple, respectively, and the spectra of the lensing galaxy E in orange. The spectra of each component are shown as the flux-density at 2 MHz intervals between 12 and 18 GHz, with the channel rms shown by the lighter shade. The power-law fits are shown as the black dotted lines for each of the spectra. The grey lines represent overlapping baseband channels, which due to the loss in sensitivity have a larger rms (as presented in Figure 5.6).

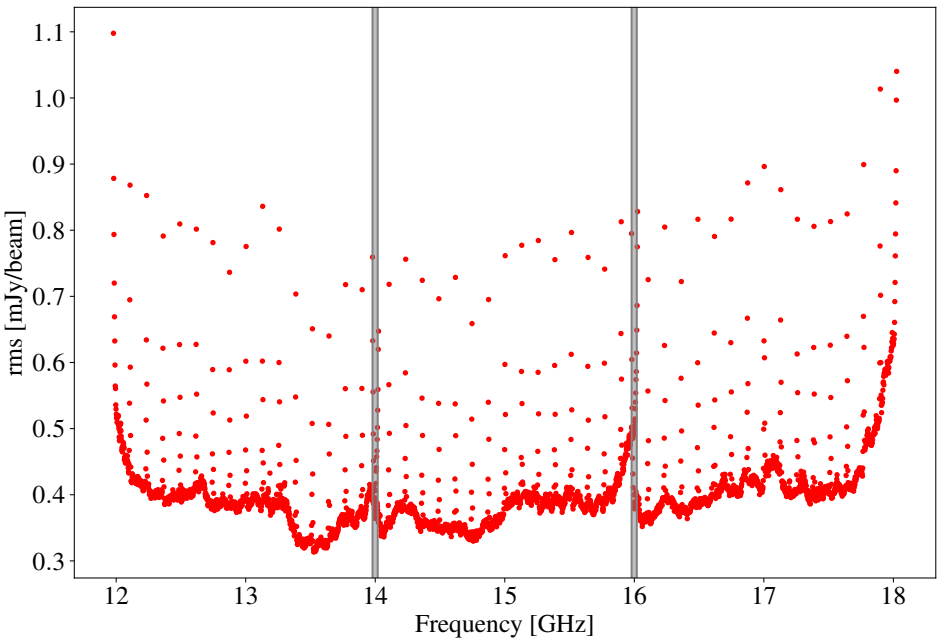

FIGURE 5.6: The average rms per channel over all 20 visits, with overlayed grey lines that represent the overlapping baseband channels. The large increase in the rms is coincident with the edge channels of each spectral window. We also see a loss in sensitivity towards the edges of the full bandwidth.

TABLE 5.2: The flux density at the reference frequency of 15 GHz for the lensed images A, B, C, and D, and lensing galaxy E taken from the power-law polynomial fits to each individual visit. Note that the uncertainties do not include the absolute flux-density scale uncertainty ($\sim$ 5%), which will be important when considering any visit-to-visit comparison.

Date	A (mJy)	B (mJy)	C (mJy)	D (mJy)	E (mJy)
15/03	4.684 ± 0.007	2.594 ± 0.007	3.217 ± 0.007	0.462 ± 0.007	1.818 ± 0.007
25/03	4.738 ± 0.007	2.613 ± 0.007	3.334 ± 0.007	0.501 ± 0.007	1.851 ± 0.007
30/03	4.560 ± 0.010	2.540 ± 0.010	3.210 ± 0.010	0.460 ± 0.010	1.780 ± 0.010
02/04	4.647 ± 0.007	2.558 ± 0.007	3.234 ± 0.007	0.485 ± 0.007	1.853 ± 0.007
04/04	4.654 ± 0.008	2.531 ± 0.008	3.296 ± 0.008	0.494 ± 0.007	1.763 ± 0.008
07/04	4.556 ± 0.008	2.461 ± 0.008	3.205 ± 0.008	0.468 ± 0.008	1.851 ± 0.008
13/04	4.658 ± 0.006	2.598 ± 0.006	3.270 ± 0.006	0.461 ± 0.006	1.829 ± 0.006
15/04	4.732 ± 0.006	2.634 ± 0.006	3.298 ± 0.006	0.470 ± 0.006	1.984 ± 0.006
18/04	4.774 ± 0.007	2.604 ± 0.007	3.332 ± 0.007	0.472 ± 0.007	1.789 ± 0.007
23/04	4.826 ± 0.008	2.580 ± 0.007	3.373 ± 0.007	0.457 ± 0.007	2.085 ± 0.007
26/04	4.598 ± 0.007	2.465 ± 0.007	3.228 ± 0.007	0.459 ± 0.007	1.766 ± 0.007
28/04	4.715 ± 0.007	2.519 ± 0.007	3.269 ± 0.007	0.458 ± 0.007	1.910 ± 0.007
30/04	4.753 ± 0.006	2.554 ± 0.006	3.227 ± 0.006	0.483 ± 0.006	1.967 ± 0.006
02/05	4.761 ± 0.007	2.569 ± 0.007	3.265 ± 0.007	0.489 ± 0.007	1.864 ± 0.007
05/05	4.614 ± 0.007	2.479 ± 0.007	3.159 ± 0.007	0.481 ± 0.007	1.695 ± 0.007
07/05	4.701 ± 0.007	2.566 ± 0.007	3.301 ± 0.007	0.478 ± 0.007	1.769 ± 0.007
10/05	4.558 ± 0.007	2.452 ± 0.007	3.183 ± 0.007	0.438 ± 0.007	1.930 ± 0.007
12/05	4.739 ± 0.007	2.578 ± 0.007	3.248 ± 0.007	0.452 ± 0.007	1.877 ± 0.007
15/05	4.689 ± 0.007	2.576 ± 0.007	3.271 ± 0.007	0.501 ± 0.007	1.721 ± 0.007
17/05	4.633 ± 0.007	2.536 ± 0.007	3.246 ± 0.007	0.465 ± 0.007	2.005 ± 0.007

TABLE 5.3: The spectral index between 12 and 18 GHz for each lensed image (A, B, C and D) and the lensing galaxy (E), taken from the power-law fit to the data averaged over all visits (see Figure 5.7).

A	B	C	D	E
-0.945 ± 0.003	-0.953 ± 0.005	-0.962 ± 0.004	-0.825 ± 0.040	-0.321 ± 0.008

image over all visits (see Figure 5.7) with those obtained during each individual visit, we see that for image A, 65% (13/20 visits) of the individual measurements are not consistent with the average value at the 2σ-level; for image B this is 50% (10/20 visits) and for image C this is 45% (9/20 visits). It is not clear whether this is due to some frequency dependent variability of the background source or a possible calibration error. In the case of the former, the frequency dependent variability would need to be significant since it is happening over very short ($\sim$ days) time-scales. We note that the spectral indices of the lensed images are indicative of non-thermal synchrotron radiation (see Section 2.6), although the spectral indices are much steeper than expected for a flat-spectrum radio source ($\alpha > -0.5$) and for a typical radio source ($\alpha \sim -0.7$). This could be due to the higher energy electrons dissipating their energy faster than at lower energies, and thus, the higher frequency part of the spectrum produces steeper spectral indices (see Section 2.6). Such a steep spectrum radio source is not expected to be variable over such small time-scales. In the case of the latter, a calibration error could manifest as a mis-match between the measured spectrum of the phase-reference calibrator and its true spectrum (which is used to define the spectrum of our target on any given day). This will be investigated further once all of the lensed objects from LoFT have been analysed, since it should be a systematic effect that is seen for all targets.

Also from Figure 5.5 and Table 5.2, we see the variation in the flux-density of each component at the reference frequency. From Equation 5.2, S_0 is essentially a normalization of the spectrum, and thus, can be used as an estimate of the level of variability for each lensed image (and for the emission from the lensing galaxy). However, from Table 5.2, we see that the visit-to-visit variations in the flux-density of each lensed image are significant, relative to the measurement uncertainty on each day, and compared to the average flux-density for each component presented in Table 5.4 and shown in Figure 5.7. As for the spectral indices above, this could be due to either source variability or an unaccounted for systematic in the measurement of the flux-densities. What we observe is almost certainty related to the latter, since the day-to-day absolute flux-density calibration of the VLA is around a few per cent, when done correctly (we will assume a conservative 5%). We find that the systematic uncertainty in the average flux density of the lensed images A, B, C, and D should be (systematic) 0.23, 0.13, 0.16 and 0.02 mJy, respectively. In the case of lensed images A, B and C, these systematic uncertainties are significantly larger than the statistical uncertainties given in Tables 5.2 and 5.4. When we take this systematic uncertainty into account, there is no evidence of variability in the lensed images A, B and C over our observing period.

5.3 Flux Ratios

Figure 5.8 shows the flux ratios of the lensed images as a function of frequency for each visit. These have been produced by dividing the channel data for lensed images B, C and D by those of lensed image A; as component E is known to be associated

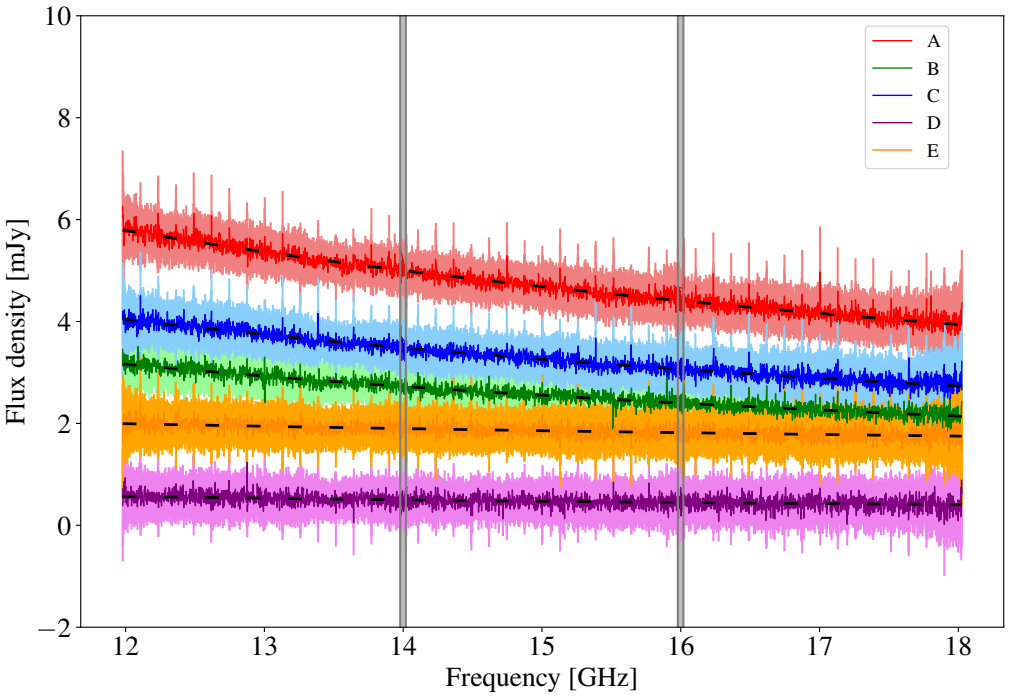

FIGURE 5.7: The average radio spectra from all 20 visits combined, showing the four lensed images A, B, C and D, in red, green, blue, and purple, respectively, and the lensing galaxy E in orange. The spectrum of each component is shown as the flux-density at 2 MHz intervals between 12 and 18 GHz, with the channel rms shown by the lighter shade. The power-law fits are shown as the black dotted lines for each spectrum. The grey lines represent overlapping baseband channels, which due to the loss in sensitivity have a larger rms (as presented in Figure 5.6).

TABLE 5.4: The flux density at the reference frequency of 15 GHz for each lensed image (A, B, C and D) and the lensing galaxy (E), taken from the power-law fit to the data averaged over all visits (see Figure 5.7).

A (mJy)	B (mJy)	C (mJy)	D (mJy)	E (mJy)
4.684 ± 0.002	2.552 ± 0.002	3.260 ± 0.004	0.472 ± 0.002	1.856 ± 0.002

with the foreground lensing galaxy, it will not be subject to a flux-ratio analysis. In principle, taking the flux ratios should allow us to divide out any frequency-dependent gain errors remaining in our data after the calibration process, since these would contribute equally to each image. The ratio-spectra presented in Figure 5.8 have been fitted with a linear polynomial, in python, and the flux-ratios determined from these fits to each visit are presented in Table 5.5.

From Figure 5.8, we see that the flux ratios of the lensed images remain fairly constant over 12 to 18 GHz, which suggests that there is no strong variation of the flux-ratios as a function of frequency. This is expected for gravitational lensing as the phenomenon is achromatic. We also see that the ratios of lensed images C/A is the highest, followed by the ratios of B/A and D/A. This is consistent with the results from previous monitoring at, for example, 5 GHz by Koopmans et al. (2003). From looking at the individual ratios given in Table 5.5 for each visit, we see that there is some evidence of a variation in the flux-ratios from visit-to-visit. For example, in the case of the flux-ratio of lensed images B and C with respect to lensed image A, we see that the maximum change in the ratio over the 20 visits is of order 6%. In the case of the flux ratio of lensed image D with respect to lensed image A, this variation is closer to 12%. These visit-to-visit variations are much larger than the uncertainty of the flux-ratios on any given visit. This is also demonstrated in Figure 5.9, where we show the flux ratios of lensed images B, C and D with respect to lensed image A over the 63 days of our monitoring campaign. Here, the variability is not immediately apparent since the flux ratios appear globally flat as a function of time. However, by normalising the flux ratios by their average value, as is presented in Figure 5.10, we see that there is clear time-dependent variations in the flux-ratios of each lensed image with respect to lensed image A. The variance on the flux-ratios has been quantified using,

$$\sigma = \sqrt{\frac{\sum(R_i - \text{mean})^2}{N \times \text{mean}}}, \tag{5.3}$$

where R_i is the flux-ratio for each visit i, and N is the total number of visits. From this, we find that the flux ratios have an rms scatter of 1.6%, 1.4% and 3.5 % for B/A, C/A and D/A, respectively.

In Figure 5.11, we have averaged our flux ratios over time and by again conducting a linear polynomial fit to the data we obtain the flux ratios as seen in Table 5.6; these are our best estimates of the true flux ratios of CLASS B2045+265. We confirm that these flux ratios are extreme for a cusp-like lens systems. However, since the lensed source is not exactly at the cusp, it is more appropriate to compare with the expectations for the best macro-model for this system. Here, we use the predicted values for the flux ratios of CLASS B2045+265, based on a power-law mass model, with an external shear component (Jacob Cohen; private communication). These model-predicted flux-ratios are B/A = 1.445 ± 0.020, C/A = 0.504 ± 0.018, and D/A = 0.012 ± 0.004. These values are in strong contention to those presented in Table 5.6, and it is here we see the nature of the extreme flux-ratio anomaly present in CLASS B2045+265.

5.4 R_{cusp} of B2045+265

The R_{cusp} parameter, as defined by Equation 3.6, gives further insight to the extreme nature of the flux-ratio anomaly of CLASS B2045+265. Using the measured

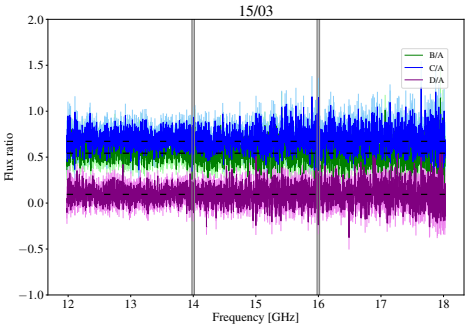

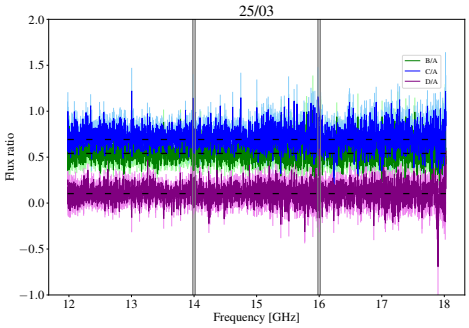

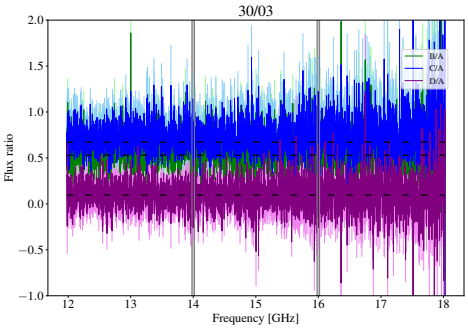

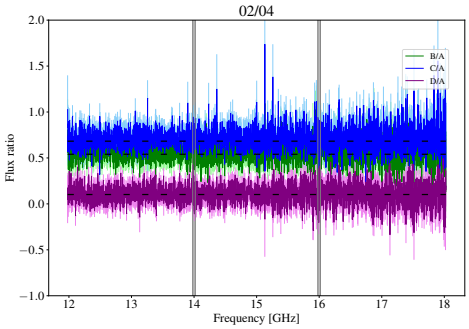

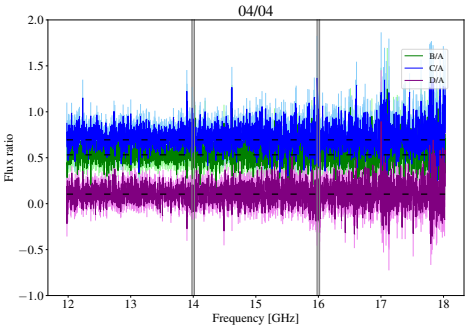

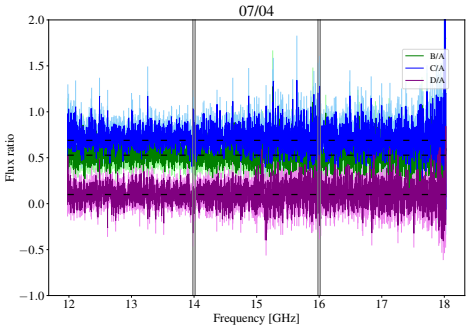

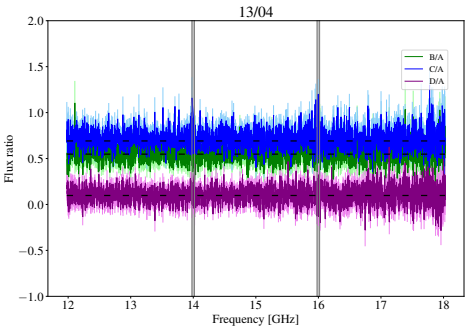

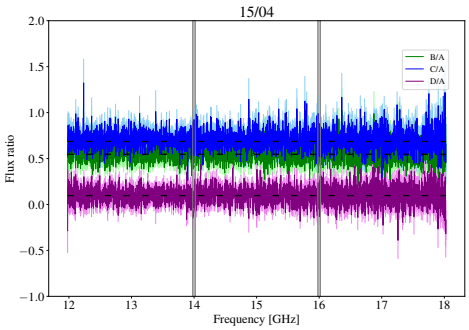

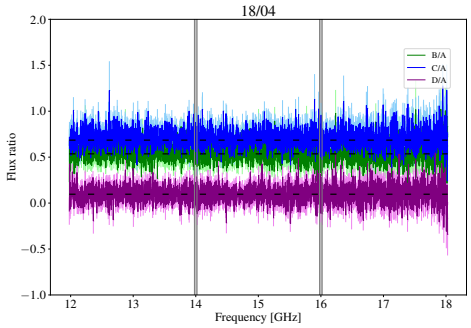

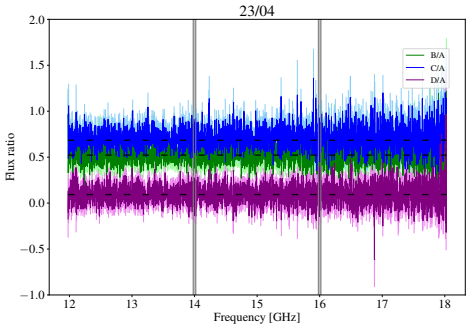

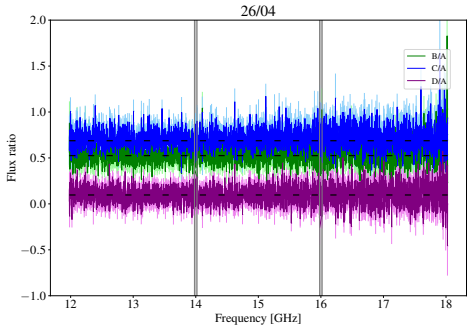

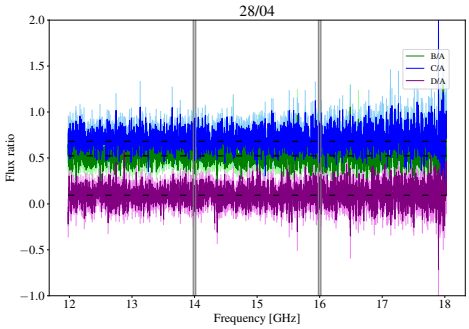

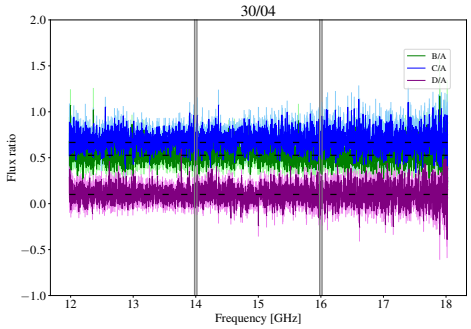

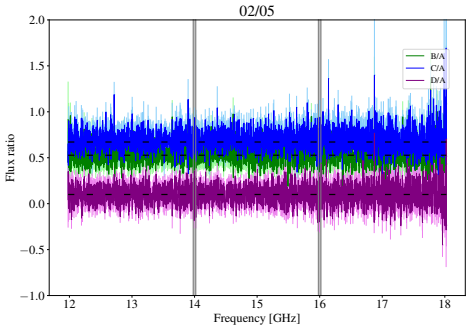

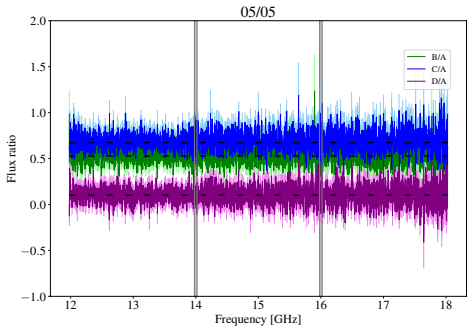

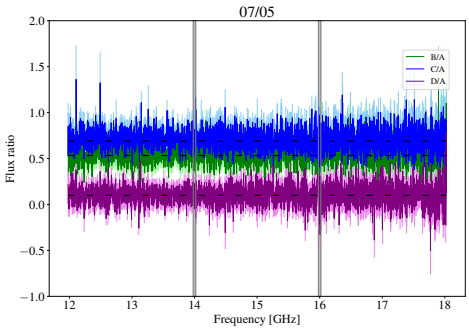

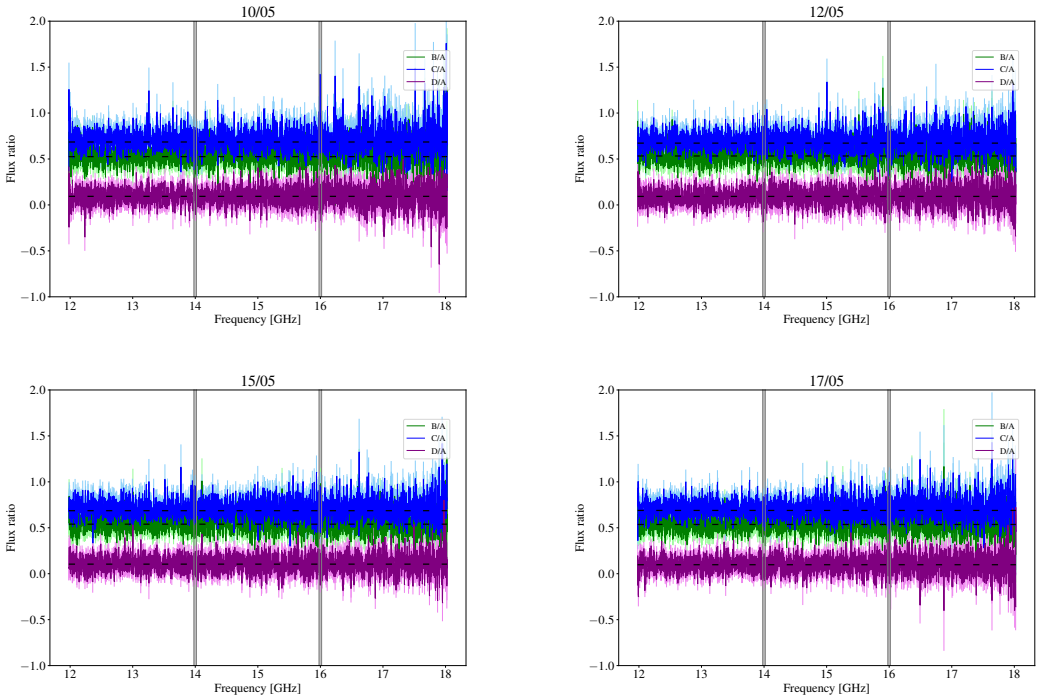

FIGURE 5.8: The flux-ratio of the lensed images as a function of frequency for all 20 visits between 2022 March 15 and 2022 May 17. In each panel, we show the flux-ratio of lensed images B, C and D, with respect to image A, in green, blue and purple, respectively. The flux-ratios of each lensed image are shown at 2 MHz intervals between 12 and 18 GHz, with the channel rms shown by the lighter shade. The linear-fits of a first order polynomial are shown as the black dotted lines for each flux-ratio. The grey lines represent overlapping baseband channels, which due to the loss in sensitivity have a larger rms (as presented in Figure 5.6).

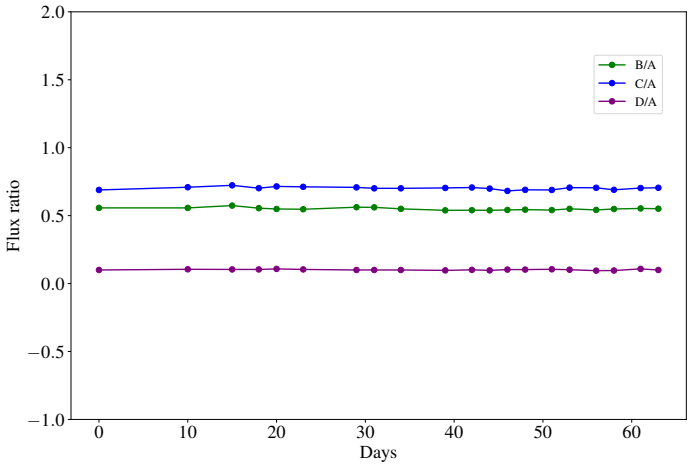

FIGURE 5.9: The flux ratios of lensed images B, C and D, with respect to image A, as a function of time. The flux-ratios at each visit are obtained via a least squares fit to the flux-ratio spectrum obtained between 2022 March 15 (day 0) and 2022 May 17 (day 63), as presented in Figure 5.8.

TABLE 5.5: The flux-ratios between 12 and 18 GHz for lensed images B, C and D with respect to image A, taken from the power-law polynomial fits to each individual visit.

Date	B/A	C/A	D/A
15/03	0.557 ± 0.002	0.689 ± 0.002	0.100 ± 0.002
25/03	0.557 ± 0.002	0.709 ± 0.002	0.105 ± 0.002
30/03	0.574 ± 0.003	0.723 ± 0.003	0.104 ± 0.003
02/04	0.555 ± 0.002	0.702 ± 0.002	0.104 ± 0.002
04/04	0.549 ± 0.002	0.715 ± 0.002	0.108 ± 0.002
07/04	0.547 ± 0.002	0.712 ± 0.002	0.104 ± 0.002
13/04	0.562 ± 0.002	0.708 ± 0.002	0.100 ± 0.002
15/04	0.561 ± 0.002	0.701 ± 0.002	0.100 ± 0.002
18/04	0.550 ± 0.002	0.701 ± 0.002	0.100 ± 0.002
23/04	0.539 ± 0.002	0.704 ± 0.002	0.097 ± 0.002
26/04	0.540 ± 0.002	0.707 ± 0.002	0.101 ± 0.002
28/04	0.539 ± 0.002	0.699 ± 0.002	0.097 ± 0.002
30/04	0.542 ± 0.002	0.682 ± 0.002	0.103 ± 0.002
02/05	0.544 ± 0.002	0.690 ± 0.002	0.103 ± 0.002
05/05	0.541 ± 0.002	0.689 ± 0.002	0.105 ± 0.002
07/05	0.550 ± 0.002	0.706 ± 0.002	0.102 ± 0.002
10/05	0.542 ± 0.002	0.705 ± 0.002	0.095 ± 0.002
12/05	0.549 ± 0.002	0.690 ± 0.002	0.096 ± 0.002
15/05	0.553 ± 0.002	0.703 ± 0.002	0.108 ± 0.002
17/05	0.551 ± 0.002	0.705 ± 0.002	0.100 ± 0.002

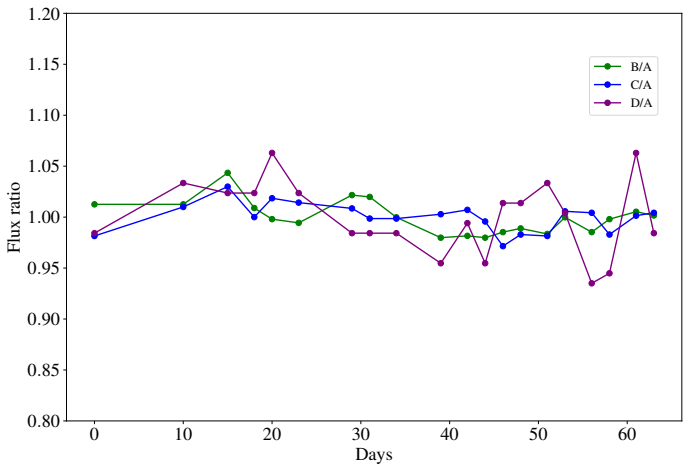

FIGURE 5.10: The normalised flux-ratio for lensed images B, C and D with respect to lensed image A. The flux-ratios at each visit are from a least squares fit to the flux-ratio spectrum obtained with the VLA between 2022 March 15 (day 0) and 2022 May 17 (day 63). The rms of the normalised flux-ratios are 1.6%, 1.4% and 3.5% for B/A, C/A and D/A, respectively.

TABLE 5.6: The average flux ratios between 12 and 18 GHz for lensed images B, C, and D with respect to lensed image A, as determined from the linear fit to the data taken over all visits (see Figure 5.11).

B/A	C/A	D/A
0.5444 ± 0.0004	0.6957 ± 0.0004	0.1002 ± 0.0004

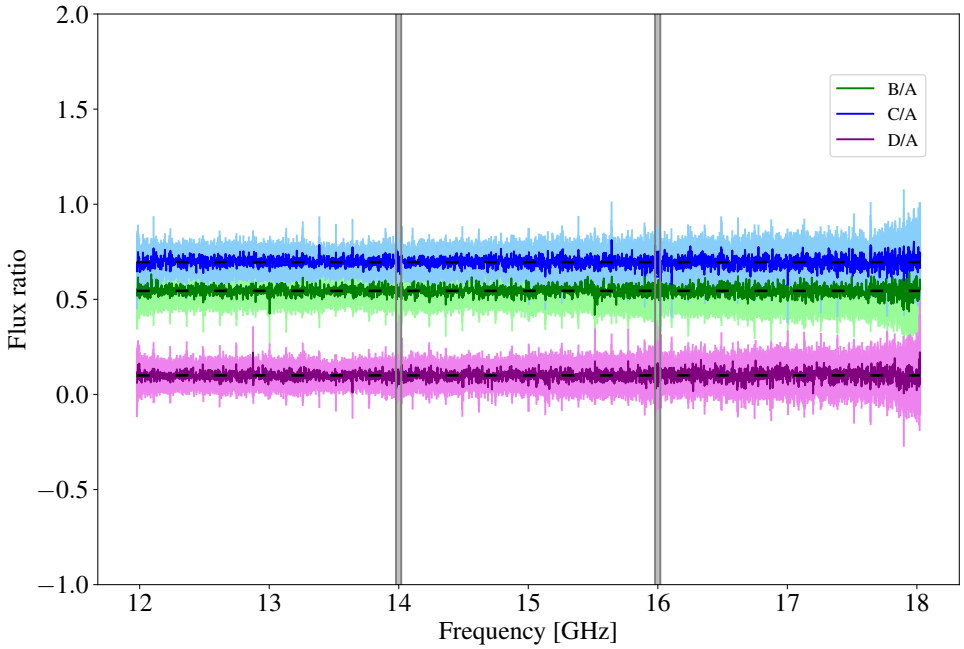

FIGURE 5.11: The flux-ratio spectrum of the lensed images B, C and D, with respect to lensed image A with associated uncertainties averaged over time. The grey lines represent overlapping channels that have a larger uncertainty, as seen in Figure 5.6.

TABLE 5.7: The R_{cusp} value for each visit, calculated using the flux-density of each lensed image at the reference frequency of 15 GHz, as given in Table 5.2.

Date	R_{cusp}
15/03	0.506 ± 0.001
25/03	0.511 ± 0.001
30/03	0.506 ± 0.002
02/04	0.510 ± 0.001
04/04	0.517 ± 0.001
07/04	0.518 ± 0.001
13/04	0.506 ± 0.001
15/04	0.506 ± 0.001
18/04	0.513 ± 0.001
23/04	0.521 ± 0.001
26/04	0.520 ± 0.001
28/04	0.520 ± 0.001
30/04	0.515 ± 0.001
02/05	0.515 ± 0.001
05/05	0.516 ± 0.001
07/05	0.515 ± 0.001
10/05	0.519 ± 0.001
12/05	0.512 ± 0.001
15/05	0.511 ± 0.001
17/05	0.513 ± 0.001

flux-densities presented in Table 5.2, along with the equation for the magnification (Equation 2.59), we have calculated the R_{cusp} parameter for each visit, which are presented in Table 5.7. In Figure 5.12, we visualize our calculated values for R_{cusp} as a function of time. We see that there is evidence of a variation in the R_{cusp} parameter, with an rms scatter of 0.97% over the 63 day period of our monitoring campaign. This is consistent with the variation seen in the flux-density of each lensed image at the reference frequency, as is to be expected.

Furthermore, we find an average value of $R_{cusp} = 0.5137 \pm 0.0003$, when the average flux-densities for each lensed image at the reference frequency are used (see Table 5.4). From Equation 3.1, we would expect the value of the R_{cusp} parameter for a true cusp-like lens system to tend towards 0. However, this is in strong disagreement with our findings, which confirm that CLASS B2045+265 has the largest value of R_{cusp} for any gravitational lens system known to date. CLASS B2045+265 is thus an extreme case of a flux-ratio anomaly and is thus an important case study into the nature of these anomalies. We note that our obtained value of R_{cusp} is consistent with the value determined by Koopmans et al. (2003), who found $R_{cusp} = 0.501 \pm 0.035$ at 5 GHz.

5.5 Complex Mass Distributions and Dark Matter

We have now determined the most precise measurement of the flux-ratios and R_{cusp} parameter for CLASS B0245+265 to-date, taking into account whether there is any significant frequency- and/or time-dependent effects. Although we find no strong evidence for any frequency dependence, there is some low level time dependence,

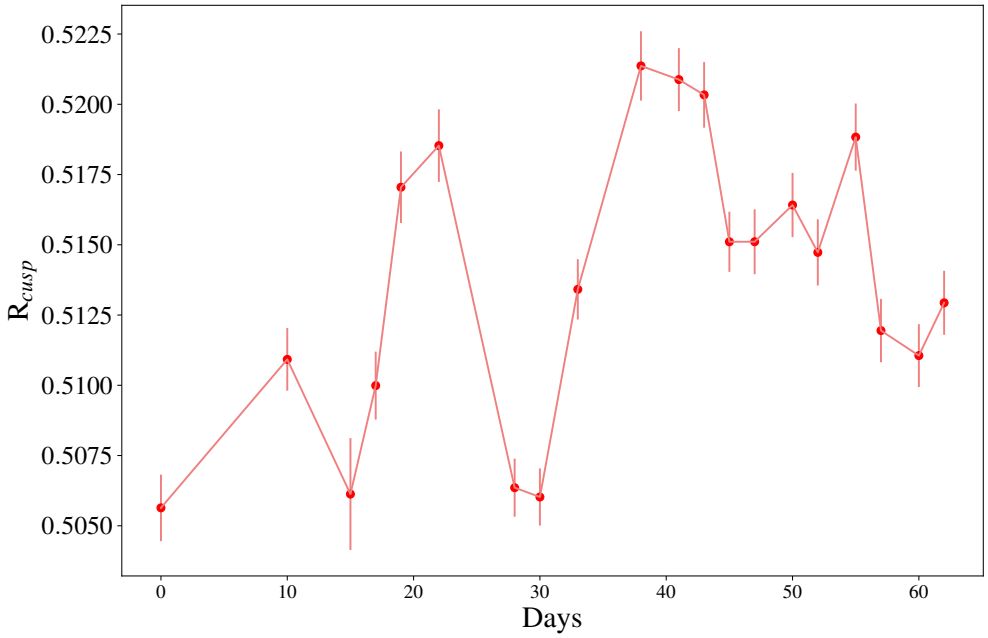

FIGURE 5.12: The R_{cusp} parameter for each visit between 2022 March 15 (day 0) and 2022 May 17 (day 63). There is an rms scatter of 0.97% in the R_{cusp} value between day 0 and 63.

which is likely due to systematic uncertainties in the calibration process. However, we note that this may also be due to some low-level variability in the lensed source. Nevertheless, for the remainder of our analysis, we will assume that the derived flux ratios and their uncertainties are representative of the observed properties of the system. With these values in hand, we now investigate what the flux ratios can tell us about the nature of dark matter.

In collaboration with Dr. Jacob Cohen (UC Davis), and by providing him with the relevant information on the image positions and flux-ratios for CLASS B2045+265, we have produced Markov-Chain Monte Carlo (MCMC) fits (Cohen et al., 2024) for an elliptical power-law mass model with an external shear (similar to an SIE), and with 3rd and 4th order multipole expansions of the mass distribution. In Figures 5.13 and 5.14, we show the fits for the elliptical power-law and multipole mass distributions, respectively, along with their predicted flux-ratios.

Cohen et al. (2024) postulate that more complex mass distributions than that of an elliptical power-law (plus and external shear; such as an SIE) could account for the anomalous flux ratios in gravitational lens systems. This idea has already been considered for CLASS B2045+265 by Congdon and Keeton (2005), where mass distributions of multipoles with an external shear were applied to several lens systems. This multipole fitting procedure is seen as a possible alternative to small-scale milli-lensing by sub-haloes since more complex structure my result in an uneven mass distribution, allowing for the observed flux ratios to vary from what we would expect. However, Cohen et al. (2024) found that low-order multipole fits are unable to reproduce the physical structures that would be viable mass distributions. On the other hand, higher order multipole fits are able to account for the flux ratio anomalies in some systems; in the case of CLASS B2045+265, the flux ratio anomalies are

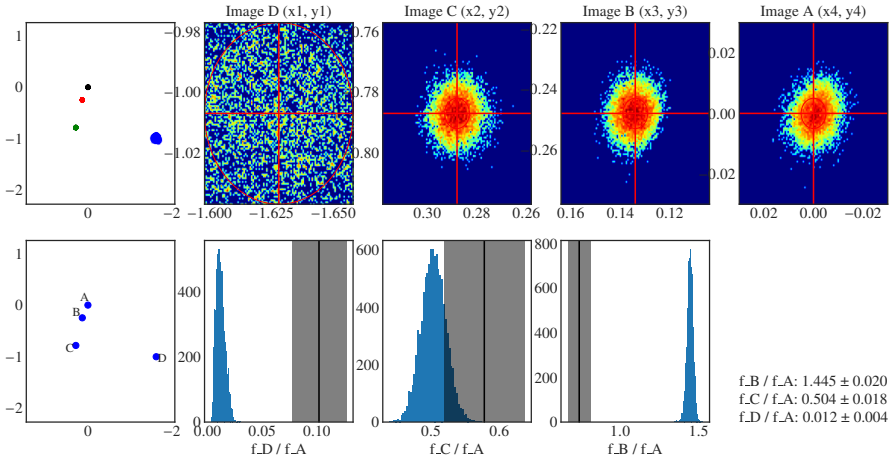

FIGURE 5.13: The model-predicted flux ratios and image positions for for an elliptical power-law distribution. These predictions are derived from an MCMC fitting for 10^4 iterations. The three panels on the bottom right show the predicted flux ratios for all 10^4 iterations, along with a back vertical line that represents the observed flux ratios found by this project. The associated uncertainty is represented as the grey shaded area. The flux-ratios B/A, C/A, and D/A are predicted to be 1.445 ± 0.020, 0.504 ± 0.018 and 0.012 ± 0.004, respectively, for this mass model.

so extreme that they have yet to be replicated through these mass models. As seen in Figures 5.13 and 5.14, these complex mass models alone are not able to reproduce our observed flux ratios from Table 5.6, and thus, for the next step in our investigation, we constrain the mass fraction in sub-haloes.

Using Bayesian inference to produce a probability density function (PDF), we are able to constrain the mass fraction in sub-haloes (f_{sub}) and construct a similar distribution to that made by Hsueh et al., 2019, as presented in Figure 1.1. This Bayesian inference was done in collaboration with Dr. Jacob Cohen (UC Davis) and Dr. Simona Vegetti (MPA). Our analysis was done by running 32 000 realizations for multiple f_{sub} values between 0.00055 (0.055%) and 0.05623 (5.623%) for a sub-halo mass-function that was consistent with CDM. Each of these realizations produced a simulated model of CLASS B2045+265 with varying f_{sub} values (0.00055, 0.001, 0.00178, 0.00316, 0.00562, 0.01, 0.01778, 0.03168 and 0.05623). For each value of f_{sub}, a likelihood calculation was conducted by comparing the realization model values of the image positions to the observed image positions found from VLBA data of CLASS B2045+265 at 5 GHz (McKean et al., 2007), as our image positions are fixed during our analysis, and by fixing the flux ratios to those we derived above. This was done in the form of taking the natural logarithm of the χ^2 of the simulated data compared to our calculated data for flux ratios and positions, such that,

$$\ln(\text{likelihoods}) = -0.5 \left(\frac{\text{model} - \text{observed}}{\sigma_{\text{obs}}} \right)^2 . \tag{5.4}$$

Here, the total likelihood, in log space, is the summation of each of these $\ln(\text{likelihoods})$ and subtracting the log value of the number of realizations per f_{sub} value (32 000 realizations). From this, we were able to produce twenty PDFs (one for each visit). We

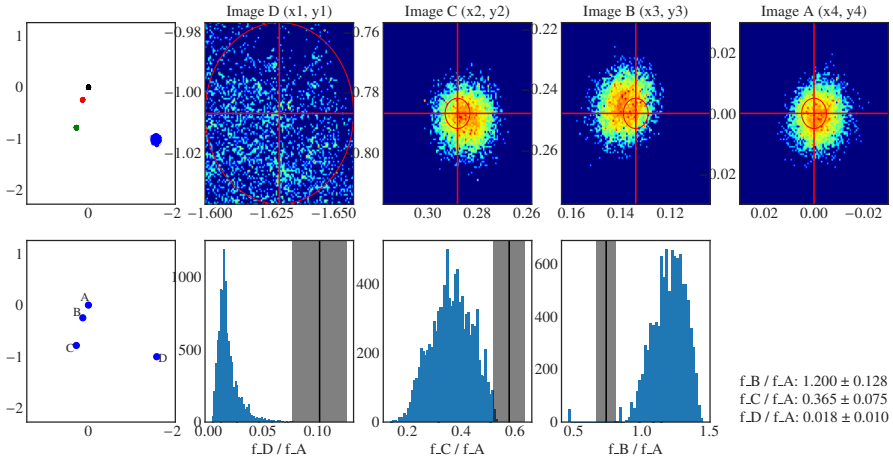

FIGURE 5.14: The model-predicted flux ratios and image positions for for an elliptical power-law distribution with 3rd and 4th-order multipoles. These predictions are derived from an MCMC fitting for 10^4 iterations. The three panels on the bottom right show the predicted flux ratios for all 10^4 iterations, along with a back vertical line that represents the observed flux ratios found by this project. The associated uncertainty is represented as the grey shaded area. The flux-ratios B/A, C/A, D/A are predicted to be 1.200 ± 0.128, 0.365 ± 0.075 and 0.018 ± 0.010, respectively, for this mass model.

then fitted a smoothed curve to the likelihood for each value of f_{sub} (see Figure 5.15). Here, it is important to note that at $f_{sub} = 0.0562$ none of the 32 000 realizations were able to reproduce the images of CLASS B2045+265, and thus, data for $f_{sub} > 0.0562$ were excluded. In Figure 5.16, these values have been averaged together to form a mean PDF for f_{sub}.

We see that the resulting PDF has a non-normal distribution. Also, the current simulation models at $f_{sub} = 0.0562$ and higher (with the PDF seeming to continue increasing at $\sim 3\%$) are not able to reproduce the image properties of CLASS B2045+265. Therefore, we are unable to constrain f_{sub} from our data. We are however able to extrapolate that the value of f_{sub} must be larger than the upper limit for CDM, as predicted by numerical simulations (Xu et al., 2015). Here, we note that we have been considering an idealized CDM model and have not accounted for any line-of-sight sub-haloes outside of the bounds of the lens galaxy halo. This would lower the expected value of f_{sub} since some of the mass (up to two-thirds) can be accounted for in line-of-sight sub-haloes (Despali et al., 2018).

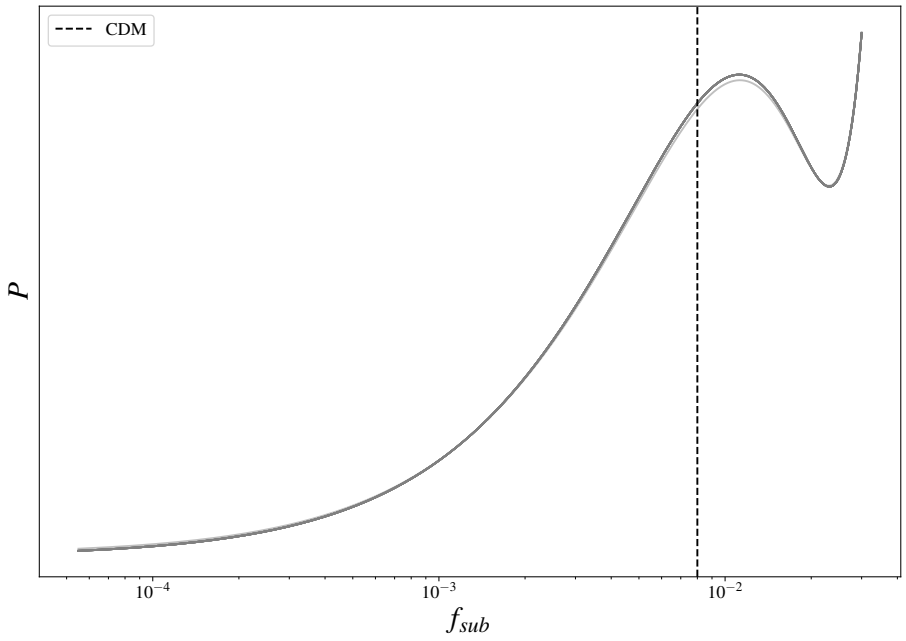

FIGURE 5.15: The probability density function for f_{sub} for all 20 visits of CLASS B2045+265. The vertical black line, similarly to Figure 1.1, shows the upper limit for CDM, as derived by Xu et al. (2015) from numerical simulations ($f_{sub} = 0.008$).

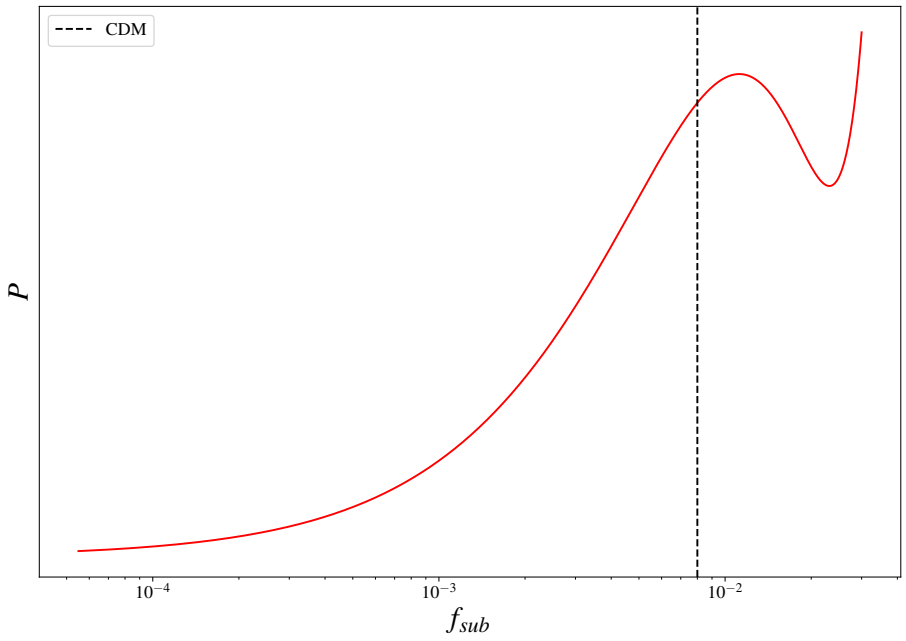

FIGURE 5.16: The mean probability density function for f_{sub}. The vertical black line, similarly to Figure 1.1, shows the upper limit for CDM, as derived by Xu et al. (2015) from numerical simulations ($f_{sub} = 0.008$).

Chapter 6

Discussion

In the previous chapter, we presented the results from our data analysis of the CLASS B2045+265 multi-frequency monitoring observations with the VLA. Here, we will be taking a deeper look into the significance of these results and what they tell us about the nature of the flux-ratio anomaly for our target system. Thus, we will discuss what the radio spectra of CLASS B2045+265 tell us about propagation effects along the line-of-sight to the lensed radio source, and what possible causes and implications there are for the low-level variability seen. This chapter will also review whether a complex macro-model and/or dark matter sub-haloes are the cause of the flux-ratio anomaly seen for CLASS B2045+265.

6.1 Absorption from Propagation Effects

From Figures 5.7 and 5.11, we are able to assess the nature of the flux-ratio anomaly in our system as it pertains to frequency. We see the combined spectra and how they change over the frequency range 12 to 18 GHz. This frequency range was specifically chosen in order to mitigate, or at least alleviate, any frequency dependent absorption/scattering effects. At these relatively high radio frequencies, effects from molecular absorption are expected to be negligible since there are no major transitions (redshifted to the lensing galaxy frame), except for high excitation hydroxyl (OH; rest-frame 23.8053069 and 32.8435288 GHz). However, from Figures 5.7 and 5.11, no discrete absorption affects are seen in our data, and thus, we can exclude molecular absorption as a possible cause of the flux-ratio anomaly seen in previous narrow-band imaging at 15 GHz (Fassnacht et al., 1999). We note that the observations of Koopmans et al. (2003) at 5 GHz with MERLIN found evidence for extrinsic variability (see below), which suggested that there may be interstellar scattering by a molecular cloud along the line-of-sight to the lensed images. Even though we do not see any evidence of absorption in our frequency range, broad-band observations at lower frequencies may detect lower excitation OH from the possible molecular cloud associated with this system.

Another form of absorption prevalent with sources of synchrotron emission is that of free-free absorption. Similarly to that of free-free emission, free-free absorption is a result of the interaction between free particles that remain free after the interaction. However, in this interaction, a photon would be absorbed rather than emitted from a free electron. This differs from absorption by molecules; as mentioned previously, such an absorption from molecules would be at a discrete frequency whereas free-free absorption is continuous, and thus, can change the flux-density over a wide frequency range. For example, this can be seen in Figure 2.5 as the turn-over in the spectra when $\tau > 1$. Free-free absorption will be caused when the radio waves pass through an ionised medium along the line-of-sight, which results in a modification

to the observed spectrum, such that,

$$S_\nu = S_{\nu_0}(\nu/\nu_0)^\alpha \exp[-\tau(\nu/\nu_0)^{-2.1}], \tag{6.1}$$

where τ is the optical depth, ν_0 is the reference frequency (for this project ν_0 = 15 GHz) and α is the intrinsic spectral index. Such a propagation effect has been seen previously in other gravitational lens systems, where one of the lensed images shows a different radio spectrum at lower observing frequencies (Mittal, Porcas, and Wucknitz, 2007; Winn, Rusin, and Kochanek, 2004). Similarly, the effects of synchrotron self-absorption, as seen in Figure 2.10, can also result in a similar down turn in the spectra of a radio source at lower frequencies, but as this should be intrinsic to the background radio source, we would expect to see this in the spectra of all of the lensed images. Also, both these absorption effects are prevalent in the low-frequency regime, and thus, our choice of observing the system in the high frequency range of 12 to 18 GHz was expected to avoid these affects. From the radio spectra presented in Figure 5.7, we see no evidence of a turnover for any of the lensed images. Also, from Figure 5.11, we see that the flux-ratios are flat with frequency, thus ruling out any differential free-free absorption.

Therefore, from our results, we are able to conclude that absorption affects do not play any role in the observed flux-ratio anomaly in CLASS B2045+265.

6.2 Variability of The Lensed Images

Another mechanism that could result in an anomalous flux-ratio measurement would be a single epoch observation coupled with some variability of one or all of the lensed images. Factors that may influence the flux-density measured over a period of time include the following.

- Internal variability, where the flux-density of the lensed AGN changes over time due to internal processes, coupled with the gravitational lensing time-delay. This should be predictive since the variation should be seen in all lensed images, after the time-delay has been corrected for (e.g. Biggs et al. 1999; Biggs 2023; Fassnacht et al. 2002).

- External variability (propagation), where the flux-density changes due to propagation effects as the light passes through a turbulent ionised medium. This will result in an un-correlated variability in one of more or the lensed images that occurs on different time scales (e.g. Koopmans et al. 2003; Biggs 2023).

- External variability (micro-lensing), where the flux-density changes due to the light interacting with low-mass objects moving across the path of the lensed image. This causes either a short or long time-scale change in the flux-density, which depends on whether the star is moving tangentially or radially with respect to the lensed image position (e.g. Koopmans and Bruyn 1999).

In this section, we investigate each of these possible scenarios.

6.2.1 Intrinsic Variability

Flares from AGN have been well studied. In the radio regime, these flares are believed to be due to adiabatic shocks within the AGN that induces synchrotron emission in phases (Marscher and Gear, 1985). These flares would not only affect the

TABLE 6.1: The percentage decrease in the flux-density of each component of CLASS B2045+265 at 15 GHz, from the VLA data collected in 1995 and 1996 (Fassnacht et al., 1999) and between 2022 March 15 and 2022 May 17, as part of this project.

Year	A	B	C	D	E
1995	$69.3 \pm 0.8\%$	73 ± 1 %	72 ± 1 %	54 ± 14 %	21 ± 11 %
1996	$55.5 \pm 0.9\%$	56 ± 2 %	53 ± 1 %	47 ± 10 %	3 ± 8 %

intrinsic flux density of the source, but may also have a direct influence on the flux ratios we observe. This is due to the time-delay between the light-paths of each lensed image and also by the different gravitational potential experienced by the different lensed images as they pass through the lens. When these flares occur, and if they have a time-scale less than that of the time delay, then each image will be showing the AGN at different phases of the flare. Therefore, we would observe differences in the measured flux density for each image, and thus, a difference in the flux ratios as a function of time.

Generally, AGN flares have typically a $\sim$ 2 year time-scale (Hovatta et al., 2008), whereas the time-delay of galaxy-scale lens systems are on day to month time-scales (Oguri, 2007). Thus, it is unlikely that intrinsic variability, coupled with a gravitational lensing time-delay are responsible for our observed flux ratio anomaly. A similar conclusion was drawn by Fassnacht et al. (1999) and Koopmans et al. (2003), who noted that the time-delays for CLASS B2045+265 could be a fraction of a day, for example, in the case of lensed images A and B. Furthermore, by comparing our results for the flux-ratios (see Table 5.6), to those of Koopmans et al. (2003), who found flux-ratios for B/A, C/A and D/A of 0.578 ± 0.059, 0.739 ± 0.073, 0.102 ± 0.025, respectively, at 5 GHz, we see that our results are completely consistent. The fact that these results are comparable over a 21 year period (and at two different frequencies) is also evidence that short time-scale intrinsic variability does not play a substantial role in the flux-ratio anomaly of CLASS B2056+265.

Interestingly, we have found from comparing our data with those of Fassnacht et al. (1999) that CLASS B2045+265 is variable over a long time-scale. As shown in Figure 6.1 and Table 6.1, we see that there is a significant decrease in the flux-density of the system between 1995 and 2022 (at 15 GHz). For lensed images A, B, C and D, the drop in flux-density is about 71% since 1995 and about 55% since 1996, whereas the emission from the lensing galaxy is basically consistent with no variability (thus ruling out a calibration error). From this, we can conclude that there is intrinsic variability present in CLASS B2045+265, however, as discussed above, this variability does not provide a significant contribution to the flux-ratio anomaly given that the time-scale is much larger than the gravitational lensing time-delay.

6.2.2 Extrinsic Variability

An alternative cause of variability in the flux ratios of CLASS B2045+265 could be external factors, such as interstellar scintillation or micro-lensing. These mechanisms are discussed by Koopmans et al. (2003), who found that the flux ratios of CLASS B2045+265 varied by up to 40% at 5 GHz on time-scales of several months. Also, Koopmans and Bruyn (1999) found evidence of extrinsic variability in the gravitational lens system CLASS B1600+434 with the VLA at 8.5 GHz. Those authors discussed whether scintillation from an ionized ISM or micro-lensing by stars could be the cause. Therein, it was concluded that scintillation from scattering effects due to

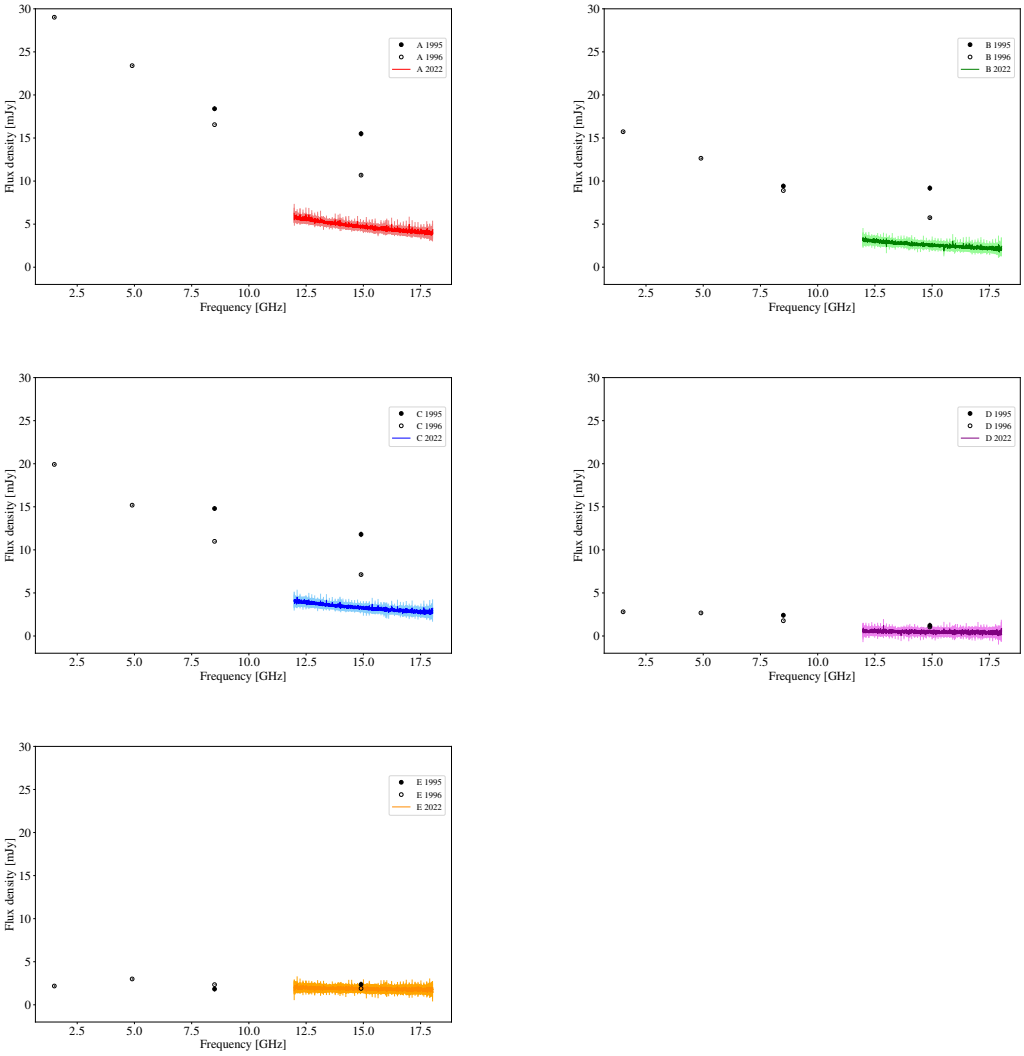

FIGURE 6.1: A comparison of the flux-densities and broad band radio spectra of CLASS B2045+265 between 1995 and 1996 (Fassnacht et al., 1999), and 2022 (this thesis). We see a clear decrease in the flux-density of the lensed images A, B, C and D, whereas the emission from the lensing galaxy E remains fairly constant. This is direct evidence for a long-term variability of the lensed radio source CLASS B2045+265.

a turbulent ISM could cause a large variability in the emission from compact radio sources, in what is described as a "flickering" low amplitude variation of more extended sources (Rickett, 1990). However, such a variability would be due to rapid variations in the ISM, and thus, would coincide with variability on time-scales less than a day. As well as short time-scale variability, there has also been evidence of scattering through high angular resolution observations of lensed images. For example, the gravitational lens systems JVAS B0218+357 (Biggs et al., 2003; Mittal, Porcas, and Wucknitz, 2007) and CLASS B0128+437 (Biggs et al., 2004) are known to be scatter-broadened. We note that the latter system is also part of the LoFT project and shows evidence of scattering even at 15 GHz in HSA imaging (Peters et al., in preparation). As seen from Figure 5.10, we observe low-level fluctuations (a few per cent) in the flux-ratios on time scales of weeks. Although these variations do not produce the required change in the flux-ratios to explain the anomalies, they could point towards evidence of scattering in the ISM of the lensing galaxy. Our VLA monitoring data are not sufficient to determine if this is the case or not, but the future analysis of the HSA imaging at 15 GHz of CLASS B2045+265 should allow this to be investigated further. However, we do note that the VLBA imaging of the system at 5 GHz by McKean et al. (2007) did not find any evidence of scattering in the lensed images of CLASS B2045+265.

In the case of micro-lensing, Koopmans and Bruyn (1999) show that for compact radio sources with steep-spectra at high frequencies (such as in the case of CLASS B2045+265), this mechanism can play a significant role in producing variability on week to month time-scales. The causes of these micro-lensing events are compact mass concentrations, such as stars, planets, black holes, molecular clouds etc. This effect is described in detail for micro-lensing of strongly lensed quasars by Vernardos et al. (2023), which is typically seen at ultra-violet to near-infrared wavelengths due to the small size of quasar accretion disks relative to the Einstein radius of the micro-lensing stars. As these compact objects move across the line-of-sight to our lensed images, they will cause changes to the image magnifications that are independent of each other. These changes may account for the variability seen in our flux ratios as well as account for the different level of variability seen between our observations and those of Koopmans et al. (2003). This is because the intrinsic source is likely larger at lower frequencies, and smaller source sizes will have a larger impact on the resulting image magnifications from micro-lensing. Although CLASS B2045+265 seems to be a good candidate for micro-lensing, which would account for the variability seen in both this project as well as by Koopmans et al. (2003), this again would fail to explain our flux-ratio anomaly. As seen in Figure 5.9, the low-level variations, seen at two different frequencies and separated by over two decades, are not large enough to globally change the relative flux ratios.

Thus, we conclude that our observed flux ratios can not be explained by scattering nor micro-lensing of one or more of the lensed images.

6.3 The Gravitational Lens Mass Model

A flux-ratio anomaly exists when the observed flux-ratios significantly differ from what is predicted from the gravitational lens mass model. Given that we see no evidence that some absorption effect (propagation) or either extrinsic and/or intrinsic variability (micro-lensing / scattering) are the cause, we now investigate whether this can be an issue with the gravitational lensing mass model.

If we recall, in Chapter 3 we introduced the idea of magnification effects from cold dark matter (CDM) sub-haloes, given the case-study of JVAS B1422+231. We visually showed what a possible CDM model may look like in Figure 3.3; there, we noted that the distribution of these CDM sub-haloes may be able to influence our flux ratios by having magnification effects that affect each image of the lensed source in a different way. By having these sub-haloes within the lens galaxy or along the line-of-sight, an observable imprint may be left on the gravitational lensing signal of these images (Vegetti et al., 2023). These imprints can be seen in the relative image magnifications, a change in the image positions, or as an additional gravitational time delay. In particular, these CDM sub-haloes within the lensing galaxy halo or along the line of sight will induce a magnification of the images similar to that of micro-lensing (this is referred to as milli-lensing). However, these changes in the magnification will not be time dependent (due to the rotational velocity of the halo and the sub-halo being relatively slow) and may account for the consistency in the flux-ratio anomaly observed by Koopmans et al. (2003) and the results presented in this thesis. Here, we have focused on the effects on the image magnifications by measuring the flux ratios, as well as using the R_{cusp} parameter for CLASS B2045+265; in doing so, we have shown that the nature of the flux ratio anomaly is indeed quite extreme. We have also shown that complex mass models (elliptical power-law with and without multipoles) are unable to reproduce the observed flux ratios. It is seen that multipole mass distributions have a larger uncertainty than that of an elliptical power-law, and thus, are closer to our observed results (see Figures 5.13 and 5.14). However, these results also require a mass fraction in CDM sub-haloes within the lensing galaxy (see Figures 5.15 and 5.16) that is much larger than is expected for CDM models. This implies that the CDM model is inconsistent with our data. It is also important to note that there seems to be little to no change in these expectations from visit to visit; this is likely due to the predicted flux ratios from the simulations not being within a reasonable range to those of our observed values, which have only (at most) at few per cent scatter.

Before concluding that our results rule out the CDM model (note that such a high mass fraction in sub-haloes would be even more problematic for WDM models), we need to look at other potential reasons for there being such a large inferred mass fraction in sub-haloes from our analysis. The discrepancy between the simulated flux-ratios and the observed values may indicate that a power law model, as presented in Figure 5.13, along with sub-haloes in the lens is not the correct model. For example, it may be that the system is dominated by line-of-sight low mass haloes. Unfortunately, we did not have the time to test this here, since such a calculation is computationally much more expensive. However, from our results, we suspect that this would also be insufficient to explain the discrepancy since this effect is expected to make up around 70% of the sub-halo signal (Despali et al., 2018). Although significant, this would not be enough to pull our constraints down to the expectations for CDM. Thus, this leads us to believe that a mix of an additional, and thus far, unaccounted for component of the complex mass distribution, along with CDM sub-haloes within the lensing halo as well as outside its bounds, may be able to account for the observed flux ratio anomaly present in CLASS B2045+265. Searching for this additional mass structure should be a goal of future research.

Chapter 7

Conclusions

We now conclude this thesis with a brief look back at our aims and goals, as outlined in the early chapters. We also review our results and discuss how they impact our understanding of dark matter, and in particular, the flux-ratio anomaly of CLASS B2045+265. We also discuss what future research should be done in this field.

7.1 Summary and Future Work

To summarize, we have investigated the quadruple imaged gravitationally lensed radio source CLASS B2045+265, for which simple mass models are unable to correctly predict the observed flux ratios. This is an example of a so called flux ratio anomaly system, which have been instrumental for our understanding of one of the biggest mysteries in astronomy, that is, the existence and nature of dark matter. CLASS B2045+265 is an extreme example of a flux-ratio anomaly system where there is a significant discrepancy between the predicted and observed flux-ratios; this has been shown most evidently by the calculated $R_{cusp} = 0.5137 \pm 0.0003$ (where the predicted value of R_{cusp} should tend to 0 for a cusp lens system). This led to CLASS B2045+265 being investigated via broadband VLA observations between 12 and 18 GHz, for 20 visits over a 63 day period, as part of the Lensing over Frequency and Time (LoFT) project. The goal of these observations was to investigate the robustness of the flux-ratio anomaly of the system, while showcasing an example of what broadband observations of gravitational lensing with the SKA and ngVLA can achieve.

In this thesis, we have developed a data reduction, imaging and data extraction pipeline for analysing such data. This pipeline is being applied by other members of the LoFT team to the other targets of that project. Our choice of observing in the high-frequency bands was chosen in order to avoid possible absorption and scattering affects in the spectra. From these broadband observations, we were able to rule-out these propagation effects by examining the spectra for discrete and continuous absorption and scattering effects. Furthermore, as CLASS B2045+265 was observed for 20 epochs over a period of 3 months (63 days), this allowed us to further investigate whether there was any variability of the flux ratios. From this analysis we found that the flux-ratios of CLASS B2045+265 varied by 1.6% to 3.7%, which although statistically significant had no consequential effects on the observed flux-ratio anomaly. With these results we have been able to rule out variability as a possible explanation for the observed anomaly. This led us to investigate complex mass models (in collaboration with Dr. Jacob Cohen and Dr. Simona Vegetti) for CLASS B2045+265 in order to reproduce the results of our observed flux ratios. However, we were again unsuccessful. Our results led us to test whether the cause of our anomaly could be due to a population of dark matter sub-haloes in the foreground lensing galaxy, as predicted by CDM mass models. These dark matter sub-haloes are able to change the fluxes of each image of our system independently (in the form of milli-lensing).

Using our observed flux ratios and image positions for each epoch, we produced a probability density function of the mass-fraction in sub-haloes (f_{sub}). These results were inconclusive as the value of f_{sub} was poorly constrained by our data, that is, the mass fraction required to satisfy the flux-ratios was too high, but at these high levels, the image positions could no longer be well fit. This led us to believe that combinations of a complex mass model and CDM sub-haloes, both within the lens and along the line of sight, may be able to account for the extreme flux-ratio anomaly that we have observed for CLASS B2045+265.

Although our results indicate the presence of an unrealistically high abundance of CDM sub-haloes within the foreground lensing galaxy halo, further research is needed to confirm this conclusion. As part of LoFT, Very Long Baseline Interferometry (VLBI) data at 15 GHz is also available for CLASS B2045+265. The analysis of these data is the natural next step into our investigation of this object. Given the high resolution of the VLBI data, perturbations of the image surface brightness distributions may be directly observed, which would further support the requirement of CDM sub-haloes being present in the foreground lensing galaxy. Also, these data would further rule out any scattering of the lensed images. ngVLA and SKA-MID observations would be able to conduct similar wide-band analyses in the future to rule out time and frequency variability aspects of flux-ratio anomalous systems with higher sensitivity, faster processing and improved RFI mitigation.

Thus, from the research conducted through this MSc project, we have been able to rule out many possible effects that could play a role in the anomaly seen in CLASS B2045+265. However, we were unable to rule-out whether complex mass models or luminous/dark sub-haloes are the definitive cause. Such sub-haloes are consistent with those predicted to exist in a CDM Universe. Thus, it is our belief that further investigation into anomalous lens systems may hold vital information into the nature of dark matter in our Universe, which has been perplexing astronomers for years.

Bibliography

Bartelmann, Matthias and Peter Schneider (Jan. 2001). "Weak gravitational lensing". In: *Physics Reports* 340.4–5, 291–472. ISSN: 0370-1573. DOI: 10.1016/s0370-1573(00)00082-x. URL: http://dx.doi.org/10.1016/S0370-1573(00)00082-X.

Biggs, A. D. (June 2023). "A VLA monitoring study of JVAS B1422+231: investigation of time delays and detection of extrinsic variability". In: 522.1, pp. 426–437. DOI: 10.1093/mnras/stad870. arXiv: 2303.11987 [astro-ph.GA].

Biggs, A. D. et al. (Apr. 1999). "Time delay for the gravitational lens system B0218+357". In: 304.2, pp. 349–358. DOI: 10.1046/j.1365-8711.1999.02309.x. arXiv: astro-ph/9811282 [astro-ph].

Biggs, A. D. et al. (Jan. 2003). "Global 8.4-GHz VLBI observations of JVAS B0218+357". In: 338.3, pp. 599–608. DOI: 10.1046/j.1365-8711.2003.06050.x. arXiv: astro-ph/0209182 [astro-ph].

Biggs, A. D. et al. (May 2004). "Radio, optical and infrared observations of CLASS B0128+437". In: 350.3, pp. 949–961. DOI: 10.1111/j.1365-2966.2004.07701.x. arXiv: astro-ph/0402128 [astro-ph].

Blandford, Roger D. and Christopher S. Kochanek (Oct. 1987). "Gravitational Imaging by Isolated Elliptical Potential Wells. I. Cross Sections". In: 321, p. 658. DOI: 10.1086/165660.

Bovy, Jo (in preparation). "Dynamics and Astrophysics of Galaxies". In: Princeton University Press. Chap. 16.

Bradac, M. et al. (2002). "B1422+231: The influence of mass substructure on strong lensing". In: *A&A* 388.2, pp. 373–382. DOI: 10.1051/0004-6361:20020559. URL: https://doi.org/10.1051/0004-6361:20020559.

Browne, I. W. A. et al. (May 2003). "The Cosmic Lens All-Sky Survey - II. Gravitational lens candidate selection and follow-up". In: 341.1, pp. 13–32. DOI: 10.1046/j.1365-8711.2003.06257.x. arXiv: astro-ph/0211069 [astro-ph].

CASA Team et al. (Nov. 2022). "CASA, the Common Astronomy Software Applications for Radio Astronomy". In: 134.1041, 114501, p. 114501. DOI: 10.1088/1538-3873/ac9642. arXiv: 2210.02276 [astro-ph.IM].

Christian, Carol and Jean-René Roy (2017). "Telescopes". In: *A Question and Answer Guide to Astronomy*. Cambridge University Press, 253–272.

Cohen, Jacob S. et al. (2024). *General Multipoles and Their Implications for Dark Matter Inference*. arXiv: 2403.08895 [astro-ph.CO].

Condon, James J. and Scott M. Ransom (2016). *Essential Radio Astronomy*.

Congdon, Arthur B. and Charles R. Keeton (Dec. 2005). "Multipole models of four-image gravitational lenses with anomalous flux ratios". In: *Monthly Notices of the Royal Astronomical Society* 364.4, 1459–1466. ISSN: 1365-2966. DOI: 10.1111/j.1365-2966.2005.09699.x. URL: http://dx.doi.org/10.1111/j.1365-2966.2005.09699.x.

Despali, Giulia et al. (Apr. 2018). "Modelling the line-of-sight contribution in substructure lensing". In: 475.4, pp. 5424–5442. DOI: 10.1093/mnras/sty159. arXiv: 1710.05029 [astro-ph.CO].

Fassnacht, C. D. et al. (1999). "B2045265: A New Four-Image Gravitational Lens from CLASS". In: *The Astronomical Journal* 117.2, pp. 658–670. DOI: 10.1086/300724. URL: https://doi.org/10.1086%2F300724.

Fassnacht, C. D. et al. (Dec. 2002). "A Determination of H_0 with the CLASS Gravitational Lens B1608+656. III. A Significant Improvement in the Precision of the Time Delay Measurements". In: 581.2, pp. 823–835. DOI: 10.1086/344368. arXiv: astro-ph/0208420 [astro-ph].

Gunn, J. E. (Dec. 1977). "Massive galactic halos. I. Formation and evolution." In: 218, pp. 592–598. DOI: 10.1086/155715.

Hogg, D. W. and R. D. Blandford (June 1994). "The gravitational lens system B 1422+231 : dark matter, superluminal expansion and the Hubble constant." In: 268, pp. 889–893. DOI: 10.1093/mnras/268.4.889. arXiv: astro-ph/9311077 [astro-ph].

Hovatta, T. et al. (May 2008). "Long-term radio variability of AGN: flare characteristics". In: *Astronomy amp; Astrophysics* 485.1, 51–61. ISSN: 1432-0746. DOI: 10.1051/0004-6361:200809806. URL: http://dx.doi.org/10.1051/0004-6361:200809806.

Hsueh, J-W et al. (2019). "SHARP – VII. New constraints on the dark matter free-streaming properties and substructure abundance from gravitationally lensed quasars". In: *Monthly Notices of the Royal Astronomical Society* 492.2, pp. 3047–3059. DOI: 10.1093/mnras/stz3177. URL: https://doi.org/10.1093%2Fmnras%2Fstz3177.

Keeton, C. R., C. S. Kochanek, and U. Seljak (1997). "Shear and Ellipticity in Gravitational Lenses". In: *The Astrophysical Journal* 482.2, p. 604. DOI: 10.1086/304172. URL: https://dx.doi.org/10.1086/304172.

Keeton, Charles R., B. Scott Gaudi, and A. O. Petters (2003). "Identifying Lenses with Small-Scale Structure. I. Cusp Lenses". In: *The Astrophysical Journal* 598.1, p. 138. DOI: 10.1086/378934. URL: https://dx.doi.org/10.1086/378934.

Keeton, Charles R., B. Scott Gaudi, and Arlie O. Petters (2002). "Identifying Lensing by Substructure. I. Cusp Lenses". In: URL: https://api.semanticscholar.org/CorpusID:262514937.

Koopmans, L. V. E. and A. G. de Bruyn (1999). *Microlensing Scintillation of Gravitationally Lensed Compact Radio Sources: Evidence for MACHOs?* arXiv: astro-ph/9910189 [astro-ph].

Koopmans, L. V. E. et al. (2003). "Extrinsic Radio Variability of JVAS/CLASS Gravitational Lenses". In: *The Astrophysical Journal* 595.2, p. 712. DOI: 10.1086/377434. URL: https://dx.doi.org/10.1086/377434.

Kormann, R., P. Schneider, and M. Bartelmann (June 1994). "A gravitational lens model for B1422+231." In: 286, pp. 357–364. DOI: 10.48550/arXiv.astro-ph/9311011. arXiv: astro-ph/9311011 [astro-ph].

Mao, Shude and Peter Schneider (Apr. 1998). "Evidence for substructure in lens galaxies?" In: *Monthly Notices of the Royal Astronomical Society* 295.3, 587–594. ISSN: 1365-2966. DOI: 10.1046/j.1365-8711.1998.01319.x. URL: http://dx.doi.org/10.1046/j.1365-8711.1998.01319.x.

Marscher, A. P. and W. K. Gear (Nov. 1985). "Models for high-frequency radio outbursts in extragalactic sources, with application to the early 1983 millimeter-to-infrared flare of 3C 273." In: 298, pp. 114–127. DOI: 10.1086/163592.

McCracken, Garry and Peter Stott (2013). "Chapter 5 - Magnetic Confinement". In: *Fusion (Second Edition)*. Ed. by Garry McCracken and Peter Stott. Second Edition. Boston: Academic Press, pp. 45–58. ISBN: 978-0-12-384656-3. DOI: https:

//doi.org/10.1016/B978-0-12-384656-3.00005-2. URL: https://www.sciencedirect.com/science/article/pii/B9780123846563000052.

McKean, J. P. et al. (May 2007). "High-resolution imaging of the anomalous flux ratio gravitational lens system CLASS B2045+265: dark or luminous satellites?" In: *Monthly Notices of the Royal Astronomical Society* 378.1, pp. 109–118. ISSN: 0035-8711. DOI: 10.1111/j.1365-2966.2007.11744.x. eprint: https://academic.oup.com/mnras/article-pdf/378/1/109/3962377/mnras0378-0109.pdf. URL: https://doi.org/10.1111/j.1365-2966.2007.11744.x.

Meneghetti, Massimo (2017). *Introduction to Gravitational Lensing*.

Mittal, R., R. Porcas, and O. Wucknitz (Apr. 2007). "Free-free absorption in the gravitational lens JVAS B0218+357". In: 465.2, pp. 405–415. DOI: 10.1051/0004-6361:20066127. arXiv: astro-ph/0607623 [astro-ph].

Myers, S. T. et al. (May 2003). "The Cosmic Lens All-Sky Survey - I. Source selection and observations". In: 341.1, pp. 1–12. DOI: 10.1046/j.1365-8711.2003.06256.x. arXiv: astro-ph/0211073 [astro-ph].

Narayan, Ramesh and Sylvanie Wallington (1992). "Introduction to basic concepts of gravitational lensing". In: *Gravitational Lenses*. Ed. by Rainer Kayser, Thomas Schramm, and Lars Nieser. Berlin, Heidelberg: Springer Berlin Heidelberg, pp. 12–26. ISBN: 978-3-540-47286-5.

Navarro, Julio F., Carlos S. Frenk, and Simon D. M. White (May 1996). "The Structure of Cold Dark Matter Halos". In: 462, p. 563. DOI: 10.1086/177173. arXiv: astro-ph/9508025 [astro-ph].

Nierenberg, A. M. et al. (Aug. 2014). "Detection of substructure with adaptive optics integral field spectroscopy of the gravitational lens B1422+231". In: 442.3, pp. 2434–2445. DOI: 10.1093/mnras/stu862. arXiv: 1402.1496 [astro-ph.GA].

Oguri, Masamune (May 2007). "Gravitational Lens Time Delays: A Statistical Assessment of Lens Model Dependences and Implications for the Global Hubble Constant". In: *The Astrophysical Journal* 660.1, 1–15. ISSN: 1538-4357. DOI: 10.1086/513093. URL: http://dx.doi.org/10.1086/513093.

Patnaik, A. R. and D. Narasimha (Oct. 2001). "Determination of time delay from the gravitational lens B1422+231". In: 326.4, pp. 1403–1411. DOI: 10.1111/j.1365-2966.2001.04711.x. arXiv: astro-ph/0106104 [astro-ph].

Patnaik, A. R. et al. (Nov. 1992). "B 1422+231 : a new gravitationally lensed system at Z = 3.62." In: 259, 1P–4. DOI: 10.1093/mnras/259.1.1P.

Perley, R. A. and B. J. Butler (May 2017). "An Accurate Flux Density Scale from 50 MHz to 50 GHz". In: 230.1, 7, p. 7. DOI: 10.3847/1538-4365/aa6df9. arXiv: 1609.05940 [astro-ph.IM].

Rickett, B. J. (Jan. 1990). "Radio propagation through the turbulent interstellar plasma." In: 28, pp. 561–605. DOI: 10.1146/annurev.aa.28.090190.003021.

Rybicki, G. B. and A. P. Lightman (1985). *Radiative processes in astrophysics.*

Shepherd, M. C. (Jan. 1997). "Difmap: an Interactive Program for Synthesis Imaging". In: *Astronomical Data Analysis Software and Systems VI*. Ed. by Gareth Hunt and Harry Payne. Vol. 125. Astronomical Society of the Pacific Conference Series, p. 77.

Vegetti, S. et al. (2023). *Strong gravitational lensing as a probe of dark matter*. arXiv: 2306.11781 [astro-ph.CO].

Vernardos, G. et al. (2023). *Microlensing of strongly lensed quasars*. arXiv: 2312.00931 [astro-ph.GA].

Winn, Joshua N., David Rusin, and Christopher S. Kochanek (Feb. 2004). "The central image of a gravitationally lensed quasar". In: 427.6975, pp. 613–615. DOI: 10.1038/nature02279. arXiv: astro-ph/0312136 [astro-ph].

Xu, Dandan et al. (Jan. 2015). "How well can cold dark matter substructures account for the observed radio flux-ratio anomalies". In: *Monthly Notices of the Royal Astronomical Society* 447.4, pp. 3189–3206. ISSN: 0035-8711. DOI: 10.1093/mnras/stu2673. eprint: https://academic.oup.com/mnras/article-pdf/447/4/3189/5702368/stu2673.pdf. URL: https://doi.org/10.1093/mnras/stu2673.